

2

RL-TR-91-57, Vol I (of two)
Final Technical Report
April 1991

DTIC
87-00000



AD-A236 648



ADAPTIVE BEAMFORMING ALGORITHMS FOR HIGH RESOLUTION MICROWAVE IMAGING

University of Pennsylvania

Bernard D. Steinberg and Boogsoon Kang



Accession For	
DTIC Special	<input checked="" type="checkbox"/>
DTIC CAS	<input type="checkbox"/>
Unannounced	<input type="checkbox"/>
Justification	
By	
Distribution	
Availability Codes	
Avail and/or	
Dist	Special
A-1	

APPROVED FOR PUBLIC RELEASE; DISTRIBUTION UNLIMITED.

This effort was funded totally by the Laboratory Director's fund.

91-01818



Rome Laboratory
Air Force Systems Command
Griffiss Air Force Base, NY 13441-5700

91 6 11 097

This report has been reviewed by the Rome Laboratory Public Affairs Office (PA) and is releasable to the National Technical Information Service (NTIS). At NTIS it will be releasable to the general public, including foreign nations.

RL-TR-91-57, Vol I (of two) has been reviewed and is approved for publication.

APPROVED: 

ROBERT A. SHORE
Project Engineer

APPROVED: 

JOHN K. SCHINDLER
Director of Electromagnetics

FOR THE COMMANDER:



BILLY G. OAKS
Directorate of Plans & Programs

If your address has changed or if you wish to be removed from the Rome Laboratory mailing list, or if the addressee is no longer employed by your organization, please notify RL(EAAC) Hanscom AFB MA 01731-5000. This will assist us in maintaining a current mailing list.

Do not return copies of this report unless contractual obligations or notices on a specific document require that it be returned.

REPORT DOCUMENTATION PAGE

Form Approved
OMB No. 0704-0188

Public reporting burden for this collection of information is estimated to average 1 hour per response, including the time for reviewing instructions, searching existing data sources, gathering and maintaining the data needed, and completing and reviewing the collection of information. Send comments regarding this burden estimate or any other aspect of this collection of information, including suggestions for reducing this burden, to Washington Headquarters Services, Directorate for Information Operations and Reports, 1215 Jefferson Davis Highway, Suite 1204, Arlington, VA 22202-4302, and to the Office of Management and Budget, Paperwork Reduction Project (0704-0188), Washington, DC 20503.

1. AGENCY USE ONLY (Leave Blank)		2. REPORT DATE April 1991		3. REPORT TYPE AND DATES COVERED Final Sep 87 - Feb 90	
4. TITLE AND SUBTITLE ADAPTIVE BEAMFORMING ALGORITHMS FOR HIGH RESOLUTION MICROWAVE IMAGING				5. FUNDING NUMBERS C - F30602-88-D-0025 Task: E-8-7066 PE - 61102F PR - LDFF TA - 08 WU - P8	
6. AUTHOR(S) Bernard D. Steinberg, Boogsoon Kang					
7. PERFORMING ORGANIZATION NAME(S) AND ADDRESS(ES) University of Pennsylvania The Moore School of Electrical Engineering Valley Forge Research Center Philadelphia PA 19104				8. PERFORMING ORGANIZATION REPORT NUMBER	
9. SPONSORING/MONITORING AGENCY NAME(S) AND ADDRESS(ES) Rome Laboratory (EEAS) Hanscom AFB MA 01731-5000				10. SPONSORING/MONITORING AGENCY REPORT NUMBER RL-TR-91-57, Vol I (of two)	
11. SUPPLEMENTARY NOTES Rome Laboratory Project Engineer: Robert A. Shore/EEAS/(617)377-2058 This effort was funded totally by the Laboratory Director's fund.					
12a. DISTRIBUTION/AVAILABILITY STATEMENT Approved for public release; distribution unlimited.				12b. DISTRIBUTION CODE	
13. ABSTRACT (Maximum 200 words) Two types of algorithms for self-calibrating distorted antenna arrays are presented and evaluated. Both successfully convert badly distorted phased arrays into diffraction-limited systems. One group is called the dominant scatterer class; each of the several algorithms in this class develops a correction weight vector from the radar echoes of one or more scatterers having large radar cross section. The second is the spatial correlation class. This group of algorithms determines the weight vector from the spatial correlation function of the measured radiation field from targets and clutter. Tests are conducted with simulation and with high resolution radar data of airborne and ground-based targets. The spatial correlation algorithms are less sensitive to the source distribution (targets and clutter locations) and therefore are preferred for a general radar environment. These algorithms require more computation than those based upon dominant scatterers. Relative computation times are measured and presented.					
14. SUBJECT TERMS Radar, Self-Cohering, Phased Arrays, Adaptive Beamforming				15. NUMBER OF PAGES 154	
				16. PRICE CODE	
17. SECURITY CLASSIFICATION OF REPORT UNCLASSIFIED	18. SECURITY CLASSIFICATION OF THIS PAGE UNCLASSIFIED	19. SECURITY CLASSIFICATION OF ABSTRACT UNCLASSIFIED	20. LIMITATION OF ABSTRACT U/L		

TABLE OF CONTENTS

0.INTRODUCTION.....	1
1.THE RADIO CAMERA.....	4
2.ADAPTIVE BEAMFORMING.(ABF).....	17
3.DOMINANT SCATTERER ALGORITHMS (DSA)....	25
4.SPATIAL CORRELATION ALGORITHMS (SCA)...	96
5.RELATIVE COMPUTATION TIMES.....	142
6.SUMMARY.....	143
REFERENCES.....	144

ADAPTIVE BEAMFORMING ALGORITHMS FOR
HIGH RESOLUTION MICROWAVE IMAGING

Bernard D. Steinberg
Bongsoon Kang

0. INTRODUCTION

This report is an algorithmic study of adaptive beamforming, which is a means for self-calibrating a radio camera. A radio camera is a bistatic microwave radar with a huge antenna array, the array being sufficiently large to enable the system to achieve the fine angular or cross-range resolution that hitherto had been available only with optical or near-optical instruments.

The bulk of the work performed to date falls into two categories. In the first body of work the self-calibrating portion of the phased array system is driven by the reradiation from a prominent reflector having large radar cross section and small physical size. The conditions under which such a phase-synchronizing source operates satisfactorily are given in [8], [4]. Algorithms of the second class are designed to operate upon the backscatter from statistically homogeneous targets and terrain [18],[17]. Examples of such backscattering sources are sea clutter, crowns of trees in a forest and large expanses of sand.

Because of the lessened dependence upon specificity of source distribution the algorithms in the second body of work are generally referred to as scene-free algorithms. The RADC support for the reported work focused upon the scene-free ABF procedures.

For completeness, however, both classes of algorithms are described. Section 1 is introductory, describing uses of the radio camera. Section 2 gives a brief, partial history of self-calibration, discusses certain interesting properties of ABF algorithms and indicates desirable properties of such algorithms. The two classes of algorithms are described in Sections 3 and 4¹. These sections also show experimental results of the application of these algorithms to high resolution X-band (3 cm wavelength) radar data obtained from VFRC radio cameras. Section 5 compares the relative computation times required by algorithms from both classes. Section 6 is the Summary. The Appendix, authored by Ph.D. candidate Bongsoon Kang, presents additional experiments, analytical details and further comparisons between algorithms.

It is found experimentally that highly distorted phased arrays can be self-calibrated under a very wide range of conditions. The dominant scatterer algorithm (DSA), which is the basic procedure in the first class, almost always can be made to self-calibrate on man-made structures. A modifica-

¹These sections form the bases for two chapters in a forthcoming book to be published by John Wiley: B. D. Steinberg and H. Subbaram, Microwave Imaging Techniques.

tion, the multiple scatterer algorithm (MSA), extends its usefulness under conditions of poor target to clutter ratio. The scene-free ABF algorithms are superior when the source distribution is statistically homogeneous, e.g., sea clutter. Although the scene-free techniques were designed primarily for statistically homogeneous backscattering, the experimental evidence indicates that they perform exceedingly well under those conditions in which the dominant scatterer algorithms also work. Thus the scene-free algorithms have been found to be more generally applicable than the dominant scatterer algorithms, they do, however, require greater computational strength. However, because of the continuing improvement over the years in speed, capacity and cost of realtime signal processing devices, it is concluded that the design of future radar systems requiring very large antennas should be based upon the scene-free algorithms.

The authors are grateful to Dr. Robert Shore of RADC, Hanscom AFB, Bedford MA for his careful editing of the draft of this report.

1. THE RADIO CAMERA

The diffraction-limited resolution of an aperture (lens, telescope mirror, microwave dish, phased array, ultrasonic transducer) is, in radians, approximately the reciprocal of the size of the aperture in units of wavelength. When the aperture is too large to maintain the rigidity necessary for diffraction-limited performance (approximately one-tenth of a wavelength) it is necessary to introduce a low-order intelligence into the antenna system so as to dynamically self-calibrate it as it undergoes distortion.

Such an aperture, i.e., one too large to maintain its shape, is called a large aperture. Large apertures include distributed antennas, that is, antennas the parts of which are located on separate and independent platforms. Examples of such apertures and their potential applications are shown in Figures 1.1 to 1.4.

Figure 1.1 depicts either an air traffic control (ATC) environment or an aircraft landing problem. An airport is shown with an ATC radar illuminating a target with a microwave pulse and receiving an echo. The echo is displayed as a blip on the monitor scope in range-angle coordinates. The presence of the blip constitutes detection and the coordinates indicate the distance to the target and its bearing. No shape information is obtained because the width of the beam is very large compared to the size of the airplane, as is easy to see from the following calculation. Diffraction theory teaches that the angular width of the beam, in radians, is approximately the ratio of the wavelength of the radi-

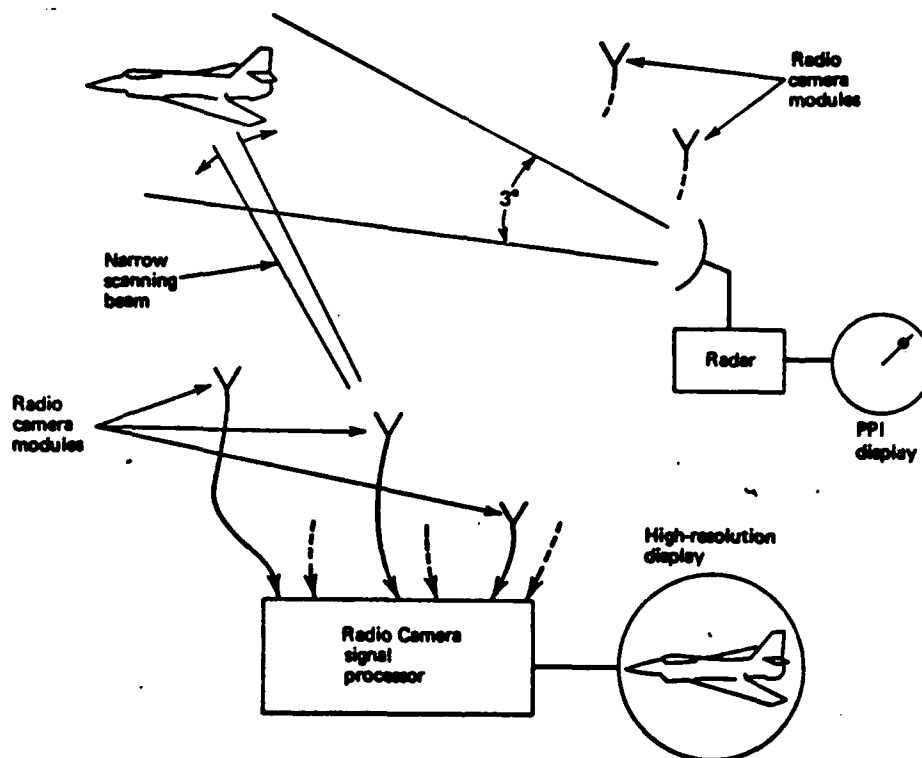


FIGURE 1.1. AIRPORT APPLICATION OF THE RADIO CAMERA. A CONVENTIONAL RADAR TRANSMITTER ILLUMINATES THE AIRPLANE WITH A PULSE. ECHOES ARE RECEIVED BY THE RADIO CAMERA MODULES, EACH OF WHICH CONSISTS OF AN ANTENNA AND A COHERENT MICROWAVE RECEIVER. THE MODULES ARE DISTRIBUTED ACROSS THE AIRPORT WHEREVER THERE IS EMPTY SPACE. THE ECHOES ARE TRANSMITTED TO THE RADIO CAMERA SIGNAL PROCESSOR WHICH CREATES A HIGH RESOLUTION IMAGE OF THE TARGET. THE BEAM-WIDTH OF THE RADIO CAMERA IS $10\mu\text{rad}$ WHEN THE WAVELENGTH IS 5cm AND THE AIRPORT IS 5km . (FROM [4].)

ation to the size of the antenna. A typical value of this ratio is $1/30$. The beam cross-section at a target distance of, say, 30 km is one km whereas the size of a large airplane is only 40 to 50 m. Because the target is so much smaller than the beam cross-section it reflects as a single point and appears as such in the radar display.

The airport, on the other hand, is several km in size. Imagine that an imaging system consisting of hundreds of small antennas and receivers, plus the proper central signal processor, is spread out over the airport in the manner shown in Figure 1.1. Assuming that the signal processor could appropriately process the echoes, the width of the beam that would be formed would be determined by the size of the airport rather than the size of each individual antenna. For example, let the airport be 5 km and the wavelength 5 cm. The beamwidth of the system would be $1/100,000$ rad and the beam cross-section at the target would be 30 cm. This 30 cm-cross-section beam could then be scanned across the target to provide an image with more than 100 resolution cells in the cross-range or azimuth direction. Experience with very high resolution imaging radar at the Valley Forge Research Center (VFRC) of the University of Pennsylvania shows that at most 30 to 50 resolution cells on a target are adequate to define the target. Hence in this ATC example the radar controller would be provided with adequate resolution in the cross-range direction to differentiate between types of aircraft.

Of course high resolution in the range direction is also necessary for it provides the second dimension needed for two-dimen-

sional imaging. High resolution in range is obtained through the use of a wide bandwidth transmitted signal. In the VFRC experiments shown later in this report a 7 ns pulse having 150 MHz bandwidth is employed. With such a waveform a range resolution of 1 m is achieved.

An imaging instrument of this kind is called a radio camera [1]. It is basically a bistatic imaging device operating at microwave wavelengths. Like a conventional optical camera it operates upon the reflections from an illuminator that does not have to be colocated with the receiving aperture. There the similarity stops, however. Not only must the receiving aperture be large enough to provide the desired resolution, but because the wavelength of the radiation is three to six orders of magnitude larger than optical radiation, there are several fundamental, inherent design differences.

These differences fall into three categories. The **first** is aperture design. The **second** category is the scattering properties of targets vs. wavelength. The **third** is propagation and weather effects.

The first category is the most critical. Because of the huge aperture size required at microwaves to achieve the modest angular resolution of common optical instruments the radio camera aperture must be assumed by the designer to be intrinsically distorted. That is, the designer is forced to assume that, no matter how carefully s/he specified the antenna element locations and their complex weights, the actual antenna will differ sufficiently so as to destroy the desired radiation pattern.

Consider the illustration above. The 5 km radio camera operating at 5 cm wavelength is as large in units of wavelength as a 50 mm optical telescope. While the latter can be constructed from a small lens purchased from a scientific supply shop, the former cannot be designed from standard antenna design practice alone. **First**, it cannot be assumed that the required positional tolerance of less than $1/10$ wavelength can be achieved when the antenna elements are deployed over 100,000 wavelengths. **Second**, when the receivers are spaced so far apart their electromagnetic couplings to their local environments will differ. The consequence is a random component to the driving point impedance of each antenna element in the giant array, which appears as a random complex gain or weight in each signal channel of the imaging system. **Third**, the system will be paced by a local oscillator distribution subsystem that must remain frequency- and phase-locked. With a system of radio camera size it must be assumed that oscillators will drift and, similarly, that electronic circuits in the receivers will change their complex gains with age. **Fourth**, impedance mismatches throughout the system will introduce further random amplitude and phase errors in the signal channels. **Fifth**, these random errors can, and in all likelihood will, vary with time.

In principle each of these distorting effects can be tuned out. In practice dynamic self-calibration is required. Such techniques have been developed at VERC during the last several years and the comparison between the performances of several of them is the subject of this report.

The second category of difference between radio camera design and the design of optical instruments is due to the vast differences in the scattering properties in the two wave bands. Most manmade surfaces are rough to optical radiation and therefore broadly scatter optical energy in all those directions not prohibited by geometric shadowing. By and large those same surfaces are smooth to microwave radiation and reflect more or less specularly. Thus most surfaces appear black in a microwave image, and when they do show up they do so as highlights or specularities. As a consequence the dynamic range is 50 to 90 dB in a microwave image, whereas it is only 20 to 30 dB in an optical scene even in bright sunlight on a beach or in snow. Weak scattering from edges and corners of targets, which tend to define their shapes, become obscured by the strong specular returns.

Another problem resulting from the prevalence of specular reflections is that their sidelobe responses coherently interfere to produce a random speckle pattern in the image. The effect is an unrealistic "texture" to the target image. Still another problem resulting from destructive interference is a random cancellation of image signals at the edges or peripheries of targets. The effect is to make large targets appear as groups of smaller ones.

Several techniques are applicable here. One is diversity combining of images obtained from radiation patterns with statistically independent side radiation patterns. A second is image deconvolution to remove the specular returns. A third is post-image-formation digital pixel processing. This topic is not central to this report, however, and will not be discussed further.

The third category of difference in design between microwave and optical imaging systems is in propagation and weather effects. The atmosphere is not wholly transparent in either waveband. Internal waves in the atmosphere induce local variations in the refractive index, which distort wavefronts. For an aperture to perform at its diffraction limit its size must be sufficiently small for a wavefront arriving at it to appear planar. That is, its size must be less than the correlation distance of the refractive index variations of the propagation medium at the wavelength at which it operates. The lens size in common optical instruments such as the eye, the camera and the small telescope meet this condition, although larger telescopes such as the 200 in Hale telescope on Mount Palomar do not. It is questionable whether a 5 km microwave antenna would satisfy this requirement. Failure to meet this condition means that the antenna array is confronted with a phase-perturbed wavefront and the measured signals in each receiver channel has some unknown phase error caused by it. A dynamic self-calibrator of the array would also solve this problem.

In addition to propagation-induced phase errors an array as large as the one under discussion is likely to experience different weather conditions across it. The nominal size of a rain cell is about 5 km. Consequently, one portion of the array could be in sunlight while it could be raining in another part of the array. Water pouring over the radomes covering some of the receivers could induce random phase shifts to the waves passing through. Again, dynamic self-calibration solves this problem.

Thus the radio camera is a bistatic, high resolution imaging system with a large, intrinsically distorted antenna and electrical system, both of which are dynamically self-calibrated. The generic term for the various self-calibration algorithms is **adaptive beamforming (ABF)**.

Figures 1.2 to 1.4 illustrate other uses. Figure 1.2 shows an airborne radio camera. The antenna elements are flush-mounted in the skin. Notwithstanding the vibration of the skin and the flexure of the airframe the ABF subsystem in the image processor compensates for the distortion and the output image is from a diffraction-limited system. The interesting feature of the airborne radio camera is that large jet aircraft are as large as the human eye when measured in units of wavelength. Consequently the image displayed to the navigator would have the same angular resolution as the human optical system. Such a passing-scene display with human optical resolving power would be available to the airman at night as well as during the day and under all weather conditions.

Figure 1.3 depicts a battlefield surveillance problem. A distant transmitter on a hill is shown illuminating a target region of interest. A large receiving array is hurriedly deployed, perhaps from the tailgate of a truck. Phase and frequency synchronization information is radioed from the transmitter to each of the receiver modules. The locations of the free-standing microwave receivers are known only crudely. Yet ABF forms and focuses a beam in the target region and scans the beam to obtain a high resolution image. If the target region is 10 km from the receiving array

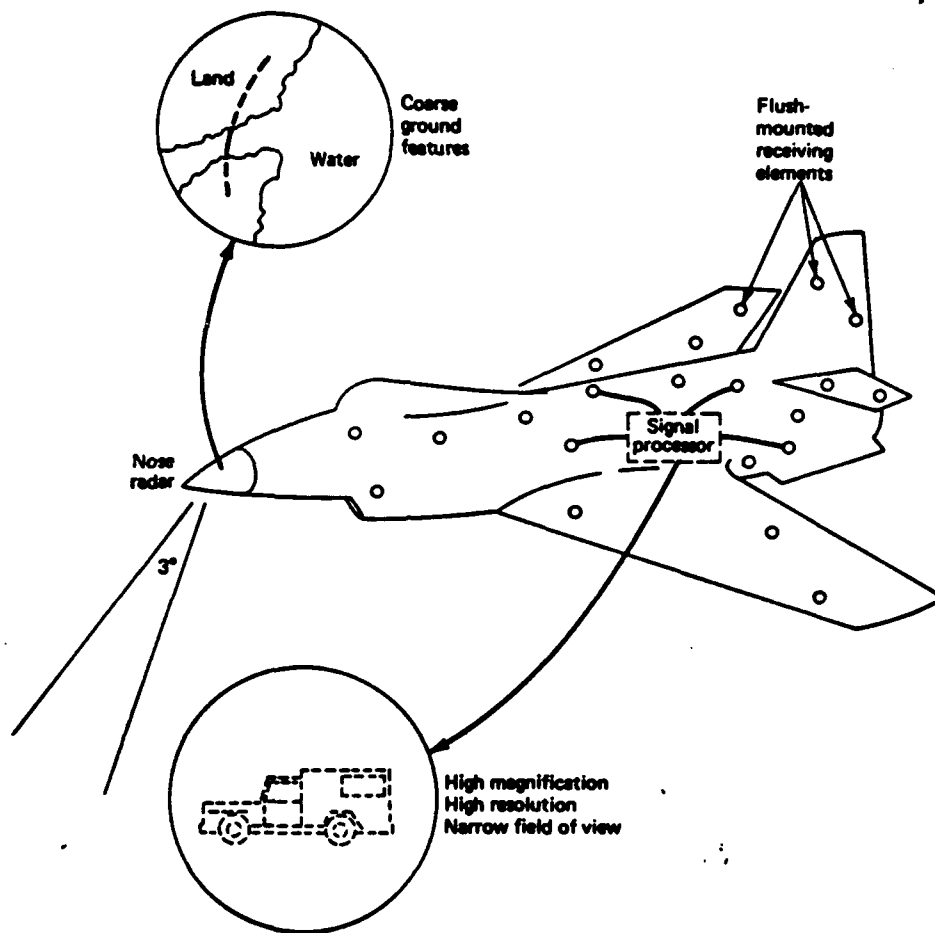


FIGURE 1.2. AIRBORNE APPLICATION OF THE RADIO CAMERA. ANTENNA ELEMENTS ARE DISTRIBUTED THROUGHOUT THE AIRFRAME TO FORM A NONRIGID PHASED ARRAY. THE ELEMENTS RECEIVE GROUND ECHOES FROM THE TRANSMITTER IN THE NOSE RADAR. THE SIGNAL PROCESSOR COHERENTLY COMBINES THESE ECHOES TO FORM A HIGH RESOLUTION IMAGE OF THE PASSING SCENE BELOW THE AIRPLANE. BECAUSE THE AIRPLANE IS APPROXIMATELY AS LARGE AS THE HUMAN EYE (AS MEASURED IN WAVELENGTHS) THE RESOLUTION IN THE PASSING SCENE IS COMPARABLE TO HUMAN VISION AND IS AVAILABLE NIGHT AND DAY AND IN ALL WEATHER. (FROM [4].)

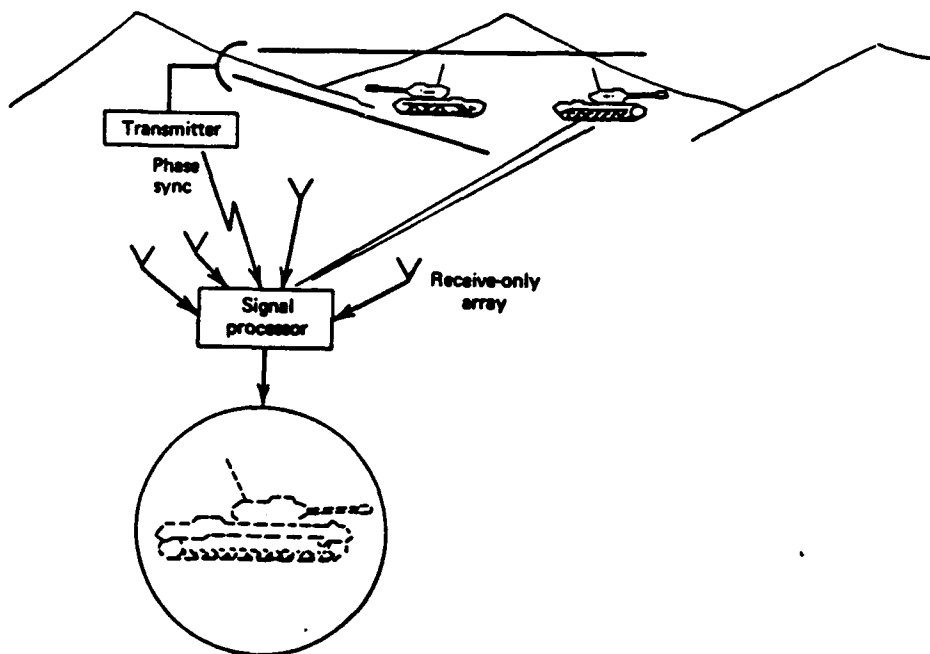


FIGURE 1.3. A BATTLEFIELD SURVEILLANCE APPLICATION OF THE RADIO CAMERA ILLUSTRATING ITS BISTATIC NATURE. THE TRANSMITTER IS SEPARATED FROM THE RECEIVING ARRAY AND ILLUMINATES THE TARGET AREA TO BE IMAGED. THE ARRAY IS HASTILY DEPLOYED AND THEREFORE IS ILL-SURVEYED AND BADLY DISTORTED. THE RADIO CAMERA FORMS A DIFFRACTION-LIMITED, HIGH RESOLUTION IMAGE OF THE SCENE. (FROM [4].)

and it is desired to obtain a 1 m cross-range resolution, the array must be 10,000 times the wavelength. Assuming X-band (3 cm) transmission the modules need be deployed over 300 m.

There is a highly favorable theoretical relationship between the size of the angular sector (called the field of view (FOV)) that may be scanned and the initial error or uncertainty in the locations of the antenna elements. Let σ be the standard deviation of element position error and let λ be the wavelength. Then the allowed position-error tolerance is [9]

$$\sigma = \lambda/2\pi(\text{FOV})$$

With conventional design the tolerance is approximately $\lambda/4\pi$. Therefore the tolerance in element placement is eased or loosened by the factor 2/FOV. In general, the FOV need be no larger than the target being imaged. In the ATC example of Figure 1.1 the minimum FOV = 30 m/3 km = 1/1000. This means that the tolerances (in manufacturing, installation, operation and maintenance) are eased by nearly three orders of magnitude in that example.

It is evident from the example shown in Figure 1.3 that the individual receivers of the radio camera could be on separate platforms. The platforms could be ground based, airborne or orbiting stations in space. Figure 1.4 illustrates a space-borne radio camera with loosely connected or tethered receivers. The central vehicle carries the transmitter in a low orbit which, for the sake of illustration, is taken to be at a height of 200 km. After unfurling from the station the receiver-carrying arms form a highly nonrigid 10 km array. If the wavelength is 10 cm the array is 100,000 wavelengths and the beam cross-section on earth is 2 m.

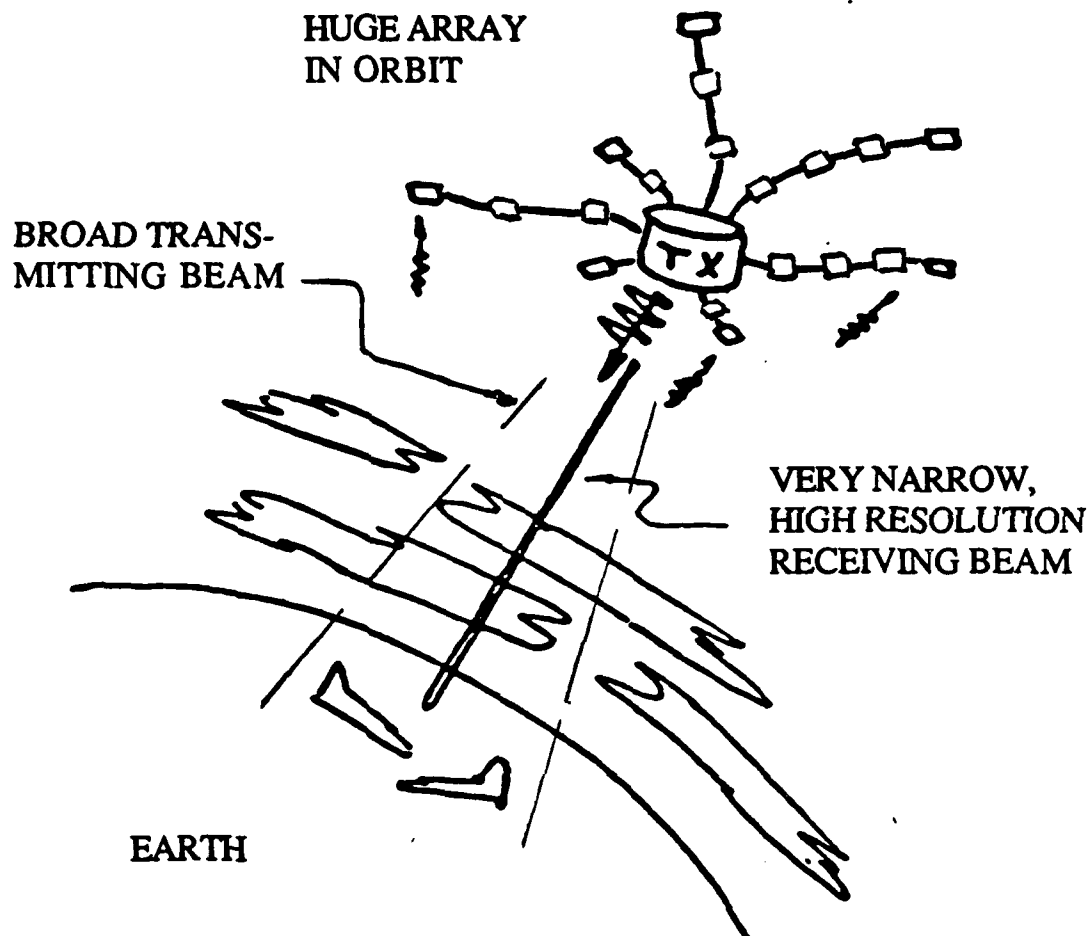


FIGURE 1.4. SPACE-BASED RADAR SURVEILLANCE APPLICATION OF THE RADIO CAMERA. A RADAR TRANSMITTER IN THE SATELLITE ILLUMINATES THE GROUND. RECEIVERS IN ARMS UNFURLED FROM THE SATELLITE DETECT ECHOES FROM EARTH. NOTWITHSTANDING THE DYNAMIC SHAPE VARIATION OF THE RECEIVING ARRAY THE RADIO CAMERA SIGNAL PROCESSOR FORMS A COHERENT, DIFFRACTION-LIMITED IMAGE OF THE AIR TRAFFIC BELOW. GIVEN THE ORBIT ALTITUDE AS 200 km, THE ARRAY SIZE AS 10 km AND A 10-cm WAVELENGTH, THE BEAMWIDTH OF THE RECEIVING ARRAY IS $10 \mu\text{rad}$ AND THE BEAM CROSS-SECTION ON THE EARTH IS 2 m.

This remarkable resolving power is potentially available from a space-borne radio camera.

2. ADAPTIVE BEAMFORMING (ABF)

Of the many problems encountered in long distance microwave imaging, one problem, that of aperture distortion, is in a category by itself: imaging with large apertures is not possible unless the problem is solved. As discussed in Section 1, the distortion is both geometric and electrical. These distortions are intrinsic to all systems sufficiently large to provide the resolution required of long distance, long-wavelength imaging systems.

Two sets of self-calibration procedures are described in the following two sections. Adaptive beamforming (ABF) is the generic term. Other names are self-cohering, self-calibrating, self-focusing, auto-focusing, self-phasing and self-synchronizing.

Adaptive control of the weight vector of a large phased array is in experimental use today in terrestrial high resolution microwave imaging as well as in radio astronomy. The radio camera was first described in a concept paper in 1973 [1]. The first radio camera experiment demonstrating ABF was performed two years later [2]. The algorithm upon which most subsequent radio camera experiments has been based was published in 1981 [3], with further details in 1983 [4]. The work reported in these and other references demonstrate that diffraction-limited imagery can be obtained from very large antenna arrays even when they are highly distorted.

Since the early part of this decade the same principle has been used in radio astronomy to correct for uncertainties in the loca-

tions of the phase centers of the dishes that form large radio astronomy arrays, as well as to compensate for wavefront distortion induced by spatial variations in the refractive index of the propagation medium. Review articles by Cornwell for the use of these procedures in radio astronomy are found in [5] and [6].

An interesting property of the radio camera is that it is a near-field instrument. In actuality its means of operation and its performance are independent of whether the target is in the near field or the far field. In practice, however, high resolution imaging implies near-field operation. The transition between the near field and the far field occurs at that distance at which the wavefront from a source, when viewed at the antenna array, changes from a quadratically curved front to an approximately planar front. This distance is in the neighborhood of L^2/λ , where L is the size of the aperture. At this distance the cross-range dimension of the resolution cell equals L . At greater distances the cross-range dimension is proportionally larger than L and at shorter distances it is proportionally smaller, assuming that the array is properly focused.

An easy test of near- vs. far-field operation of the radio camera is whether or not the cross-range resolution is smaller than or exceeds the antenna size. It is easy to see that for practical radar usage the imaging system must automatically and dynamically accommodate to near-field operation. The minimum available beamwidth is λ/L and the minimum available cross-range resolution for a system focused to range R is

$$\Delta S = \lambda R/L$$

A typical value of ΔS is 1 m. The typical range of radar target distances is a few to hundreds of km. The required aperture size is

$$L = \lambda R / \Delta S$$

which at 3 cm wavelength, a target distance of 3 km and for a required resolution of 1 m evaluates to 30 m. In this example the resolution cell is 30 times smaller than the aperture; hence the target is very deep in the near field (i.e., close to the antenna). In the space-borne illustration of Figure 1.4 the wavefront curvature is even more severe. There the relation of aperture size to cell size is 10 km to 2 m or 5000:1.

The practical significance of near-field operation is that the imaging system must focus to the target distance. The radio camera automatically performs this function in the process of adaptive beamforming. ABF, being designed to self-calibrate the system in the presence of arbitrary phase errors across the array, easily accommodates for the quadratic phase variation induced across the aperture by a near-field target. The two groups of ABF techniques that have been developed at VFRC compensate for aperture distortion and also focus the array at the target distance.

A distinction can be made between self-calibrating procedures according to whether they are local or global. A local procedure applies adaptive control to portions within the entire system to correct their errors, but fails to compensate for all the errors in the system. An example of local adaptivity is the use of a pilot signal, i.e., a known waveform at a known time, injected into the input of the RF section of a phased array. By measuring

the output signal it is possible to deduce the distortions in the receiving path and to transmit feedback control signals to the phase shifters and amplifiers for the purpose of compensating for these errors. This procedure will self-calibrate the receiver but will not correct for element position errors or the distortions caused by weather or propagation conditions.

Global adaptivity applies feedback control over the entire system, simultaneously correcting for propagation medium effects, geometric distortion in the aperture and phase errors in the distribution network.

Adaptive beamforming as applied to the radio camera is a globally adaptive procedure. Instead of introducing an artificial pilot signal into the receiver, as is the practice when local adaptivity is to be achieved, echoes from the target are used to derive the control for the phase shifters or the weight vector of the array. These echoes experience all the distortions mentioned above. They interact with medium turbulence and weather. Their phases are distorted by element position error. And they experience all the phase and amplitude errors due to circuit mistunings, component aging, oscillator drift, etc. It is these distorted signals that are converted into diffraction-limited images by ABF. To do so the system must correct all errors encountered by the echoes, not merely the ones induced in the receiver. Consequently, the ABF control procedure is global.

A companion procedure to ABF is called self-survey. The function of a self-survey procedure is to determine the locations of the parts of a large antenna system, for once the element posi-

tions are known, it is then possible to calculate the phase shifts required to form and point a beam in an arbitrary direction. A self-survey system employs a minimum of three, and typically four to six, beacons or transmitters. These sources are distributed in azimuth throughout the sector that the array is designed to scan. Either time of arrival or phase measurements of the beacon signals are made at each of the antenna elements. The number of measurements is sufficient to calculate the entire geometry of the system, i.e., the positions of all beacons and antenna elements.

Thus a two-step operation is involved: first is the survey of the system which is followed by beamforming and scanning. ABF is a more efficient procedure. It recognizes that the function of the antenna array is only the latter of the two operations performed by the self-survey technique. It bypasses the survey stage completely. It ignores where the elements are located and therefore eliminates the requirement to calculate their locations. It only makes those measurements that permit the system to adjust the phase shifts at each element to compensate for the position error. Furthermore, the requirement of the self-survey method that several beacons be deployed over the scanning sector, which limits the use of the procedure to fixed installations in which the user has control of the nearby terrain, is avoided completely. Instead, in the first of the two ABF procedures, only a single source in the general direction in which the system is scanning is needed. And experience shows that this source does not have to be a beacon or transmitter; in general, some scatterer in the field of view acts as a suitable replacement. Such a scatterer is called a beamform-

ing source. Even that modest requirement is eliminated in the second of the two ABF methods.

There are several desirable properties of an adaptive beamforming algorithm:

1. Independent of array geometry and distortion. The algorithm should be unconstrained by the locations of the elements or the errors in their positions. In simpler terms, the self-calibration procedure should operate successfully without regard to array design or the nature of the errors in the system. This is accomplished to a large extent in the algorithms described in the following sections.

2. Independent of source distribution. This highly desirable property is difficult to achieve. The algorithms described in Section 3 impose conditions upon the source distribution while those in Section 4 do not.

3. Passive. Adaptive beamforming is most desirable when applied in the passive mode, which means in the receiving system only. When self-calibration is accomplished in this manner, the transmitter and receiver functions are independent and the equipment need not be colocated. This permits bistatic operation (receiver and transmitter do not share a common aperture) and possibly the use of available on-the-air radiation to illuminate the target scene. All the algorithms have this desirable property.

4. All algorithms require calculations made from complex field measurements at the elements. To perform a calculation based upon all the measurements, there must exist within the system an intra-array communication subsystem to deliver the data to a common

point for computing. The preferred algorithms are those that minimize this additional burden upon an already complex system.

5. Noniterative. The calculations referred to above can be made at the element level or aperture plane of the array, which is prior to the image processor, or in the output or image plane following the image processor. Corrections for the errors are generally applied to the signals entering the image processor. Thus if the calculations are made in the aperture plane, they can be applied directly to the distorted signals. On the other hand, if they are derived from the output of the image processor and delivered to the input signals for correction, a new image must be formed before the corrections can be updated or a new weight vector formed. Such an iterative procedure across the image processor is costly in time and in the total amount of computation required. In general, a noniterative procedure is preferred.

6. Amplitude only. It would be highly desirable if amplitude measurements would suffice, for then the imaging system would simplify enormously. Detection would be by an envelope detector at each element. Without phase detectors there would be no need for frequency- and phase-locked local oscillators. And without such LOs there would be no need for an LO distribution system within the array. (See [4], chapters 5 and 8, for the system complexities that result from the need to preserve phase.)

No procedure has been discovered as yet that either works without phase information or that reconstructs phase from amplitude measurements made in a very sparse array. However, because long distance imaging is a near-field procedure in principle, there is

information in the modulus of the complex field measurement that might compensate for the missing phase information. The reason for his conjecture is as follows: When the target is in the far field the relative amplitudes of the element voltages in the array are independent of target distance. Not so in the near field, however, for there the phase and amplitude of the radiation field couple. This means that the set of amplitudes across the array due to radiation or reflection from a target scene that is located in the near field is a function of distance to the target. Consequently, amplitude measurements made at two or more distances from the target convey information about the scene that is normally carried only in the arguments of the measurements.

The second possibility - the reconstruction of phase from amplitude measurements - is a subject of current research. As this field matures, solutions may arise useful to the large array problem. One promising technique is reported by Tsao. Only 10% of the receivers in the array require phase measurement; 90% of the array consists of amplitude-only detectors [7].

3. DOMINANT SCATTERER ALGORITHMS (DSA)

3.1 ADAPTIVE BEAMFORMING ON A SINGLE DOMINANT SCATTERER

The primary procedure used at VFRC today assumes that there exists somewhere in the field of view (FOV) of the imaging system a point-like scatterer or source having large radar cross-section or source strength. The theory governing the requirement on cross-section or source strength is given in [8]. Such a target or source radiates a nearly spherical wavefront, thereby inducing a simple phase variation across the array. Provided that the array is linear or planar, the phase variation is linear if the target or the source is in the far field, or approximately quadratic when the source is in the near field. Deviations from such simple behavior indicate geometric distortion in the array, electrical mistunings or wavefront distortion due to turbulence in the propagation medium.

Consider a one-dimensional, far-field source distribution $s = s(u)$. Its radiation field in the axis of the array is

$$e = e(x) = F^{-1}\{s(u)\}$$

where the right hand side is the inverse Fourier transform of the source distribution $s(u)$, and $u = \sin\theta$ where θ is the angle from the normal to the array. For simplicity operation notation is used in the following development. F indicates the Fourier transform and F^{-1} its inverse. The electric field in the x -axis is then written

$$e = e(x) = F^{-1}s \quad (3.1)$$

Now imagine that the system could measure e and form a weight vector w equal to its conjugate:

$$w = w(x) = e^* = Fs^* \quad (3.2)$$

The radiation pattern of the system is the inverse transform of w , which is

$$f = f(u) = F^{-1}w = F^{-1}Fs^* = s^* \quad (3.3)$$

Thus the radiation pattern is the complex conjugate of the source distribution¹. The most interesting aspect of this procedure is that no account was taken of the shape of the antenna, the placement of its parts or geometric or electrical errors in the antenna. To utilize this relationship in an ABF algorithm, whereby the shape of the radiation pattern is the modulus of the angular profile of the source, it is necessary that there be at least one scatterer of small physical size that has a radar cross section (RCS) so large that its reflection dominates all the other scatterers in its range cell². A corner reflector is an example; its RCS is approximately T^4/λ^2 where T is the length of one side and its reflection profile approximates a δ -function. Let this reflector be at distance $r = r_0$. The source distribution at this range is

$$s_0 = s_0(u) = \delta(u-u_0) \quad (3.4)$$

where u_0 is the bearing to the dominant scatterer.

¹The weight vector is chosen as the complex conjugate of the electric field to ensure that the radiation pattern, when formed from the e -field of a point source, points to that source. This is called retrodirective beamforming. If the conjugate is not employed the beam points in the mirror or Snells-law direction.

²A range cell or range bin is an interval in range such that all scatterers within it return echoes that overlap in time in the receiver. Its nominal extent is $ct/2$ where c is the speed of light and t is the radar pulse duration.

Next, let the adaptive system recognize the presence of the single, dominant scatterer at $r = r_0$ (by the procedure described in Section 3.2) and form its weight vector from measurements of the radiation from that range. Then from (3.3) and (3.4)

$$f = f(u) \approx \delta(u-u_0) \quad (3.5)$$

is the radiation pattern of the antenna. When this radiation pattern scans the source distribution $s_i = s_i(u)$ at range R_i , the image delivered by the system is

$$\begin{aligned} \hat{s}_i &= \hat{s}_i(u) = \int f(x) s_i(u-x) dx \stackrel{\Delta}{=} f(u) * s_i(u) \\ &\approx \delta(u-u_0) * s_i(u) \\ &\approx s_i(u-u_0) \end{aligned} \quad (3.6)$$

Thus the output is an excellent replica of the target scene except for the unknown displacement angular u_0 .

We now introduce an antenna into the equations. Let the antenna be a phased array which is designed as a sampled aperture of finite length. Let the design location of the n th element be x_{0n} and the weight w_{0n} . The aperture, as designed, can be described by

$$w_0 = w_0(x) = \sum_{n=1}^N w_{0n} \delta(x-x_{0n}) \quad (3.7)$$

where the weights, as a rule, are real, and are selected to provide shaping to the side radiation pattern. Because of gain errors and aperture distortion, the actual weight vector differs from (3.7) and can be written

$$w(x) = \sum w_n \delta(x-x_n) \quad (3.8)$$

where

$$w_n = a_n e^{j\phi_n} \quad (3.9)$$

Now the weights have become complex. The w_n differ from the design values w_{on} primarily due to the phase errors in the system and the x_n differ from the x_{on} due to the geometric errors in the locations of the elements of the antenna. For the most part the moduli of the w_n do not differ significantly from the design values because the wavefront of the radiation from a point source is spherical; hence $a_n \approx w_{on}$.

The weight vector can be viewed as a transducer that converts the electric field across the aperture to a current $i = i(x)$ that drives the electronic system. i is given by

$$i = we = wF^{-1}s \quad (3.10)$$

Let the adaptive beamforming subsystem measure i and form a compensation or correction weight vector

$$c = c(x) = i^* = w^*e^* = w^*Fs^* \quad (3.11)$$

The composite weight vector is the cascade or product

$$wc = ww^*Fs^* \quad (3.12)$$

The term

$$\begin{aligned} ww^* &= \sum_n \sum_m w_n w_m^* \delta(x-x_n) \delta(x-x_m) \\ &= \sum_n w_n w_n^* \delta(x-x_n) = \sum_n a_n^2 \delta(x-x_n) \stackrel{\Delta}{=} w_1 \end{aligned} \quad (3.13)$$

is a sampling function having sample points at the actual element location x_n , and real weights a_n^2 , implying that the phase errors in the aperture have been eliminated. The composite weight vector

$$wc = w_1Fs^* \quad (3.14)$$

and the radiation pattern is

$$f = f(u) = F^{-1}w_c = F^{-1}w_1Fs^* = F^{-1}w_1 * s^* \quad (3.15)$$

where $F^{-1}w_1 \triangleq f_1(u)$ is the radiation pattern of the sampled aperture defined by (3.13). Assuming, as before, a source distribution at $r = r_0$ given by (3.4) and the composite weight vector (3.12) formed from measurements of the echoes from that range, the adaptively formed radiation pattern is

$$f(u) \approx f_1(u) * \delta(u-u_0) = f_1(u-u_0) \quad (3.16)$$

The key feature of (3.16) is that all phase errors have been eliminated by the adaptively-formed compensation weight-vector. The aperture weights a_n^2 are real, as they should be. They differ from the design values w_{on} . However, because of the approximate relationship $a_n \approx w_{on}$, that difference can be easily corrected by modifying the initial w_{on} to $\sqrt{w_{on}}$ to account for the fact that the final weights are a_n^2 . Alternately the correction can be introduced in the signal processing computer. The simplest procedure (used for all VFRC imaging) is to set $w_{on} = 1$ for all n , and to perform the desired aperture tapering upon the stored data records in the computer. With this procedure the square-root relationship between the weights of w_1 and w_0 is avoided and an arbitrary taper most suitable to the particular imaging problem can be applied.

3.2 THE RADIO CAMERA

The adaptive, retrodirective beamforming procedure described above is the key to the design of the radio camera. The radio camera is a large imaging system that operates at wavelengths very large compared to optics, and its large size implies that it suffers from distortions in its shape and in errors in the loca-

tions of its parts. Propagation and circuit errors are assumed as well. The means for applying the procedure given in the preceding section is described in detail in Chapter 5 of [4] and in [3]. Figure 3.1 illustrates the logic by which calibration information is extracted from the radiation field from a target. A point source or target, identified as a phase synchronizing source in the sketch, reflects a transmitted pulse toward the array. Because of the small size of the target, it reradiates a spherical radiation field, meaning that the amplitude and phase are constant on any sphere centered on the synchronizing source. Assuming free-space radiation, the complex field amplitudes measured by the elements of, say, a linear or planar array, would have equal moduli. Their phases, however, would be random and meaningless because of the geometrical distortion, even with element position errors as little as several tenths of a wavelength. Any circuit mistunings or mismatches would further distort the measured phases. The system compensates for the phase distortion across the aperture by comparing the phases measured at the various elements and deriving feedback-control signals from them to drive the first bank of phase shifters so that the signals passing through the phase shifters are all cophased (described below). Doing so phase shifts each receiver channel by the negative of the received signal. Because the amplitudes are equal and the phase shifts are the negatives of the measured signal phases, the weight vector is the complex conjugate of the field measurements. The first bank of phase shifters and the circuit that controls it is the calibration or compensation subsystem. The sum of the cophased signals is

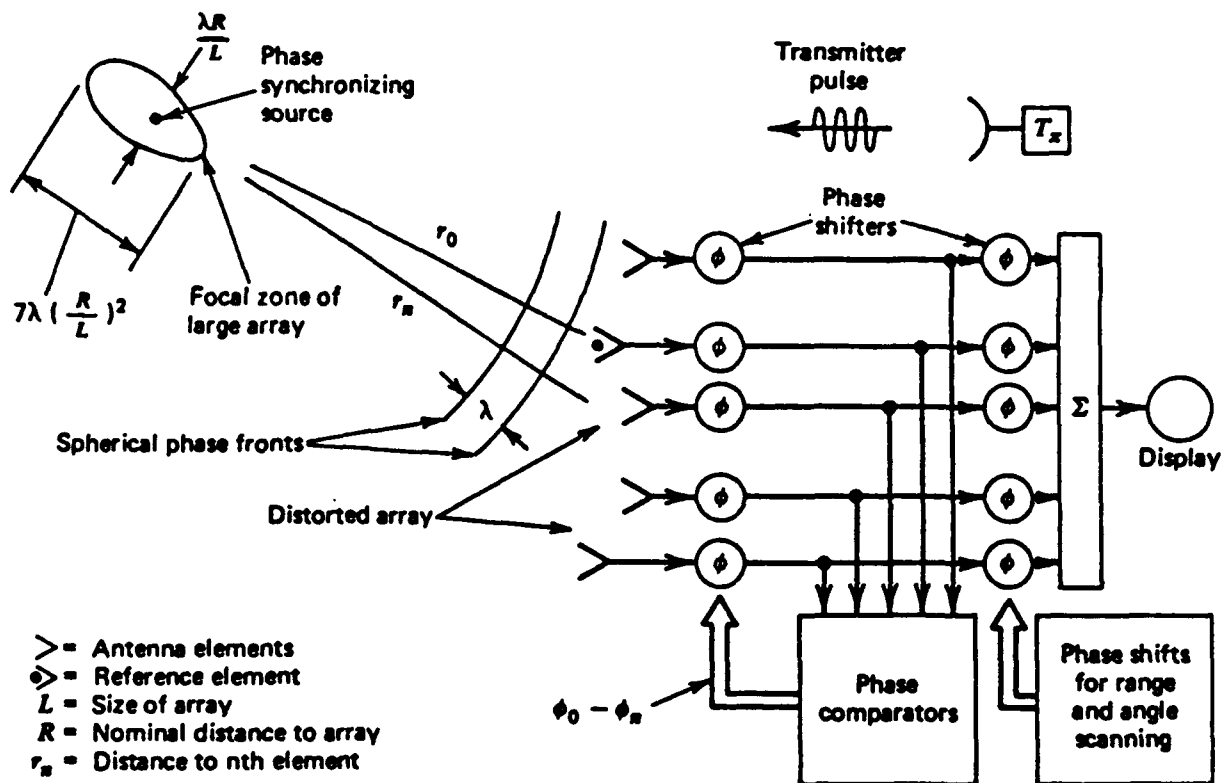


FIGURE 3, 1. Distorted array self-coheres on a phase-synchronizing source: > = antenna elements; ▷ = reference element; L = size of array; R = nominal distance to array; r_n = distance to nth element. (From [4].)

that of an array focused on the phase synchronizing target. The two-dimensional radiation pattern of the array is centered at this point. The beam cross section in the focal zone is $\frac{\lambda R}{L}$ in the lateral or cross-range dimension and approximately $7\lambda(R/L)^2$ in the range or longitudinal dimension.

Once the beam is formed, a second set of phase shifters can scan it to form a map or an image of a target. In essence, the inputs to the second bank of phase shifters can be viewed as the outputs of antenna elements of a properly designed, error-free array. Scanning is an open-loop procedure, exactly as in a conventional phased array. The extent to which scanning can be accomplished is limited, however, by the amount of geometrical distortion in the array. This is because only a single beamforming source is used to calibrate the system. The calibration is correct in the direction of the beamforming source and at its distance. Residual distortions develop as the beam is scanned away from the location of the beamformer. Errors in the array in the direction of the beamforming source and at its range are fully compensated. The errors which dominate under scanning are the distortions in the axis of the array [4, Section 7.3]. (Experiments supporting the theory are found in the same reference.) Errors normal to the array direction and to the direction to the beamforming source have a relatively minor effect.

The tolerance theory for scanning in the near field of the array is given in [4, Section 7.5]. There it is shown that the maximum scan angle from the focal point is

$$\theta_{\max} = \frac{\lambda}{4\pi\sigma_x} \quad (3.17)$$

where σ_x is the standard deviation of a zero-mean random variable in the x-position of each of the antenna elements in the array. Equation (3.17) is derived on the assumption that the maximum nominal tolerance on the loss of array gain is 1 dB. The angular field of view is twice θ_{\max} given by (3.17) and the cross-range dimension of the sector that may be scanned by the adaptively formed beam is R times this value, as given in (3.18):

$$\Delta S = 2\theta_{\max}R = \frac{\lambda R}{2\pi\sigma_x} \quad (3.18)$$

The extent in range ΔR over which the beam may be scanned is much larger. It is shown in [4, Section 7.5] that the ratio of the dimensions of the scanning sector is given by

$$\frac{\Delta R}{\Delta S} = \frac{\sqrt{12} R}{L} \quad (3.19)$$

where R is the range to the focal zone and L is the size of the array. In general, $\Delta R \gg \Delta S$ because normally $R \gg L$. Thus the position-error limitation to scanning is most heavily felt in the cross-range or angle direction.

The two banks of phase shifters in Figure 3.1 indicate only that two distinct functions must be performed. These functions can be performed in hardware or within a computer. The procedure used at VFRC is illustrated in Figure 3.2. A search procedure is indicated by which the imaging system discovers the phase synchronizing source, which is a critical operation for the success of the system.

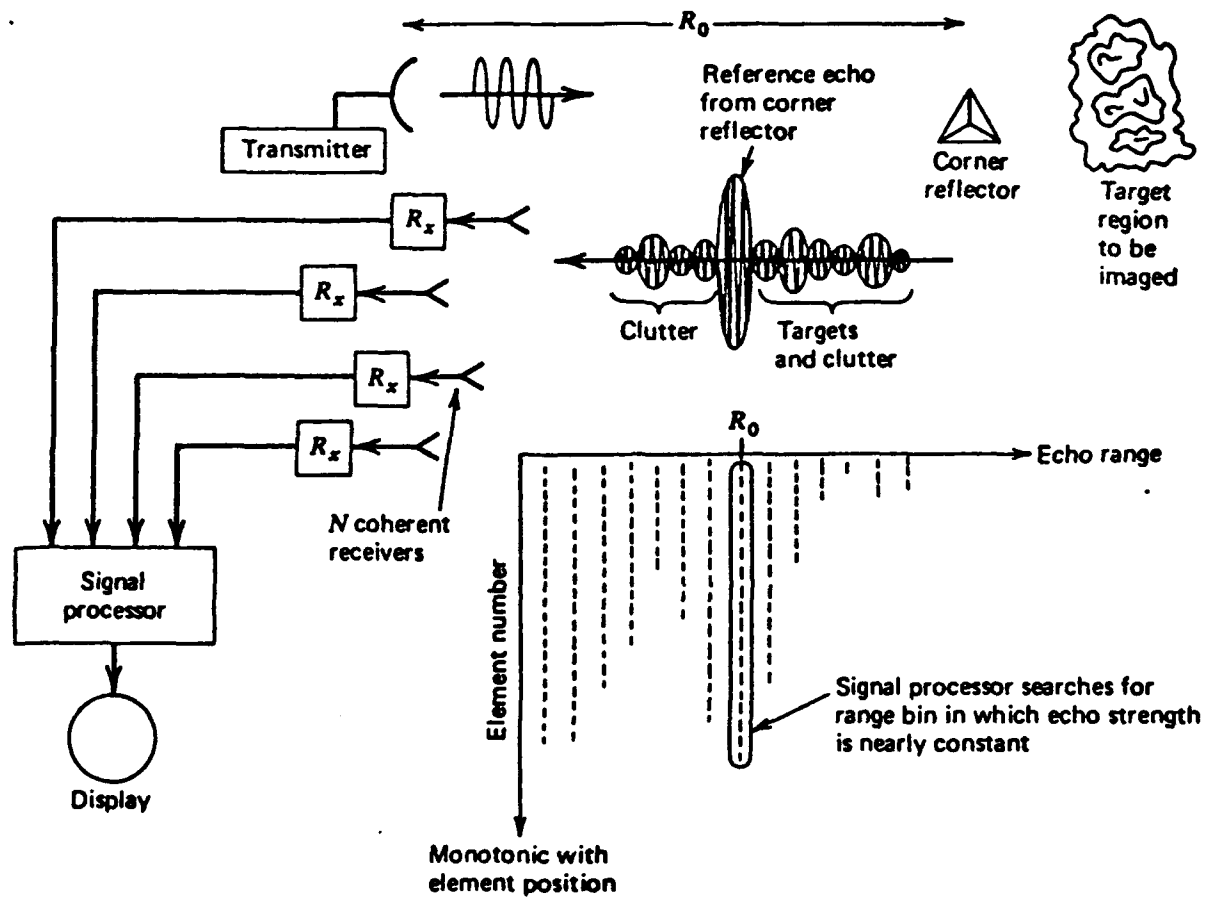


FIGURE 3.2. Radio camera data format and procedures. (From B. D. Steinberg, *IEEE Trans. Antennas and Propagation*, Ap-29, No. 5, September 1981.)

The search procedure is based upon a minimum amplitude variance (MAV) test upon the echoes streaming across the array. Referring to Figure 3.2, a transmitter launches a pulse toward a target area, in which is embedded a small target of large radar cross section. A corner reflector is illustrated in the figure, although experience shows that it is rarely needed because targets of opportunity having appropriate scattering properties are plentiful (Section 3.5). The reflected echo from the range bin containing the reference target is dominated by the reflection from that target. The distorted array consists of antenna elements followed by receivers that coherently detect and demodulate the signals. The data are sampled and stored as shown in the lower right of the figure. The sampling interval is approximately the pulse duration. Each row of data is the echo trace received by a single element. Successive rows correspond to successive elements in the array. Each column of data is called a range bin. The data represent a snapshot of the radiation field from sources at a distance corresponding to the time of arrival of those signals. For simplicity, it is assumed that range walk or range-bin slippage has been corrected.

To locate the range bin in which the target most closely resembles a point source, the signal processor calculates the normalized variance of the measured amplitudes of the signals received across the array in each range bin. The range bin with the smallest variance is chosen, for that echo sequence most closely approximates the expected field from a point source. Designate that range by R_0 . The weight vector adopted by the system is the

complex conjugate of the complex column vector of signals received at that range. It is shown in Chapter 6 of [4], and also in [8], that the reference target echo need be no more than 4 dB greater than noise and clutter in that range bin for successful phase synchronization of the array to be achieved.

Table 3.1 describes the algorithm. The measured signals from the i th range bin at the n th element, corrected by the shape of the element pattern, are $A_i \exp(j\psi_{in})$. Step 3 finds the reference range R_0 in which the amplitudes A_{0n} are nearly equal. Because the A_{0n} are nearly equal, the measured value at the n th element can be written approximately as $A \exp(j\psi_{0n})$. Its conjugate $A \exp(-j\psi_{0n})$ is the weight vector. Step 4 gives the phase-corrected signals in the 0th range bin. The corrected i th term is proportional to $A_i \exp[j(\psi_{0n} - \psi_{in})]$ (Step 5).

This term has now been corrected for array distortion. It also has been corrected for the near-field curvature of the phase-front associated with the distance R_0 to the phase synchronizing source. Step 6 alters the phase curvature by replacing the quadratic phase variation of the reference range by the proper curvature for the i th range bin, and similarly for all other bins. Following this step, the beam may be scanned in angle, for it is now in focus at all ranges. Steps 7 and 8 complete this process.

High resolution imaging implies that the resolution cell in the transverse dimension is smaller than the array. The target always is in the near field and the array must therefore be focused. Adaptive beamforming automatically focuses the array to R_0 (step 5). However, it is rarely necessary to perform step 6

TABLE 3.1. Steps in Radio Camera Imaging [4]

Step		
1	Measure and store complex envelopes of echo samples	$V_{in}e^{j\psi_{in}}$
		range bin \nearrow \nwarrow element number
2	Correct amplitudes by dividing by element pattern estimate \hat{f}_n	$A_{in}e^{j\psi_{in}}$
3	Find R_0 such that $A_{0n} = A$, all n	$Ae^{j\psi_{0n}}$
4	Phase rotate at R_0 by phase conjugate in relation to reference element, $\exp j(\psi_{00} - \psi_{0n})$	$Ae^{j\psi_{00}}$
5	Phase rotate at all range elements	$A_{in}e^{j(\psi_{in} - \psi_{0n} + \psi_{00})}$
6	Focus at each range R_i	$A_{in}e^{j(\psi_{in} - \psi_{0n} + \psi_{00} + (kx_n^2/2)(1/R_i - 1/R_0))} \triangleq B_{in}$
7	Phase shift linearly with angle	$B_{in}e^{-jkx_nu}$
8	Sum at each range element	$\hat{z}_i(u) = \sum_{n=1}^N B_{in}e^{-jkx_nu}$

which refocuses the array simultaneously to all range bins. At most it is necessary to refocus in steps of 100s of meters. This is because the depth of field of an array usually is larger than the extent in the range dimension of the sector being imaged.

The depth of field of an aperture (array, lens, dish, etc.) is the extent in range over which the aperture is nominally in focus and is approximately $7\lambda(R/L)^2$ [9]. The cross-range resolution is approximately $\Delta S = \lambda R/L$. Combining,

$$\text{D.O.F.} = 7\lambda \left(\frac{R}{L}\right)^2 = 7\lambda \left(\frac{\Delta S}{\lambda}\right)^2 = \frac{7}{\lambda} (\Delta S)^2.$$

Given a 3-cm system focused to a 1-m beam cross section, the depth of field is about 200 meters.

Figure 3.3 (top) illustrates the spatial distribution of scatterers of various sizes located at some range R . The illustration to the left shows a group of small scatterers of random sizes and locations. This distribution models statistically homogeneous clutter, uniformly distributed throughout the illuminated sector. On the right one large target or scatterer has been added. The bottom sketches picture the difference between the phasefronts of the fields received at the array for the two cases. The phasefront on the left is a sample of a zero-mean random process whereas the phasefront on the right has a well defined slope determined by the bearing from the array to the large scatterer. Superimposed on the average phasefront is a perturbation field caused by the radiation from all the remaining, small scatterers in the range bin.

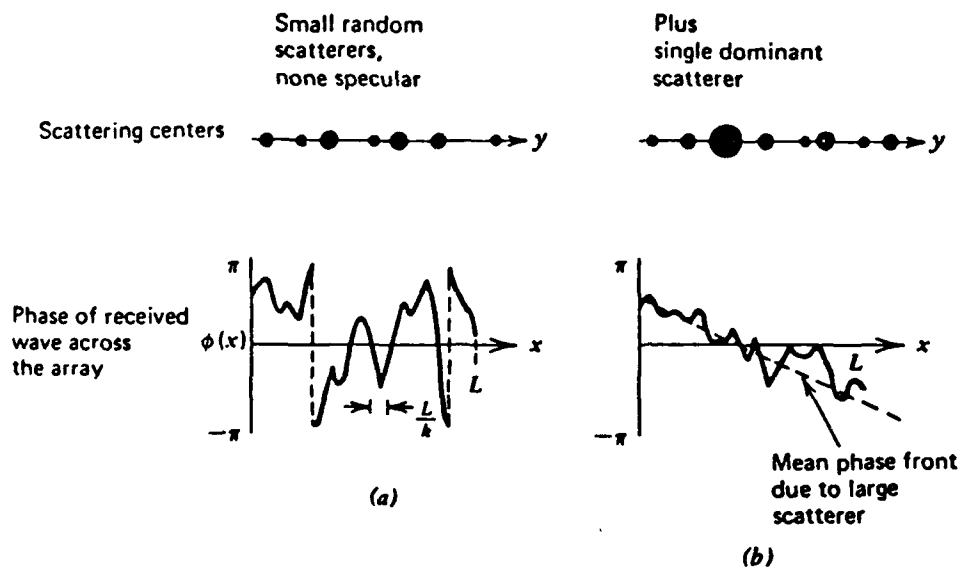


Figure 3.3 Phase distributions across array. From Steinberg, J. *Franklin Inst.* (December 1973).

The argument that follows is based upon plane wave propagation, but it is equally valid in the near field. The sum of the waves emanating from the scatterers is the radiation field at the receiving array. Only those scatterers illuminated by the transmitting beam contribute to the reradiation field. Call the source function of this field $\rho(u)$. We can write this source function

$$\rho = \rho(u) = f_T(u) s(u) \quad (3.20)$$

$f_T = f_T(u)$ is the radiation pattern of the transmitter and

$$s = s(u) = \sum_i s_i \delta(u - u_i) \quad (3.21)$$

is the scatterer distribution, s_i and u_i being the complex strength and bearing of the i th scatterer. The electric field in the receiving array is

$$\begin{aligned} e &= e(x) = F^{-1}\rho \\ &= F^{-1}f_T * F^{-1} \sum_i s_i \delta(u - u_i) \\ &= w_T * \sum_i s_i \exp(jkxu_i) \end{aligned} \quad (3.22)$$

where w_T is the aperture excitation of the transmitter and F^{-1} means inverse Fourier transform. The electric field is the sum of randomly weighted (by the s_i) plane waves arriving from random directions u_i , each convolved with w_T .

Let l be the size of the transmitting antenna and L the size of the receiving antenna. The transmitted beamwidth $\Delta\theta_T \approx \lambda/l$ and the width of the clutter patch illuminated at range R by the beam is $\Delta s = \lambda R/l$. The reradiation is lobular with typical lobe width $\lambda/\Delta s = l/R$. At the receiver, also a distance R from the clutter patch, the lobe cross section is $(l/R)R = l$, which is approxi-

mately the separation between such lobes. These $L/1$ lobes across the receiving array are statistically independent because they are derived from the Fourier transform of a band-limited random process. Thus the phase of the e-field across the receiving array is a band-limited random variable characterized by the order of $L/1$ random values in the interval $[-\pi, \pi]$. Such a field is useless for phase synchronizing the receiving array.

The situation changes dramatically when a large radar cross section (RCS) reflector is added (upper right). The sum of the scattered fields from the clutter does not change, but added to it is the strong plane wave from the prominent scatterer. The e-field can be written

$$e = e(x) = s_0 \exp(jkxu_0) + \sum_i s_i \exp(jkxu_i) \quad (3.23)$$

in which the first term dominates. This field can be viewed as a perturbed plane wave, i.e., its direction of arrival is approximately u_0 , meaning that its phase slope is nearly but not exactly ku_0 at every point. The phase of the e-field (3.23) is

$$\begin{aligned} \phi_x &= \tan^{-1} \frac{s_0 \sin kxu_0 + \sum_i s_i \sin kxu_i}{s_0 \cos kxu_0 + \sum_i s_i \cos kxu_i} \\ &= kxu_0 + \tan^{-1} \left[\frac{\sum_i s_i \sin kx(u_i - u_0)}{s_0 + \sum_i s_i \cos kx(u_i - u_0)} \right] \end{aligned} \quad (3.24)$$

The sum field from the random scatterers can be called

$$A(x) \exp j\alpha(x) = \sum_i s_i \exp(jkxu_i) \quad (3.25)$$

With $A \ll s_0$ throughout the array when s_0 is large compared to the sum of all the other scatterers,

$$\begin{aligned}\phi_x &\approx kxu_0 + \tan^{-1} \left\{ \frac{A(x) \sin \alpha(x)}{s_0} \right\} \\ &\approx kxu_0 + \frac{A(x)}{s_0} \sin \alpha(x) \\ &= kxu_0 + \delta\phi(x)\end{aligned}\tag{3.26}$$

where $\delta\phi(x)$ is the deviation of $\phi(x)$ from kxu_0 .

Equation (3.26) is the phase available to be measured by the system for self-calibration of the array. The first term is the linear phase term with constant slope, which is the desired term. The second term is the error phase. The dominant field due to s_0 need exceed the scattered field (3.25) by no more than 6 dB to enable the dominant scatterer algorithm (DSA) to extract the phase information it needs with adequate accuracy to form and scan a main beam [4, Section 7.6].

The procedure is summarized in the mathematics that follows. Consider a linear array with N elements located at (x_n, y_n) , $1 \leq n \leq N$. The y_n are the deviations in the element positions in the array that are to be corrected by the adaptive beamforming procedure. Let β'_n , $1 \leq n \leq N$, $0 \leq |\beta'_n| \leq \pi$, denote the electronic phase error at each of these elements. These errors are caused by mistunings, impedance mismatches, oscillator drifts, etc. Assume that somewhere in the FOV of the imaging system there exists a range bin containing a single dominant scatterer plus clutter. Let R_0 denote the distance of this range bin from the origin, which is assumed to be located at the first element ($x_1=y_1=0$) (see Figure

3.9). Let the bearing to the scatterer be $u_o = \sin\theta_o$, where θ_o is the angle measured clockwise from broadside to the array.

The phase of the echo from the R_o range bin measured at the n th receiver is

$$\phi_{o,n} = -kr_{o,n} + \beta_n + \delta\phi_{o,n} \quad (3.27)$$

where $k = 2\pi/\lambda$, $r_{o,n}$ is the distance from the beamforming scatterer (also called adaptive beamforming source, beamformer or reference target) to the n th receiver, and is equal to

$$r_{o,n} = [(x_n - R_o \sin\theta_o)^2 + (y_n - R_o \cos\theta_o)^2]^{1/2} \quad (3.28)$$

β_n is the electronic phase error at the n th receiver and $\delta\phi_{o,n}$ is the phase perturbation in the spherical wavefront of the beamforming scatterer due to clutter and noise.

The Fresnel approximation for the distance $r_{o,n}$ can be used in most microwave imaging scenarios. Further, the perturbation of the n th element in a direction perpendicular to the array, y_n , will be much smaller than its location along the array, i.e., x_n . Expanding (3.28) in a Taylor's series and ignoring all terms other than the linear and quadratic terms in X and Y yields

$$r_{o,n} = R_o - x_n u_o - y_n (1 - u_o^2)^{1/2} + x_n^2 (1 - u_o^2) 2R_o. \quad (3.29)$$

A similar expression pertains to any other range bin. Thus, $r_{m,n}$, the distance from a scatterer in the m th range bin to the n th element, is found from (3.29) with all 'o' subscripts replaced by 'm'.

The signal phase $\phi_{m,1}$ at the array origin is treated as a reference phase for the mth bin and is subtracted from all the phases measured in the array, thereby removing the target distance R_m . In the reference range bin R_0 , the difference phase at the nth element is (substituting (3.29) into (3.27))

$$\begin{aligned} \phi_{o,n} = \phi_{o,n} - \phi_{o,1} = & k\{x_n u_0 + y_n(1 - u_0^2)^{1/2} \\ & - kx_n^2(1 - u_0^2) / 2R_0 + \beta_n - \beta_1 + \delta\phi_{o,n} \end{aligned} \quad (3.30)$$

where $\delta\phi_{o,n} = \delta\phi_{o,n} - \delta\phi_{o,1}$. The negative (or conjugate phase) of (3.30) is the phase shift introduced into the nth channel to compensate for array distortion and electrical phase errors in the receivers. This is the ABF process.

It is desirable to combine the second, fourth and fifth terms to form a phase error $\beta_n = \beta_n - \beta_1 + ky_n(1 - u_0^2)^{1/2}$ and to treat it as being nearly independent of the viewing angle of the imaging system. The phase errors β_n and β_1 are electronic errors and therefore are independent of viewing angle. The last term, on the other hand, is not; it is an explicit function of the angle, which for any scanning problem can vary only over the width of the imaging sector. However, the FOV of most microwave imaging systems is narrow because the transmitter beamwidth is typically the order of a few degrees. Hence this error may be assumed to be independent of this small variation. Consequently, summing the electronic phase error $\beta_n - \beta_1$ and the perturbation error $ky_n(1 - u_0^2)^{1/2}$ gives

a phase error β_n that is almost independent of the beamformer direction u_0 . Using $\beta_n = \beta'_n - \beta'_1 + ky_n(1 - u_0^2)^{1/2}$ in (3.30) yields

$$\phi_{0,n} = \frac{kx_n u_0 - kx_n^2(1 - u_0^2)}{2R_0} + \beta_n + \delta\phi_{0,n}. \quad (3.31)$$

The first two terms point and focus the array to (u_0, R_0) . The third term, β_n , is the phase error from the R_0 bin caused by electrical phase distortion and element position errors. Except for the small variation across the FOV, this error is constant for all range bins; hence its inclusion in the weight vector of the array eliminates the primary source of distortion. The fourth term is caused by clutter and noise. Because the clutter-induced phase perturbation is not constant from range bin to bin, the $\delta\phi_{0,n}$ term does not compensate for this source of phase error. Let $\delta\phi_{m,n}$ be the clutter-induced phase perturbation in the m th range bin; then $\delta\phi_{m,n} - \delta\phi_{0,n}$ is the residual phase error after adaptive beamforming and is responsible for the loss in mainbeam gain and the rise in the sidelobe level that result from the ABF process.

The n th component of the phase-compensating weight vector is

$$w_{n,DSA} = \exp(-j\phi_{0,n}) \quad (3.32)$$

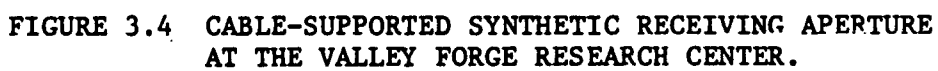
Thus the DSA phase corrections compensate for both electronic phase errors and perturbation of the receivers along the Y-axis; however, they are contaminated by clutter and focus the array to u_0 and not to the center of the FOV, which we may call \bar{u} . Focusing the array to u_0 leads to a pointing error $\bar{u} - u_0$ in the target location estimates. The multiple scatterer algorithm (MSA), described

in Section 3.5, reduces the clutter noise in the phase corrections and yields a better estimate of the target location.

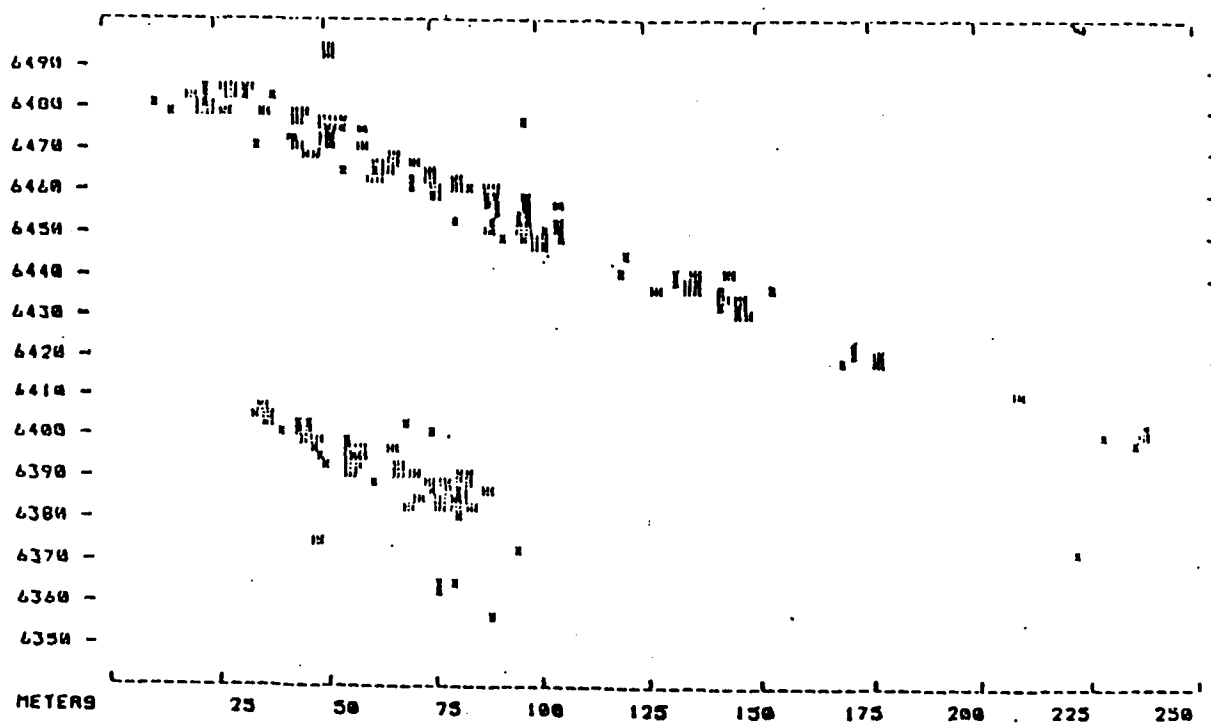
3.3 DSA EXPERIMENTS

Radio camera images have been made with the DSA applied to data from three experimental facilities. The first is a cable-supported synthetic receiving array 83 m in length. This array is 2500 wavelengths at the 3 cm wavelength at which it was operating. Its resolving power is comparable to human vision. The experimental procedure is shown schematically in Figure 3.4. A single receiver was moved along a cable 10 m above the ground. The cable was 83 m long and supported only at the ends and center. The radar transmitter was directed approximately normal to the array. The receiver with 1 ft dish was pulled from end to end in approximately two minutes. It was turned on 330 times at predetermined locations as it moved over the 83 m course. The estimated uncertainty in antenna location at each of the sample points was the order of 1 wavelength rms.

Figure 3.4A shows images made with this array. The scene is of rows of houses on streets in the town of Phoenixville with and without adaptive beamforming. The same microwave data were used to form these images. The dominant scatterer adaptive beamforming algorithm was used to form the upper image. Careful examination of the image data shows that the "corrected" array was operating diffraction limited. The lower picture, without adaptive beamforming, is a useless array of pixels. The image of the housing development in Figure 3.4B was also made with this array.



ADAPTIVE BEAMFORMING



NONADAPTIVE BEAMFORMING

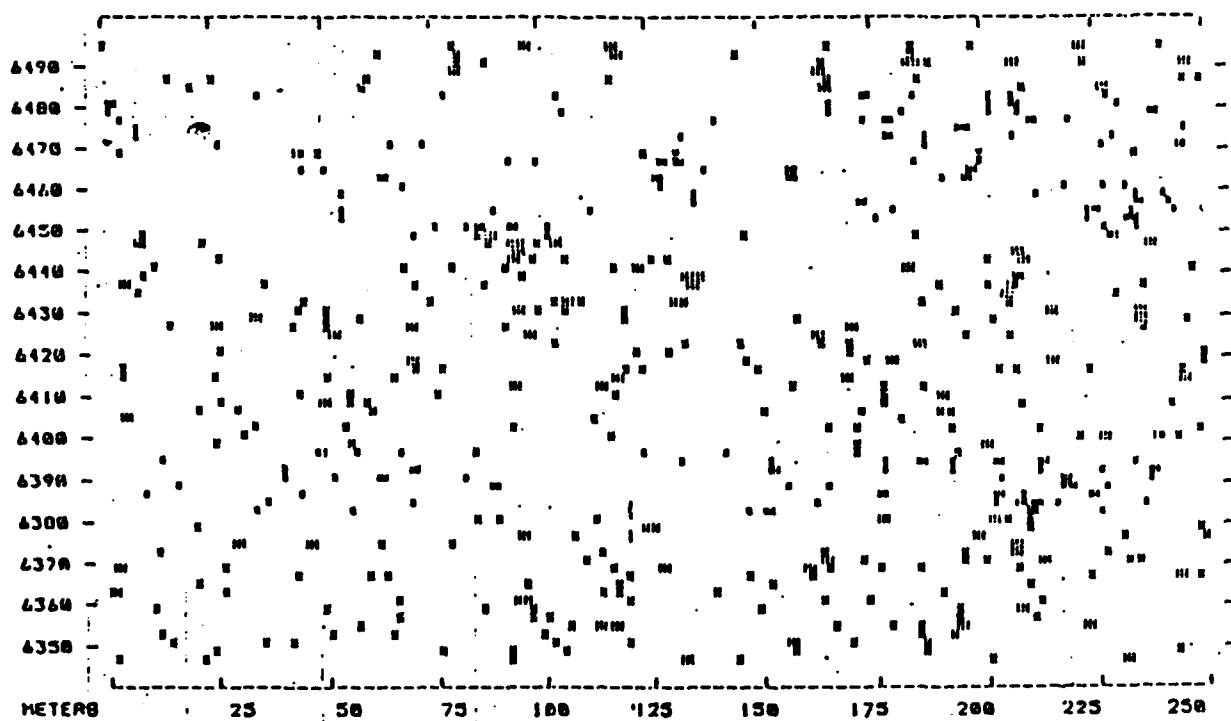


FIGURE 3.4A IMAGES OF HIGH STREET, PHOENIXVILLE, PA, WITH AND WITHOUT ADAPTIVE BEAMFORMING.

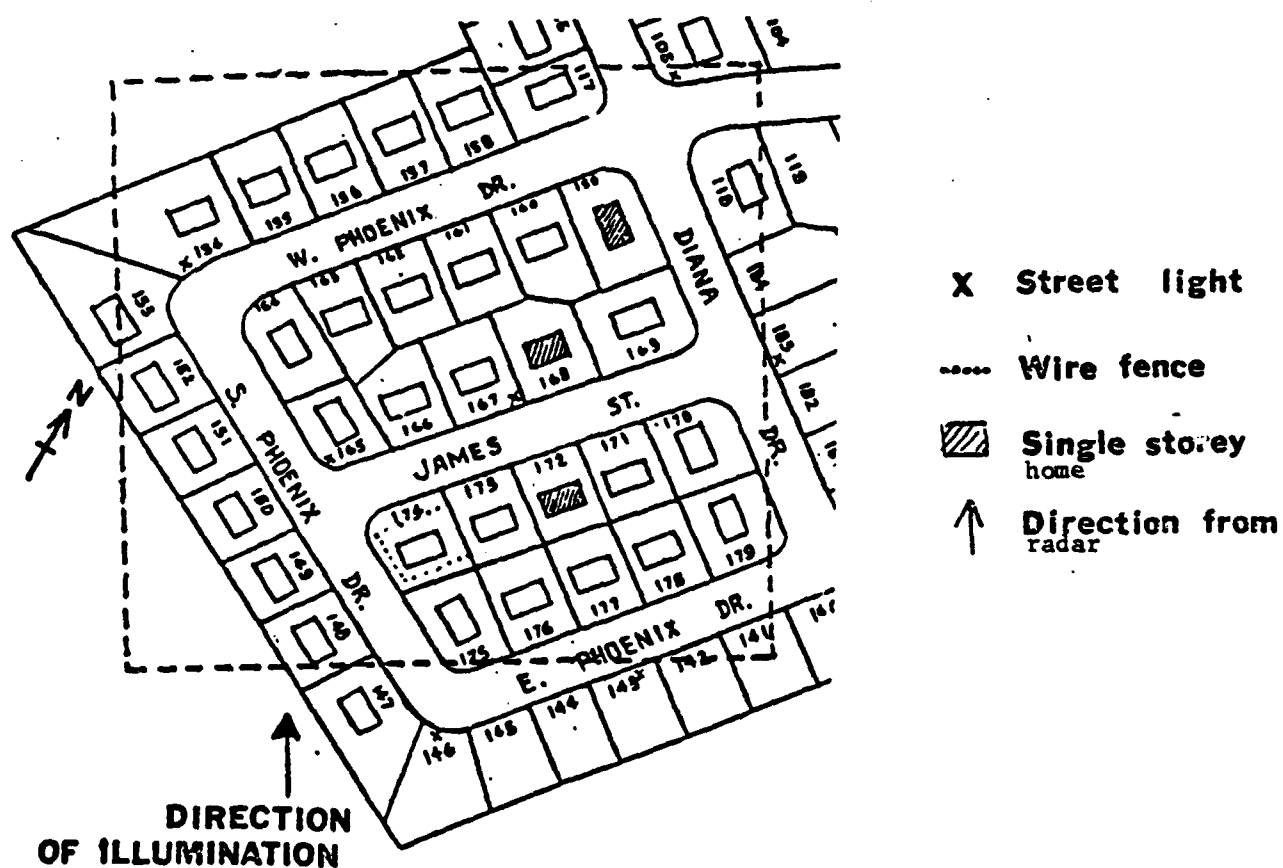
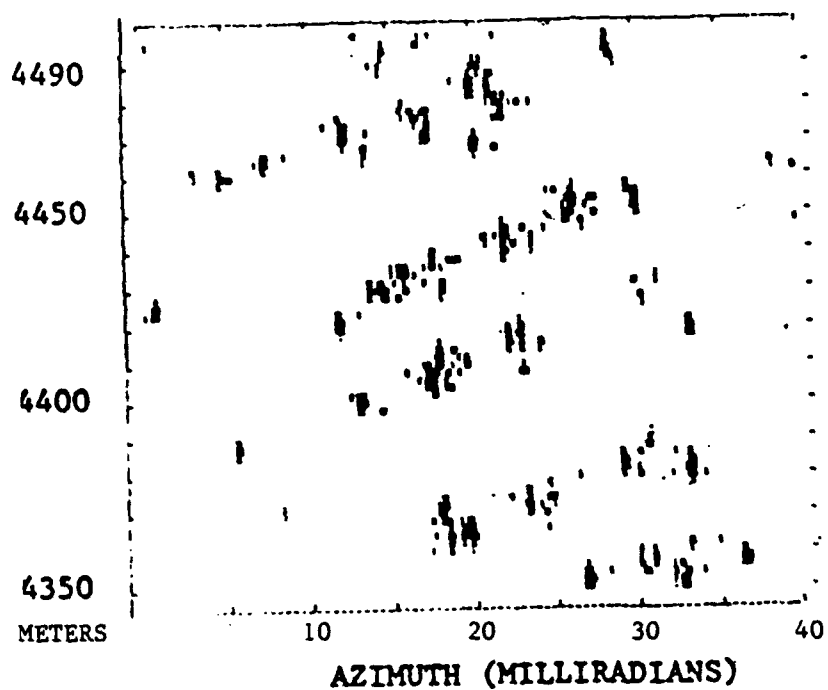


FIGURE 3.4B DIFFRACTION-LIMITED 3 cm RADAR MAP OF SUBURBAN HOUSING DEVELOPMENT, PHOENIXVILLE, PA., SHOWING STREETS AND HOUSES. EACH PIXEL CLUSTER IS A HOUSE. THE HOUSES ARE ABOUT 20 m APART. RESOLUTION IS COMPARABLE TO HUMAN VISION. THE ARRAY LENGTH IS 83 m.

The second facility was a physical aperture consisting of 32 X-band (3 cm) receivers each with 12 in horns (Figures 3.5A and B). The receivers were spaced by approximately 1 m, the element placements being inaccurate over the 32 m course of the array. The receivers were placed on a laboratory roof and were not bolted to a common platform. The upper portion of Figure 3.6 is a picture of a Boeing 727 flying at a distance of 3.2 km from the laboratory made with this array. The lower portion shows the same data without adaptive beamforming. The importance of the self-calibration procedure again is evident.

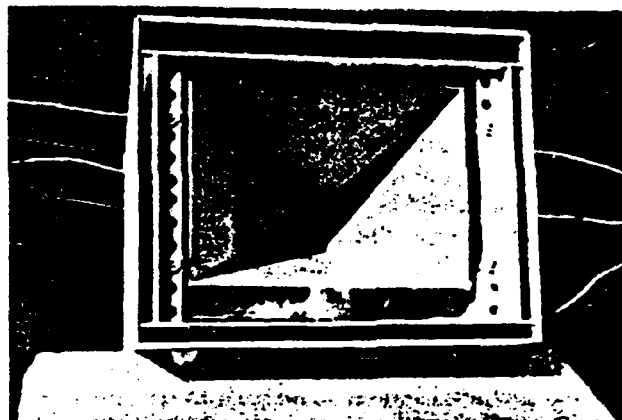
A third facility is a single, monostatic X-band radar used in an ISAR mode. Figure 3.7 shows the pedestal and 1.2 m dish antenna. The flexible waveguide connecting the antenna to the equipment in the laboratory is visible. Figure 3.7A is a pair of images made from a common set of data with and without adaptive beamforming. The location of the antenna did not change from pulse to pulse in this experiment. The distortion instead was due to the perturbations in the flight path of the airplane target due to wind turbulence (Figure 3.8). Adaptive beamforming corrected the distortion (upper figure); without it, the echo data produced a hopeless jumble of pixels.

3.4 BEAMFORMER STATISTICS

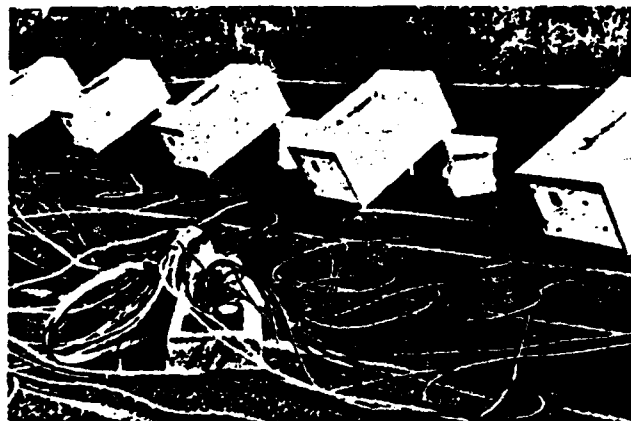
Dependence upon implanted corner reflectors as adaptive beamforming sources is unrealistic. Practical system design requires that echoes from targets themselves serve for the self-calibration process. Three studies have been conducted of the frequency of occurrence of targets of opportunity that can serve as beamforming



Fig. 3.5A 32-element microwave array. Each module is a microwave receiver at 3-cm wavelength. The mean spacing is one meter. The elevation look angle of each module is approximately 30°. Placement and pointing were done by eye. This array is highly distorted relative to the nominal 0.1λ standard tolerance in array design. This distortion is responsible for the poor imaging performance shown in Fig. 3.6 (c); it is electrically corrected by adaptive beamforming, as is demonstrated in Fig. 3.6 (a). (From [22].)

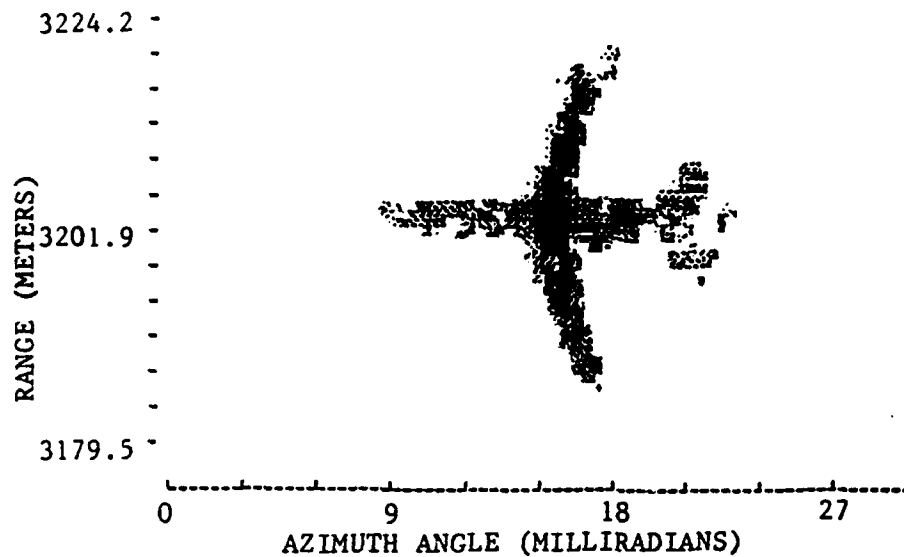


FRONT VIEW

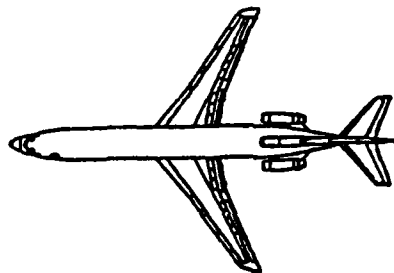


REAR VIEW

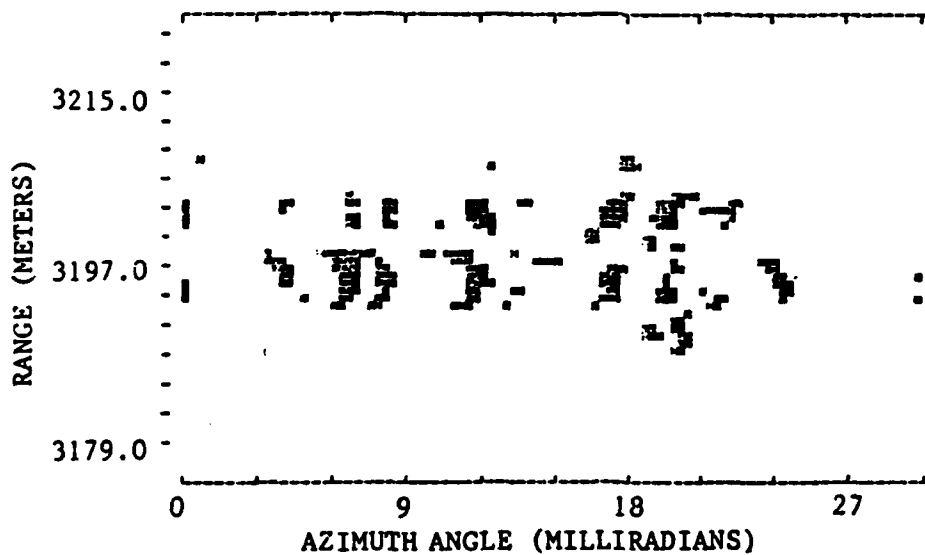
FIGURE 3.5B. FRONT AND REAR VIEWS OF ARRAY MODULES. (FROM [22].)



(a)
WITH ADAPTIVE
BEAMFORMING



(b)
PLAN VIEW DRAWING
OF AIRCRAFT

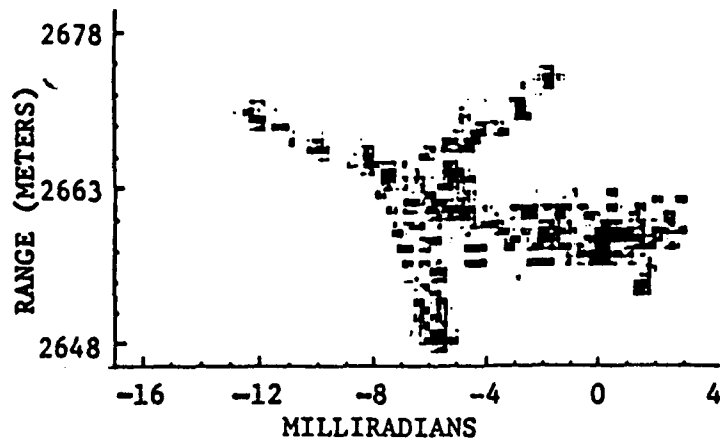


(c)
WITHOUT ADAPTIVE
BEAMFORMING

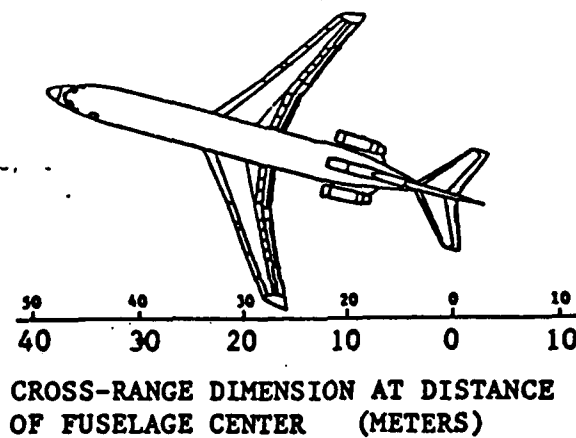
FIGURE 3.6 MICROWAVE IMAGE OF BOEING 727 OBTAINED WITH 32m X-BAND RADIO CAMERA. AIRPLANE IS FLYING AT DISTANCE OF 3.2 Km FROM VALLEY FORGE RESEARCH CENTER. (From [22].)

PHOTO NOT AVAILABLE

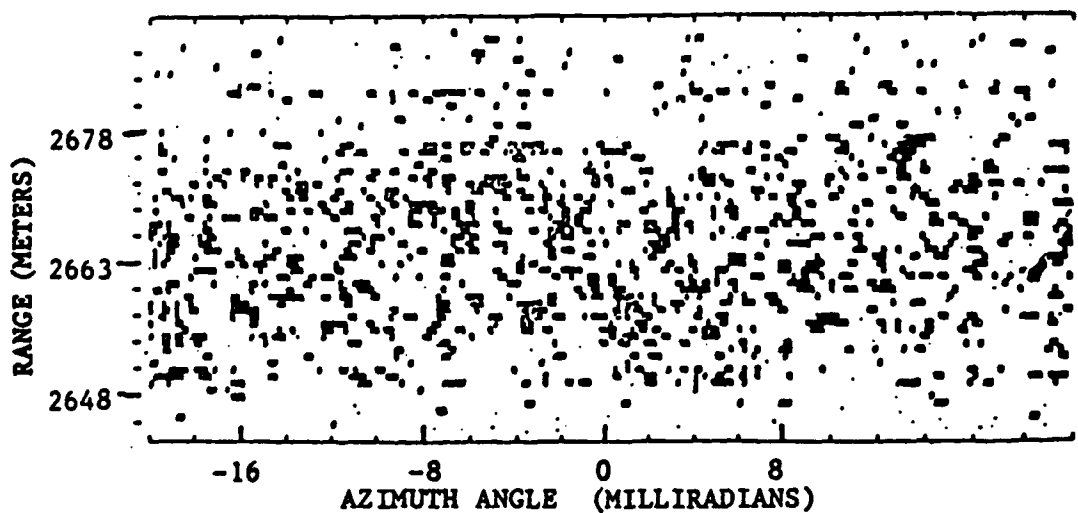
FIGURE 3.7 MONOSTATIC X-BAND RADAR USED FOR ISAR
IMAGING, SHOWING PEDESTAL AND 1.2 m DISH.



(a)
WITH
ADAPTIVE
BEAMFORMING



(b)
PLAN VIEW
DRAWING OF
AIRCRAFT



(c)
WITHOUT
ADAPTIVE
BEAMFORMING

FIGURE 3.7A. MICROWAVE IMAGE OF BOEING 727 OBTAINED AT X-BAND WITH MONOSTATIC RADIO CAMERA. AIRPLANE IS FLYING AT DISTANCE OF 2.7 Km FROM VALLEY FORGE RESEARCH CENTER (From [22].)

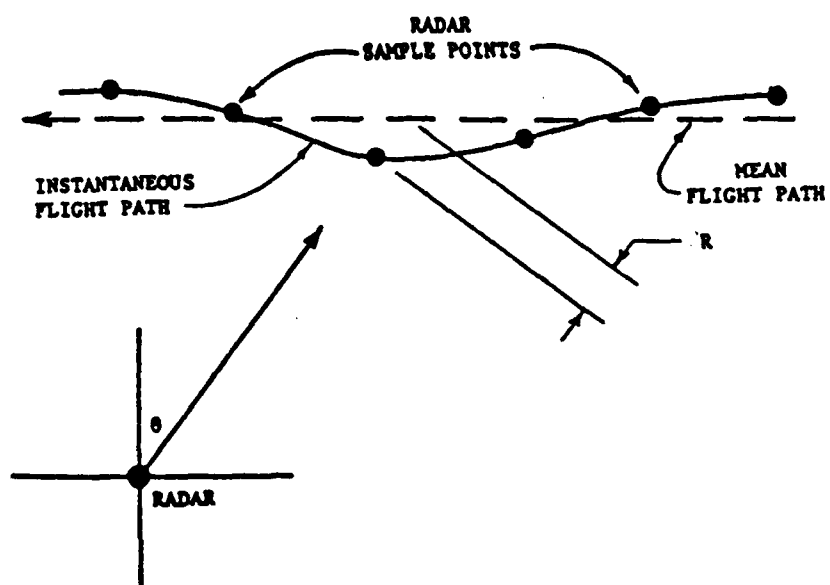


FIGURE 3.8 FLIGHT PATH DISTORTION IN ISAR.

sources. The first, by Yadin, examined airborne radar data obtained by the Naval Research Laboratory in the upper UHF band (850 MHz) [10]. The data were radar ground clutter obtained from an 8-element receiving system flown at 200 knots over the southeastern portion of the United States at an altitude of 15,000 to 20,000 ft. Because the antenna array was a rigid structure with known characteristics, it was possible to compare the adaptively formed radiation pattern based upon the ground clutter with the intrinsic pattern of the antenna itself. This comparison was made from echoes from a large number of range bins. The criterion of whether or not a particular range bin contained a suitable adaptive beamforming source was determined by the rise in the sidelobe level; an acceptable range bin was one for which the sidelobe level rose no more than 3 dB. Based upon this arbitrary criterion, it was found that approximately 10% of the range bins were acceptable candidates for adaptive beamforming. In view of the fact that at most one range bin per radar trace is needed for the ABF process and that at the most one trace per beamwidth is necessary, the observed frequency of occurrence is encouraging.

A second study also examined the frequency of occurrence of beamforming sources amidst echoes from ground targets. The experiments are in ground-to-ground imaging at very low grazing angles [11]. The array sketched in Figure 3.4 was employed. Radiation was in the X-band. Data were obtained at distances of 4-7 km from farmland, and residential and industrial areas from a town. The results are shown in Table 3.2. These results are not as opti-

mistic as the observed frequency of occurrence in the airborne case but are nevertheless very satisfactory.

BEAMFORMERS		
<u>RUN TYPE</u>	<u>AVAILABLE</u>	<u>DETECTED</u>
Industrial	16.9%	5.8%
Residential	11.6%	1.3%
Undeveloped	2.7%	1.8%

TABLE 3.2. VARIANCE TEST EFFECTIVENESS (FROM [11]). All VALUES
RELATIVE TO TOTAL NUMBER OF BINS PROCESSED. $\sigma_{Ni}^2 \leq 0.12$.

<u>RANGE CELL</u>		
	<u>1 m</u>	<u>3 m</u>
% SUCCESS	87%	28%
NUMBER OF EXPERIMENTS	18	11
NUMBER OF SNAPSHOTS	68	36

TABLE 3.3 PERCENTAGE OF AIRCRAFT IMAGING EXPERIMENTS IN WHICH
ADAPTIVE BEAMFORMING WAS SUCCESSFUL.

The primary differences between the experiments were the grazing angles and the criteria of acceptability of ABF range bin data. The airborne grazing angle was a few degrees while the ground-to-ground grazing angle was nearly zero. The criteria of acceptability were also different. In the airborne experiment, a range bin was accepted when the radiation pattern adaptively formed from its echoes had satisfactory sidelobe properties. A more sophisticated measure was chosen for the ground-to-ground experiments. First, a corner reflector was used to form the weight vector at the array, after which an image of a target sector was obtained. This image is the reference image. Second, the echoes from each range bin were used to obtain a set of trial weight vectors, and an image was formed from each one. Next, the correlation coefficient between each trial image and the reference image was calculated. The criterion for acceptability was a correlation coefficient in excess of 0.88, a value obtained by a subjective viewing test using 63 subjects [12].

Both tests lead to optimistic inferences. Typically there are hundreds of range bins in a radar trace. Thus, when the frequency of occurrence of acceptable range bins is few per cent, the probability is nearly unity that a suitable target of opportunity will be found.

A third study of a different nature involves adaptive beam-forming and imaging on aircraft, which are isolated targets. Here the question is the fraction of aircraft snapshots obtained during the passage of a target through the transmitter beam for which a single range bin proves suitable, i.e., for which imaging can be

performed. Table 3.3 shows the results of observations made from approximately 100 data sets obtained from about 30 experiments at the Valley Forge Research Center. The results are very satisfactory for the shorter pulse duration. The reason that they were less satisfactory for the longer pulse duration is that the probability that a single dominant scatterer exists in any single range bin decreases rapidly with the size of the range cell.

While these results are satisfactory on the average, they do not guarantee the successful use of this algorithm at all times. A more robust procedure is described in the next section that increases the probability of success still further. Moreover, the dominant scatterer algorithm with the minimum amplitude variance test is sure to fail under those circumstances in which no dominant scatterer exists. An example is the backscatter from the surface of the sea. Fields of vegetation, crowns of trees and large extents of sand are in a similar category. In these cases, the backscatter is statistically homogeneous and a different type of algorithm is required. Section 4 addresses this problem.

3.5 MULTIPLE SCATTERER ALGORITHM (MSA)

When no high quality adaptive beamforming source is found, a form of range-bin diversity sometimes can be employed to synthesize a useful ABF source. The echo data from several range bins are combined to produce a superior weight vector to what would be available from any of the individual range bins. A modification to the DSA was invented by Attia to deal with this situation [13]. Experiments were reported in [14]. The method is called by its in-

ventor the robust minimum variance algorithm (RMVA); here it is called the multiple scatterer algorithm (MSA).

Conceptually, the procedure works as follows: in Figure 3.9 there is a transmitter of beamwidth $\Delta\theta$ illuminating a set of isolated scatterers in different range bins. These scatterers are called candidate beamformers, meaning that none is suitable for adaptive beamforming by itself, but that together a satisfactory virtual beamformer can be synthesized. Amplitude and phase data are recorded at each element in the array for each of these range bins. The algorithm proceeds as follows. The range bin for which the echo amplitudes at the various receivers in the array have the smallest variance is selected as the reference bin R_0 , as in the earlier algorithm. Second, the phases $\phi_{0,n}$ of the received signals from R_0 are subtracted from the phases $\phi_{m,n}$ of the signals of M candidate bins, thereby removing the random phase errors β_n , again as in the former algorithm. With the β_n deleted, the difference phases form quadratic sequences, modulo 2π , across the array. These phase sequences are then "unwrapped" by removing the modulo 2π discontinuities. While the unwrapped phases are corrected for the aperture distortion, there remain residual phase errors caused by the clutter. These clutter-induced residual phase errors are unbiased and therefore can be reduced by averaging. Averaging yields $\frac{1}{M} (\sum_m^M (\phi_{m,n} - \phi_{0,n})^u)$, which is the averaged unwrapped phase of the difference phases of the M candidate beamformers from the reference ABF bin at the n th element. The superscript 'u' means unwrapping.

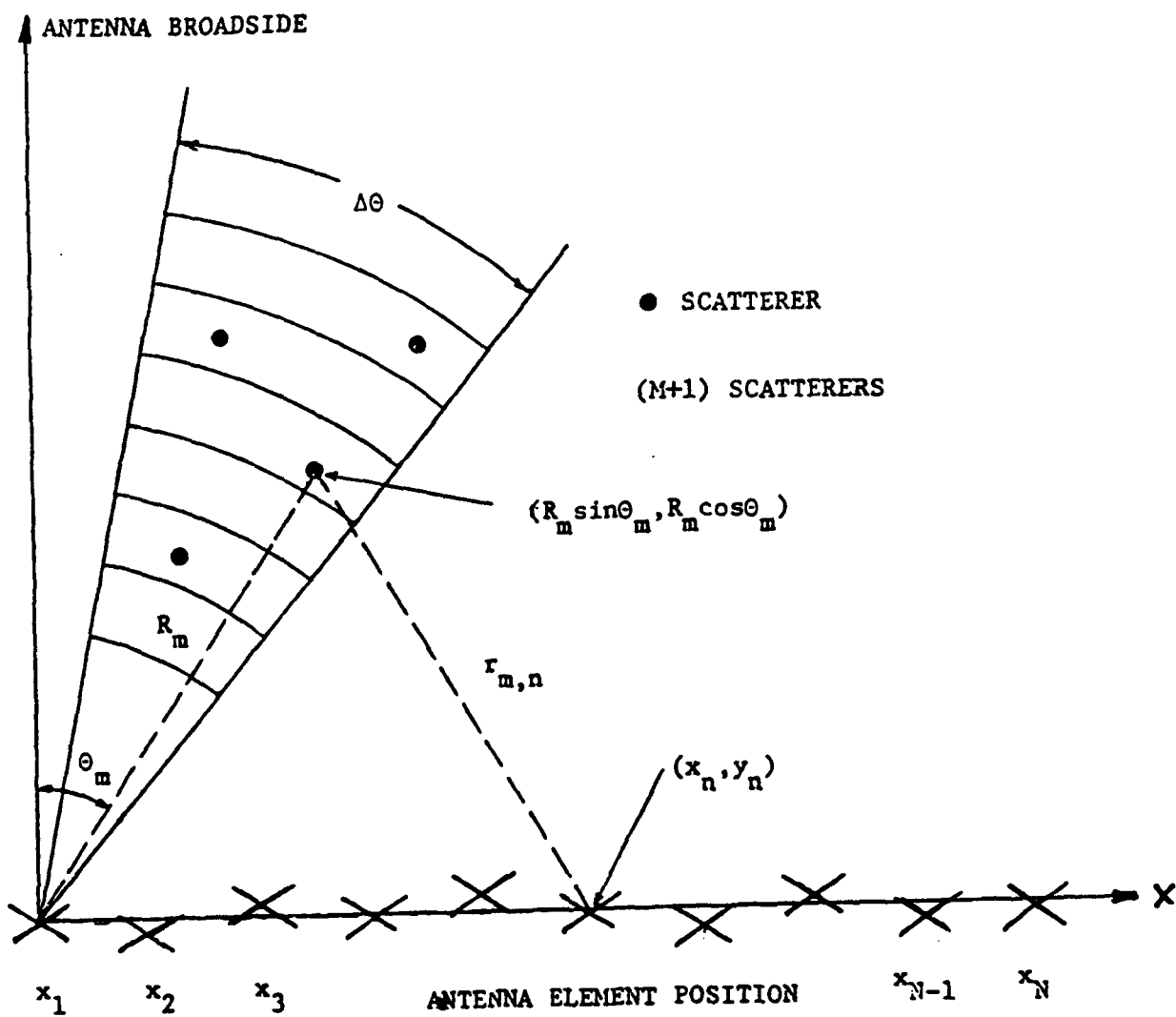


FIGURE 3.9 ANTENNA ARRAY AND TARGET GEOMETRY. (FROM [24].)

The steps can be summarized as follows:

1. Find R_o .
2. Form $\phi_{m,n} - \phi_{o,n}$ to remove β_n .
3. Unwrap $\phi_{m,n} - \phi_{o,n} = (\phi_{m,n} - \phi_{o,n})^u$ to remove modulo 2π ambiguities.
4. Take the average $\frac{1}{M} \{ \sum_m^M (\phi_{m,n} - \phi_{o,n})^u \}$ of the unwrapped phases to reduce the variance of the clutter-induced residual phase errors.

Each of the range bins is assumed to contain a single scatterer embedded in clutter where the scatterer is not sufficiently large to operate the DSA. We call such a scatterer subdominant. In none is the target-to-clutter ratio adequate for the DSA to operate satisfactorily. There are $M+1$ such scatterers. Let R_m , $1 \leq m \leq M+1$, be their distances from the origin and $u_m = \sin\theta_m$ their directions relative to the normal to the array. The geometry is shown in Figure 3.9. The mathematics of Section 3.2 can be carried over directly from the DSA to the MSA by replacing all subscripts "o", denoting range bin R_o , by "m", denoting range bin R_m . $\phi_{m,n}$ is found in this manner from (3.31). The difference phases are obtained by

$$\begin{aligned} \phi_{m,n} - \phi_{o,n} = & [kx_n(u_m - u_o) - kx_n^2 \left(\frac{1}{2R_m} - \frac{1}{2R_o} \right) \\ & + kx_n^2 \left(\frac{u_m^2}{2R_m} - \frac{u_o^2}{2R_o} \right) + \delta\phi_{m,n} - \delta\phi_{o,n}]_{\text{mod } 2\pi} \end{aligned} \quad (3.33)$$

which is then unwrapped

$$\begin{aligned}
(\phi_{m,n} - \phi_{o,n})^u &= kx_n (u_m - u_o) - kx_n^2 \left(\frac{1}{2R_m} - \frac{1}{2R_o} \right) \\
&+ kx_n^2 \left(\frac{u_m^2}{2R_m} - \frac{u_o^2}{2R_o} \right) + \delta\phi_{m,n} - \delta\phi_{o,n}.
\end{aligned} \tag{3.34}$$

For many microwave imaging systems and target geometries the quantity $kx_n^2 \left(\frac{u_o^2}{2R_o} - \frac{u_m^2}{2R_m} \right) \ll \pi$, even in very near-field imaging situations. Further, $1/2R_o \approx 1/2R_m$; therefore, (3.34) is nearly linear in x (first term) and is perturbed by the distortions in the phasefronts caused by clutter in range bins R_o and R_m (last two terms). The average of M such quantities will also be a straight line with a smaller perturbation provided that the clutter in the various candidate beamformer range bins are uncorrelated. The unwrapping is illustrated in Figure 3.10a where the dots represent $\phi_{m,n} - \phi_{o,n}$ versus element position n . Each of the M curves $\phi_{m,n} - \phi_{o,n}$ versus n exhibits discontinuities at different values of n . Unwrapping removes these discontinuities and permits averaging the M curves to obtain a linear regression line with smaller perturbations. The symbols '*' at the left and right edges of Figure 3.10a represent the unwrapped values of the symbols '.'. The residual clutter-induced phase errors $\delta\phi_{m,n} - \delta\phi_{o,n}$ in (3.34) are depicted in Figure 3.10b.

The success of the procedure depends upon the quality of the phase unwrapping. It is clear that phase unwrapping will be a relatively easy task if the slope of $\phi_{m,n} - \phi_{o,n}$ is small, i.e., $k(u_o - u_m)\Delta x$ is very much less than 2π where Δx is the nominal interele

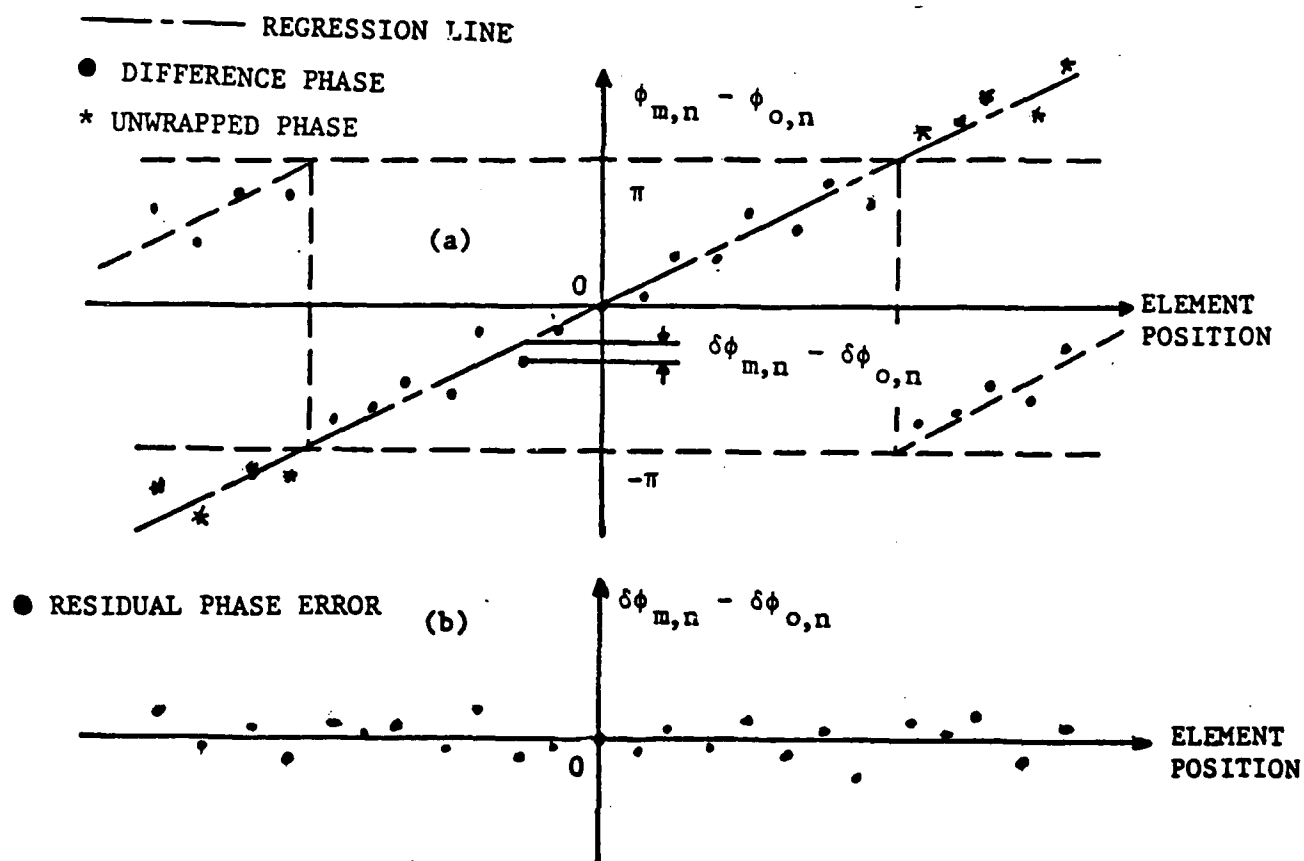


FIGURE 3.10 (a) PHASE UNWRAPPING
 (b) RESIDUAL PHASE ERRORS BETWEEN THE REGRESSION LINE
 AND THE UNWRAPPED PHASES
 (FROM [24].)

ment spacing. The residual phase errors are easily obtained by calculating the differential phases between the unwrapped phases and the linear regression line. The dots in Figure 3.10b represent $\delta\phi_{m,n} - \delta\phi_{o,n}$ versus n . The slope of a linear periodic array with $\lambda/2$ spacing is $\pi(u_m - u_o)$. $|u_m - u_o|$ cannot exceed the transmitter beamwidth, which is rarely more than a few degrees. Hence in most imaging scenarios there will be many data points between the discontinuities of $\phi_{m,n} - \phi_{o,n}$. However, for an array with large inter-element spacing the number of data points between 2π jumps can be small and the phase unwrapping problem becomes more difficult, in which case MSA may prove less applicable. The second requirement for successful unwrapping is that the perturbations in the straight line $kx_n(u_m - u_o)$ due to clutter may be much smaller than π . It is for this reason that the range bin with the smallest normalized amplitude variance (and therefore the smallest clutter-induced phase perturbation) is chosen to unwrap the phases of the candidate beamformers.

The unwrapped value of $\phi_{m,n} - \phi_{o,n}$, denoted $(\phi_{m,n} - \phi_{o,n})^u$, is given in (3.34). The average of M unwrapped phase sequence curves is

$$\begin{aligned} \mu_n = \frac{1}{M} \sum_{m=1}^M (\phi_{m,n} - \phi_{o,n})^u &= kx_n \left[\left(\frac{1}{M} \sum u_m \right) - u_o \right] \\ &- \frac{kx_n^2}{2} \left[\left(\frac{1}{M} \sum \frac{1-u_m^2}{R_m} \right) - \frac{1-u_o^2}{R_o} \right] \\ &+ \frac{1}{M} \sum \delta\phi_{m,n} - \delta\phi_{o,n} \end{aligned} \quad (3.35)$$

The second, fourth and sixth terms sum to $\beta_n - \phi_{o,n}$ (see (3.31)). Adding (3.31) to (3.35) replaces these terms by β_n , which reduces the bias and random errors. This sum is called ϕ_n^* :

$$\begin{aligned}\phi_n^* &= \mu_n + \phi_{o,n} \\ &= \frac{kx_n}{M} \sum_{m=1}^M u_m - \frac{kx_n^2}{M} \sum_{m=1}^M \frac{1-u_m^2}{2R_m} + \beta_n + \frac{1}{M} \sum_{m=1}^M \delta\phi_{m,n}. \quad (3.36)\end{aligned}$$

The negative of (3.36) is the MSA error-compensating phase shift introduced into the nth channel. Therefore, the nth component of the MSA weight vector is

$$w_{n,MSA} = \exp(-j\phi_n^*) \quad (3.37)$$

The first two terms in (3.36) point and focus the array to map coordinates (u, R) :

$$\left\{ \frac{1}{M} \sum_{m=1}^M u_m, \frac{1}{M} \sum_{m=1}^M \frac{1}{R_m} \right\}^{-1}.$$

The third term is the phase error caused by electrical phase distortion and element position error. The fourth term is the averaged clutter-induced phase error of the M candidate beamformers. This term is smaller than the corresponding DSA term ($\delta\phi_{o,n}$ in (3.31)) because of the averaging.

3.6 COMPARISON OF DSA AND MSA

In this section, the angular biases and errors in the DSA and MSA are compared. Equations (3.31 and (3.36) define the error-compensating phase shifters. The first term in (3.31) is $kx_n u_o$ and in (3.36) it is $(kx_n \sum_{m=1}^M u_m)/M$. These terms steer the beams. The DSA centers the phase-corrected image on u_o whereas the MSA centers the

phase-corrected image on $(\sum_m^M u_m)/M$, which is the average of the locations of the M candidate beamformers. The average is more likely to be closer to the center of the FOV than the location of the reference beamformer u_0 . Therefore, one advantage of the MSA over the DSA is that it focuses the array closer to the center of the FOV than the DSA, thereby reducing the uncertainty in target location.

An estimate of the improvement in angular accuracy is obtained using the theorem in statistics that the standard deviation of the sample mean of M independent random variables varies as $M^{-1/2}$, and the realistic assumption that the angular locations of the candidate beamformers are random and independent. The expected location of u_0 is within the main lobe (of width $\Delta\theta$) of the transmitting beam for otherwise the target would be too weakly illuminated to become the reference reflector. For the same reason the directions to all the other candidate beamformers also fall within the main beam. These bearings to the targets may be assumed to be approximately uniformly distributed within the main beam because there is no physical reason for their distribution to be biased. Thus, after averaging, the standard deviation of the sample-mean pointing direction is $\sigma_\theta/M^{1/2}$. Hence the accuracy in the angular coordinate of the microwave image is improved by the factor $M^{1/2}$.

The second terms in (3.31) and (3.36) focus the array to R_0 and $(\frac{1}{M} \sum R_m^{-1})^{-1}$, respectively. There is no advantage of one over the other because the quadratic phase curvature from either distance is deterministic and therefore can be removed to permit re-

focusing the array for range bins lying outside the depth of field of the array.

The third terms in (3.31) and (3.36) are the phase errors caused by electrical phase distortion and element position error. This error is constant for all range bins and is corrected by both ABF procedures.

The fourth terms in (3.31) and (3.36) are the clutter-induced phase errors. The MSA term is smaller because of the M-fold averaging. Let σ_{DSA} be the standard deviation of $\delta\phi_{o,n}$ of (3.31) and σ_{MSA} be the standard deviation of $\frac{1}{M} \sum_{m=1}^M \delta\phi_{m,n}$ of (3.36). Given the realistic assumption that all phase errors are independent, and under the assumption that the $\delta\phi_{m,n}$ and $\delta\phi_{o,n}$ have common variances, the relation between the phase-error variances is

$$\sigma_{\text{MSA}}^2 = \frac{1}{M} \sigma_{\text{DSA}}^2 \quad (3.38)$$

The significance of (3.38) lies in its influence upon the radiation pattern. σ_{MSA}^2 and σ_{DSA}^2 are the variances of the phase errors in the phase corrections across the array after ABF. It is these residual errors that determine the qualities of the radiation patterns formed by these algorithms. It has been shown that the expected power pattern Eff^* when phase errors are present and amplitude errors are not, normalized so that the on-axis ($u=0$) gain in the absence of phase errors is unity, is [after (13.7) of [9]]

$$\text{Eff}^* = e^{-\sigma^2} f_o f_o^* + \frac{\overline{a^2}}{\bar{a}^2} \frac{\sigma^2}{N} \quad (3.39)$$

For the problem being discussed σ^2 is either σ_{DSA}^2 or σ_{MSA}^2 .

$f = f(u)$ is the radiation pattern of the array with phase error,
 $f_0 = f_0(u)$ is the design pattern, $\frac{\overline{a^2}}{\bar{a}^2}$ is the square of the ratio of

the rms to mean value of the aperture weights and is normally close to and slightly greater than unity, and N is the number of elements. Clearly $\sigma^2 > 0$ reduces main lobe gain and increases sidelobes. Only when σ_{DSA} is not sufficiently small is there reason to reduce the residual phase-error variance with the more complicated algorithm. For example, assume that $\sigma_{\text{DSA}}^2 = 0.1(\text{rad})^2$,

$N = 300$, the allowed loss in main lobe gain is 0.5 dB and the sidelobe specification, after ABF, is -30 dB. The expected main lobe gain, relative to the design gain, is $e^{-0.1} \approx 0.9$ or -0.43 dB, which is acceptable. However, the sidelobe level is too high. The average sidelobe is approximately $0.1/300$ or about -35 dB and the peak sidelobe is typically 10 dB higher, which exceeds the specification by 5 dB. Equation (3.38) indicates that MSA will meet the specifications for a value of $M = 3$.

However, (3.38) is somewhat optimistic because the second assumption, equality of variances, is not often satisfied. The "best" range bin is selected for the DSA, implying that the rms of the phase perturbations $\delta\phi_{m,n}$ of the MSA exceeds that of the $\delta\phi_{0,n}$ of the DSA. Let $\alpha \geq 1$ be the average of the variances in the M candidate beamforming bins relative to the DSA reference ABF bin. Then the proper relation between the phase-error variances of the two algorithms becomes

$$\sigma_{\text{MSA}}^2 = \frac{\alpha}{M} \sigma_{\text{DSA}}^2 \quad (3.40)$$

Because MSA is a more complicated algorithm, achievement of the improvement given by (3.40) requires additional computation. Experience with the algorithm indicates that the computation is 2-3 times larger than the DSA process.

MSA plays the role of a threshold extender to DSA. The lowest amplitude variance bin is selected for the DSA reference. Only if it proves inadequate is the more complicated MSA employed. The reference bin data are used to unwrap the phases of a small set of the M candidate beamformers. A few dB reduction in the phase-error variance has been observed in ground clutter experiments. This advantage is demonstrated in the next section.

The DSA and MSA can also be compared by correlating the DSA and MSA phase-corrected images with a perfect image. The correlation measure has proved useful in comparing microwave images [12]. The correlation between two images $I_1(u)$ and $I_2(u)$ is

$$\rho \triangleq \frac{\int_{-1}^1 I_1(u) I_2(u) du}{\left[\int_{-1}^1 I_1^2(u) du \int_{-1}^1 I_2^2(u) du \right]^{1/2}} \quad (3.41)$$

where $I_1(u)$ is the error-free image of the target scene and $I_2(u)$ is the erroneous image. Assume that the perturbations in the phase corrections caused by clutter are independent and identically distributed Gaussian random variables with zero mean and variance σ^2 . A lower bound on the correlation ρ between the error-free and erro-

neous images has been derived in [16] in terms of the residual phase-error variance; it is given by

$$\rho_0 = \frac{1}{2} (1 + e^{-\sigma^2}) \approx e^{-\sigma^2/2} \quad (3.42)$$

so that $\rho \geq \rho_0$. By comparing (3.42) and (3.39) we see that the expected value of the mainbeam gain relative to the design gain G_0 is the square of ρ_0 :

$$E \left[\frac{G}{G_0} \right] = \exp(-\sigma_{\delta\phi}^2) = \rho_0^2 \quad (3.43)$$

3.7 DSA AND MSA EXPERIMENTS

The 83-m, 330-element quasi-linear array pictured in Figure 3.4 was used to image the nuclear power plant in Limerick, PA, located 17.6 km from the array. The array was highly distorted; the locations of the receivers differed from their assumed locations by one or more wavelengths in each dimension.

Beamforming bins having normalized amplitude variances not larger than 0.12 have been shown to yield satisfactory images when the DSA is used for phase cohering an array [11]. A survey of the normalized amplitude variances of the 75 range bins in the FOV yielded 6 bins that could possibly contain a single subdominant reflector embedded in clutter. These range bins were ordered in accordance with their variances and numbered 0 through 5; their normalized amplitude variances were 0.06, 0.07, 0.09, 0.10, 0.10 and 0.12. Bin 0 contains the highest quality beamformer. A comparison was made between the DSA and the MSA both using bin 0 as the reference bin. Bins 1 and 2, the next highest quality bins, were used as the candidate bins for the MSA test. These results, shown

in parts a and b of Figures 3.11-3.13, compare the DSA and the MSA under low variance conditions, i.e., highly favorable for imaging.

A second comparison was made using high variance range bins, none of which was favorable for imaging. These range bins had normalized amplitude variances of 0.20, 0.21 and 0.23 and were numbered 6 through 8. The results of these experiments are shown in parts c and d of Figures 3.11-3.13.

3.7.1 1-D CROSS-RANGE IMAGES OF BIN 2

Figure 3.11 shows the cross-range images of bin 2 obtained from the four experiments. The dotted line, which is 25 dB below the peak, is a typical threshold value below which signals are not displayed in range-azimuth imagery. It is close to the average sidelobe level of $10 \log \frac{1}{N}$, where N is the number of antenna array elements. The upper two parts compare the low variance experiments and the lower two parts compare the high variance experiments.

Figure 3.11a shows that the DSA peak sidelobe level (PSL) is about -13 dB. Figure 3.11b shows the improvement due to the MSA: the PSL is decreased to about -16 dB. Furthermore, the sidelobe artifacts around the main beam, evident in the DSA image, have been removed.

The high variance comparison is made in the lower two figures. Figure 3.11c shows the performance of the DSA with bin 8 as the reference bin. The PSL has risen to about -7 dB and many sidelobes rise above the threshold. This experiment demonstrates that bin 8, whose normalized amplitude variance is 0.23, is a very poor beamformer for the DSA. However, when additional candidate beam-

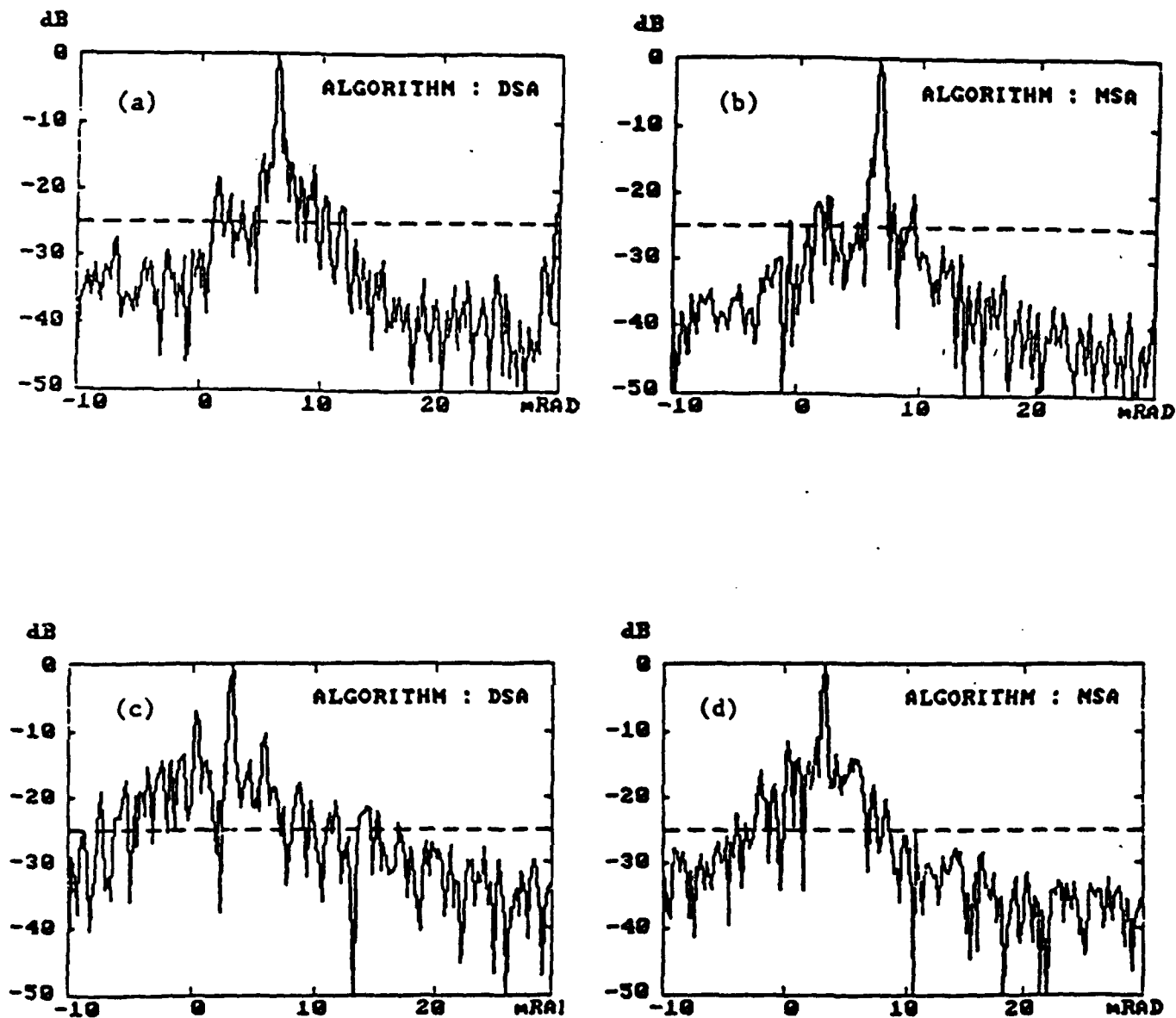


FIGURE 3.11 CROSS-RANGE IMAGE OF BIN 2 OF LIMERICK NUCLEAR POWER PLANT
LOW VARIANCE CASE

(a) DSA WITH BIN 0 AS THE REFERENCE BIN

(b) MSA WITH BIN 0 AS THE REFERENCE BIN AND BINS 1-2 AS THE CANDIDATE BINS

HIGH VARIANCE CASE

(c) DSA WITH BIN 8 AS THE REFERENCE BIN

(d) MSA WITH BIN 8 AS THE REFERENCE BIN AND BINS 6-7 AS THE CANDIDATE BINS

(FROM [24].)

former bins of equally poor quality are added, the MSA performs reasonably satisfactorily. Figure 3.11d shows this case. The PSL has decreased to about -11 dB. This MSA image is almost as good as the DSA image of Figure 3.11a formed from the highest quality beamformer.*

In addition to a comparison based upon the PSL, a second useful comparison is the number of apparent targets appearing above the display threshold. Both values are listed in Table 3.4 for the four cases, along with the normalized amplitude variance information. From the table it is evident that the MSA high variance case approaches the quality of the low variance DSA case.

Figure 3.12 shows the details of the residual phase errors across the aperture for the four cases. The rms errors and the losses in mainbeam gain (calculated from (3.43)) are listed in Table 3.5.

3.7.2 2-D RANGE-AZIMUTH IMAGES

Figure 3.13 shows range-azimuth images of buildings at the site of the Limerick nuclear power plant. The upper two images, both obtained from low variance beamformers, are very similar and both are satisfactory. Although the MSA reduces the phase errors and thereby intrinsically produces a higher quality image, the DSA image of Figure 3.13a is of sufficient quality so that use of the MSA is not warranted.

*It is interesting to observe the shift in the optical axes of the lower images relative to the upper ones. The radio camera points in the direction of the reference reflector. The shift reflects the difference in directions of the reference reflectors in bins 0 and 8.

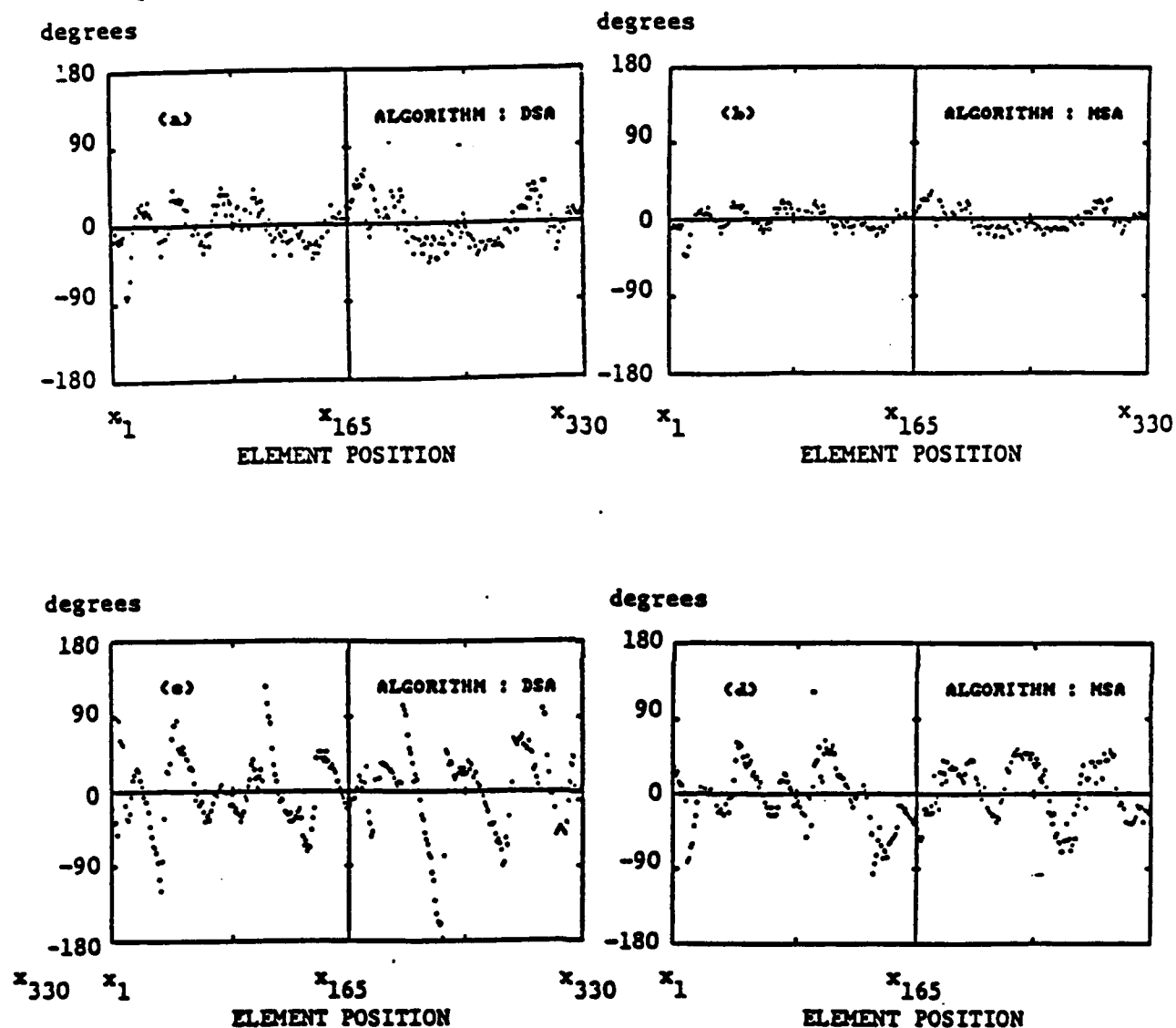


FIGURE 3.12. PHASE ERRORS OF BIN 2 OF LIMERICK NUCLEAR PCWER PLANT
 LOW VARIANCE CASE
 (a) DSA WITH BIN 0 AS THE REFERENCE BIN
 (b) MSA WITH BIN 0 AS THE REFERENCE BIN AND BINS 1-2 AS THE CANDIDATE BINS
 HIGH VARIANCE CASE
 (c) DSA WITH BIN 8 AS THE REFERENCE BIN
 (d) MSA WITH BIN 8 AS THE REFERENCE BIN AND BINS 6-7 AS THE CANDIDATE BINS
 (FROM [24].)

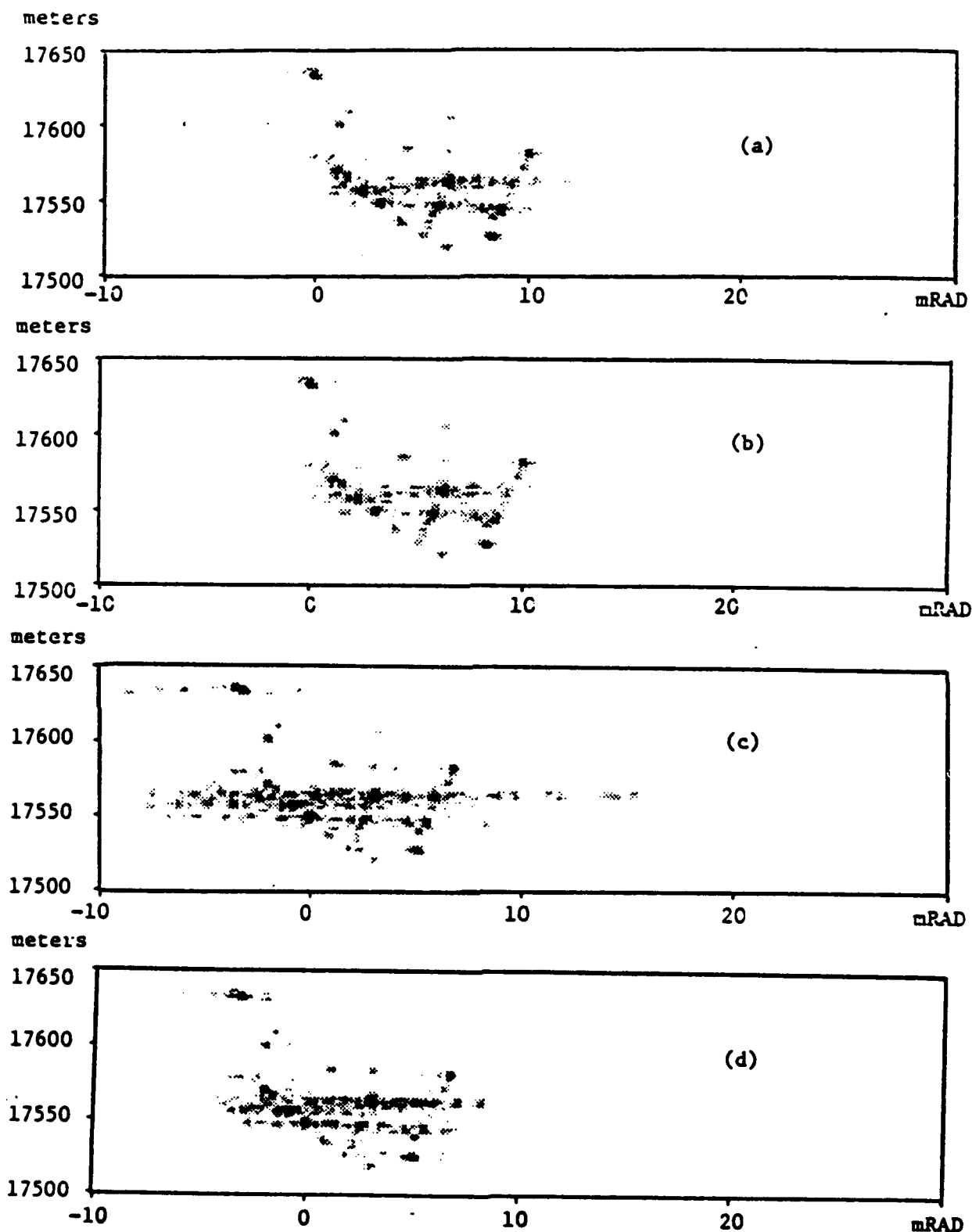


FIGURE 3.13 RANGE-AZIMUTH IMAGES AT SITE OF LIMERICK NUCLEAR POWER PLANT.

LOW VARIANCE CASE

(a) DSA WITH BIN 0 AS THE REFERENCE BIN

(b) MSA WITH BIN 0 AS THE REFERENCE BIN AND BINS 1-2 AS THE CANDIDATE BINS

HIGH VARIANCE CASE

(c) DSA WITH BIN 8 AS THE REFERENCE BIN

(d) MSA WITH BIN 8 AS THE REFERENCE BIN AND BINS 6-7 AS THE CANDIDATE BINS

(FROM [24].)

	<u>LOW VARIANCE</u>		<u>HIGH VARIANCE</u>	
SELF-CALIBRATION ALGORITHM	DSA	MSA	DSA	MSA
EXPERIMENT IN FIGURE 3.11	a	b	d	d
AMPLITUDE VARIANCE				
REFERENCE BEAMFORMER	0.06	0.06	0.23	0.23
CANDIDATE BEAMFORMERS		0.07		0.20
		0.09		0.21
PEAK SIDE LOBE (dB)	-13	-16	-7	-11
NUMBER OF TARGETS > -25 dB	15	10	26	15

TABLE 3.4 COMPARISON OF DSA AND MSA SELF-CALIBRATING ALGORITHMS IN LOW AND HIGH VARIANCE CASES. THE MSA HIGH VARIANCE CASE IS ALMOST AS GOOD AS THE DSA LOW VARIANCE CASE.

	<u>LOW VARIANCE</u>		<u>HIGH VARIANCE</u>	
SELF-CALIBRATION ALGORITHM	DSA	MSA	DSA	MSA
EXPERIMENT IN FIGURE 3.12	a	b	c	d
RESIDUAL RMS PHASE ERROR (deg)	23.57	10.07	46.74	33.35
ΔG (dB)	-0.73	-0.13	-2.89	-1.47

TABLE 3.5. RESIDUAL RMS PHASE ERRORS FOR THE FOUR CASES OF FIGURE 3.11 AND THE LOSSES IN MAIN BEAM GAIN THAT RESULT FROM THESE ERRORS.

Not so with the imagery from the low quality beamformers. Figure 3.13c shows the DSA image driven by a range bin with a normalized amplitude variance of 0.23. This image is badly degraded by high sidelobes; it is not a satisfactory image. The same low quality reference beamformer plus two equally low quality candidate bins produce a considerably improved MSA image (Figure 3.13d). Here the sidelobe artifacts have been largely removed and the image is not significantly inferior to the high quality images in Figures 3.13a and 3.13b.

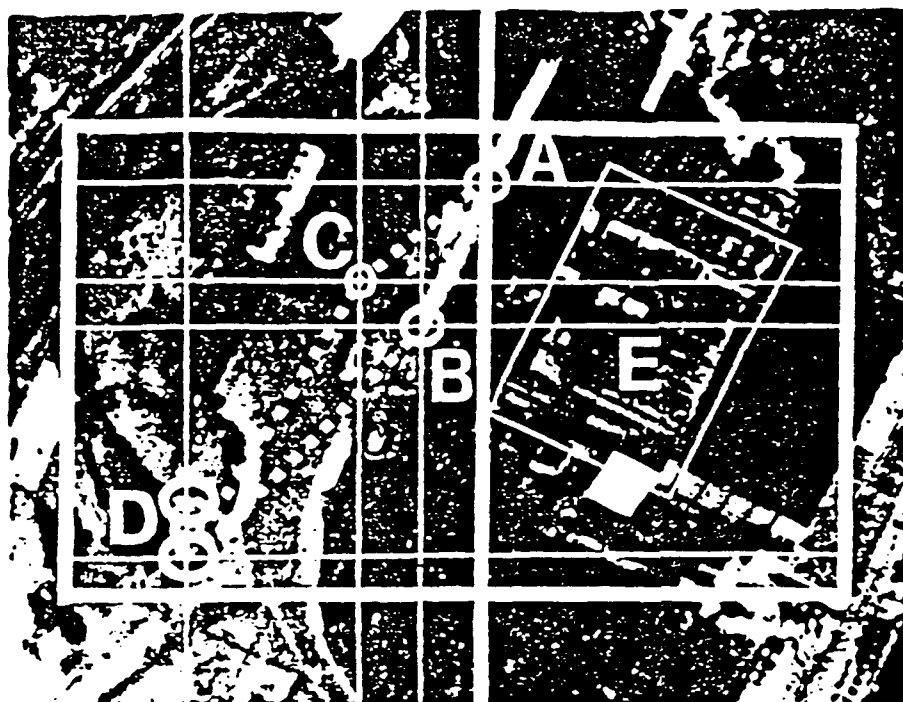
3.7.3 IMAGE CORRELATION

It is interesting to form an image correlation comparison based on the definition given in (3.41). The best of the four images is Figure 3.13b, as determined by the residual RMS phase data. Using it as the reference image, its correlations with Figures 3.13a, c and d are 0.98, 0.87 and 0.92, respectively. In [12] it was shown that a correlation coefficient of 0.9 or greater indicates satisfactory image formation. Based on that criterion, experiment c fails while a and d are satisfactory. Thus we again see that three range bins having normalized amplitude variances 0.20 or greater can be used with the MSA to obtain a useful image, one nearly as good as the image obtained using the DSA with the best beamformer. Moreover, if only one of the three range bins is used for beamforming purposes, the resulting image will have large sidelobe artifacts, as is demonstrated in Figures 3.11c and 3.13c. In addition, the loss in mainlobe gain relative to experiment b can be calculated using (3.43). Table 3.6 summarizes these findings.

	<u>LOW VARIANCE</u>		<u>HIGH VARIANCE</u>	
SELF-CALIBRATION ALGORITHM	DSA	MSA	DSA	MSA
EXPERIMENT IN FIGURE 3.13	a	b (REFERENCE)	c	d
IMAGE CORRELATION	0.98	1.0	0.87	0.92
ΔG (dB)	-0.18	0	-1.21	-0.72

TABLE 3.6 IMAGE CORRELATIONS AND LOSSES OF MAIN BEAM GAIN RELATIVE TO EXPERIMENT b AGAIN DEMONSTRATING THAT THE MSA HIGH VARIANCE CASE (FIGURE 3.13d) IS NEARLY AS GOOD AS THE DSA LOW VARIANCE CASE (FIGURE 3.13a).

The last experiment illustrates the capability of a dominant scatterer algorithm to image a distant target with human-optical resolution. The VFRC 83-m array was used to image an industrial site in Phoenixville, PA, located at a distance of 8.2 km from the array. Figure 3.14a is an aerial photo of the Cromby Power Plant which shows two high stacks, a water tower, the power plant building, and two connected storage silos. The microwave image of the white blocked area in the upper figure is shown below. The radar line of sight is indicated by the white vertical line in the center of the upper figure. The radio camera image was obtained by applying the MSA to the best set of three range bins; it reveals the two high stacks (A and B), the water tower (C), the two connected silos (D), and the power plant building (E). The resolution cell is 3 m in both range and cross range. The MSA phase corrections compensated for the large geometric distortion of the phased



(a)

A,B: TWO HIGH STACKS

C: WATER TOWER

D: TWO STORAGE SILOS

(ERECTED AFTER PHOTO)

E: POWER PLANT BUILDING

RANGE (METERS)

8260

8240

8220

8200

8180

8160

8140

(b)

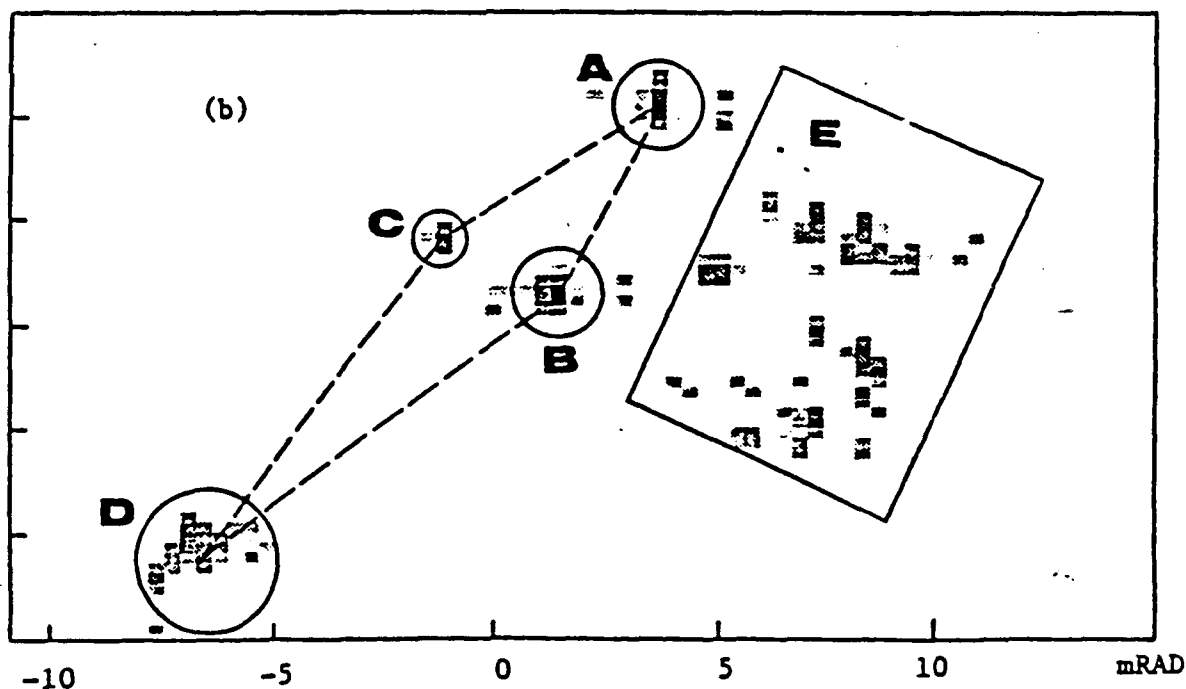


FIGURE 3.14 OPTICAL PHOTO AND RADIO CAMERA IMAGE OF CROMBY POWER PLANT.

(a) AERIAL PHOTO, PHOENIXVILLE, PA (1975)

(b) RADIO CAMERA IMAGE (3 CM WAVELENGTH)

(FROM [24].)

array antenna, and very little sidelobe energy is evident in the microwave image.

The variance range from 0.12 to 0.20 is the DSA transition zone. The algorithm always works at the low end and never works at the high end. The MSA, on the other hand, provides a useful image from three range bins having normalized amplitude variances as large as the order of 0.2. In this sense MSA acts like a threshold extender, permitting the radio camera to function under adverse clutter conditions.

The performance of each algorithm can be improved by subarray processing.

3.8 USE OF SUBARRAYS

Other variations of the basic algorithm improve its operation. One modification is the division of the large array into sections or subarrays to enhance the adaptive beamforming process when the beamforming source is not an ideal point reflector. Figure 3.15 shows the problem. A target of size T reradiates energy toward the array. The radiation is always lobular and the nominal lobe width is λ/T almost independent of the distribution of the scatterers on the target. The phase across the central portion of a lobe is fairly constant, while it changes abruptly and often randomly from lobe to lobe. For the ABF process to proceed smoothly it is necessary for the entire array to be illuminated by the central portion of a single lobe. A typical lobe cross section at the array, which is a distance R from the target, is $\lambda R/T$. Unless L , the array size, is smaller than $\lambda R/T$, this condition is

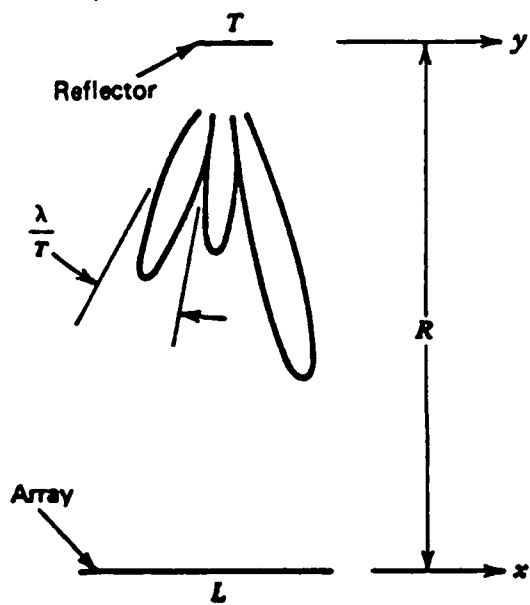


FIGURE 3.15 The reradiation pattern of the target is lobular. (From [4].)

not likely to be satisfied. It is shown in [4] and [8] that the minimum target size for satisfactory beamforming is

$$T < \frac{\lambda R}{2L} \quad (3.44)$$

Experience with manmade reflectors indicates that the condition (3.44) is violated sometimes and imaging quality with the DSA or the MSA degrades. It is often possible to correct this situation by breaking the array into sections or subarrays each small enough to satisfy (3.44). Let $L_1 < L$ be such a subarray such that

$$T < \frac{\lambda R}{2L_1} \quad (3.45)$$

The phase of the reradiated wavefront from the target across the subarray is nearly constant and phase corrections for element position errors, electrical mistunings, etc., can be accomplished. Let L_2, L_3 , etc., be other such subarrays. Phase compensation is performed across each subarray. Thus each subarray has its aberrations corrected. However, the phase reference for a particular subarray is the phase of the lobe of the reradiation pattern of the target that illuminates that subarray. Because the lobe phases must be assumed to be random with respect to each other, the array segments, each internally phase synchronized, are also randomly phased with respect to each other. Thus the remaining problem is to link the array segments by phase correcting for the random phase differences between segments of the array. Figure 3.16 illustrates this situation. The abscissa is range and the ordinate

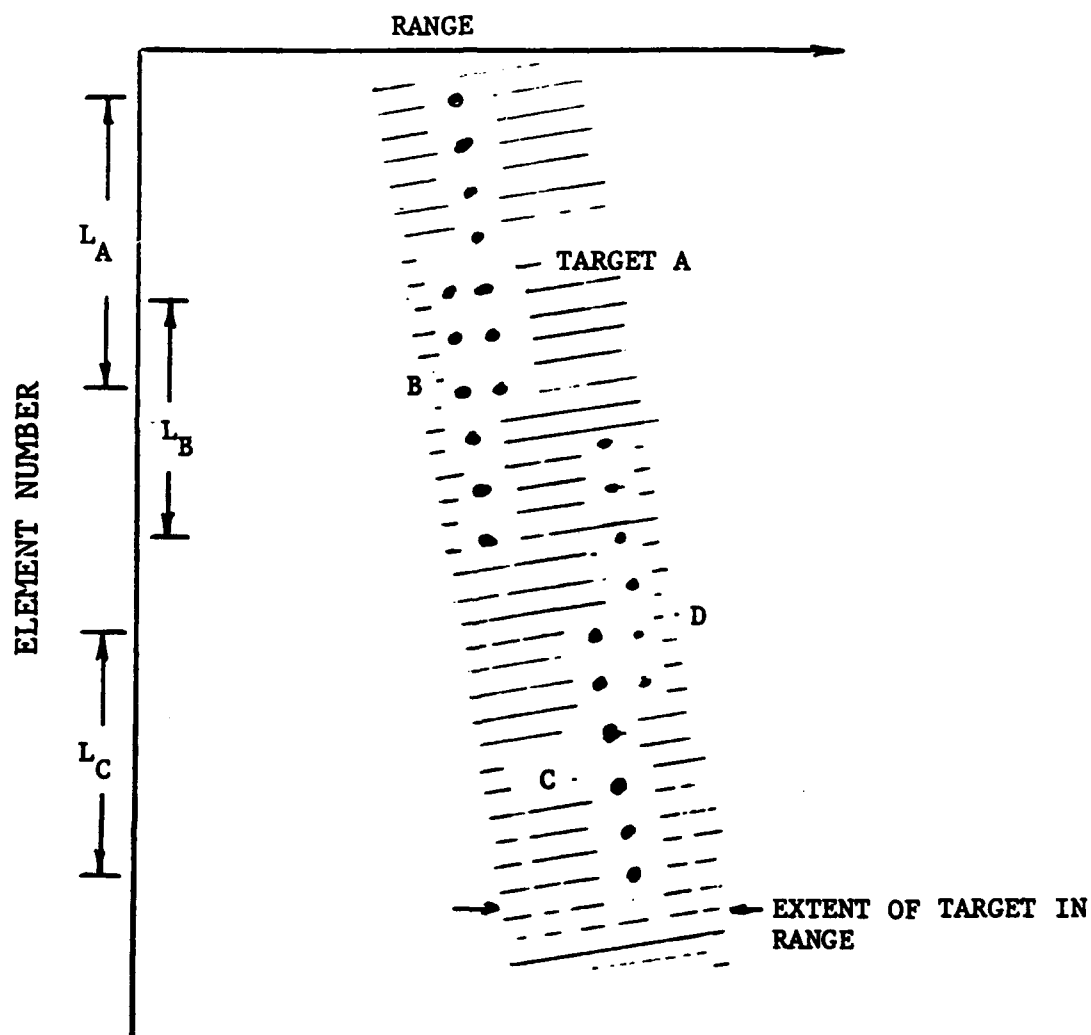


FIGURE 3.16 SUBARRAYS L_A , L_B AND L_C SELF-COHERE ON TARGETS A, B AND C. L_A AND L_B ARE OVERLAPPING SUBARRAYS; L_B AND L_C ARE NONOVERLAPPING.

is element number. Target echoes fall in the shaded area. Let A, B and C be prominent scatterers. None persists throughout the array, however. A provides a strong, stable echo over that portion of the array labeled L_A , and similarly for B and C. Subarrays L_A and L_B overlap; L_B and L_C do not.

Array elements within L_A are self-calibrated by the echoes from A using, say, the DSA. Echoes from B self-calibrate subarray L_B . The self-calibrated subarrays do not share a common phase reference and therefore exhibit a random offset phase between them. The offset between L_A and L_B can easily be measured because targets A and B appear in both data sets. Let ϕ_{AA} be the phase of target A as observed by subarray L_A and ϕ_{AB} its phase as observed by subarray L_B . The difference $\phi_{AA} - \phi_{AB}$ is the phase offset between the self-calibrated subarrays. Adding this difference to all the phases in the L_B data set eliminates the random phase offset and extends the calibration over the two subarrays.

An additional step is required when the subarrays do not overlap. In that case a target common to both subarrays is found after self-calibration. Call this target D. The phase difference $\phi_{DB} - \phi_{DC}$ is added to all the phases in the L_C data set to eliminate the random phase offset between subarrays B and C.

The technique is more complex when applied to the MSA. Two useful procedures for solving the problem are now discussed. The first deals with non-overlapping subarrays, the second with overlapping array segments. Both techniques are described in the context of the MSA.

The phase sequence $\phi_{o,n}$ from the reference range bin R_o , given in (3.31), is

$$\phi_{o,n} = kx_n u_o - \frac{kx_n^2 (1-u_o^2)}{2R_o} + \delta\phi_{o,n} + \beta_n \quad (3.46)$$

where $\delta\phi_{o,n}$ are the perturbations in the phasefront caused by clutter and β_n are the phase errors due to errors in array geometry and mistunings in the receivers. The averaged unwrapped phase differences of the sequences $\phi_{m,n}$ from M candidate beamformers, given in (3.35), are

$$\begin{aligned} \mu_n &= \frac{1}{M} \sum_{m=1}^M (\phi_{m,n} - \phi_{o,n})^u \\ &= kx_n \left(\frac{1}{M} \sum u_m - u_o \right) - \frac{kx_n^2}{2} \left(\frac{1}{M} \sum \frac{1-u_n^2}{R_m} - \frac{1-u_o^2}{R_o} \right) \\ &\quad + \left(\frac{1}{M} \sum \delta\phi_{m,n} \right) - \delta\phi_{o,n} \end{aligned} \quad (3.47)$$

The n th component of the weight vector formed by the MSA is (from (3.37))

$$w_{n,MSA} = \exp[-j(\mu_n + \delta\phi_{o,n})] \quad (3.48)$$

Eq. (3.47) is nearly a straight line (because the quadratic term is very small) perturbed by zero-mean clutter-induced phase errors. Such a sequence is illustrated in Figure 3.10a. This figure portrays the case in which the main reflector is physically small, i.e., satisfies condition (3.44), and overwhelmingly dominates the backscatter from the clutter. In this case the data points cluster about a linear regression line.

Sometimes, however, condition (3.44) is not satisfied. Then, due to the lobular nature of the reradiation, the data sequence exhibits the phenomenon shown in Figure 3.16. The low spatial frequency variation shown there induces a phase error that adds to

an independent, random perturbation from element to element. This phenomenon is evident in the residual phase errors shown in Figure 3.17 and indicates a lobular reradiation across the array. The residual phase-error variance is increased because it is the sum of the variances of the random component and the low frequency undulation. It is often possible to remove much of the latter contribution by estimating, from the data, the phase change from lobe to lobe. These phase jumps are then deleted from the data.

Figure 3.17 illustrates one procedure. A μ_n sequence is illustrated in the upper figure. The array is broken into three subarrays and a linear regression line (least mean square fit to the data) is found for each subarray (a). The result is a lower residual phase error variance (b). The discontinuities in the piecewise linear fit of (a) to the data are assumed to be due to phase changes between lobes in the reradiation field; they are removed by adding fixed phases to each section to make the piecewise linear fit continuous (c). The modified sequence of averaged unwrapped differential phases is called μ_n^* and the nth component of the modified MSA weight becomes

$$w_{n,MSA}^* = \exp \sum [-j(\mu_n^* + \phi_{0,n})] \quad (3.49)$$

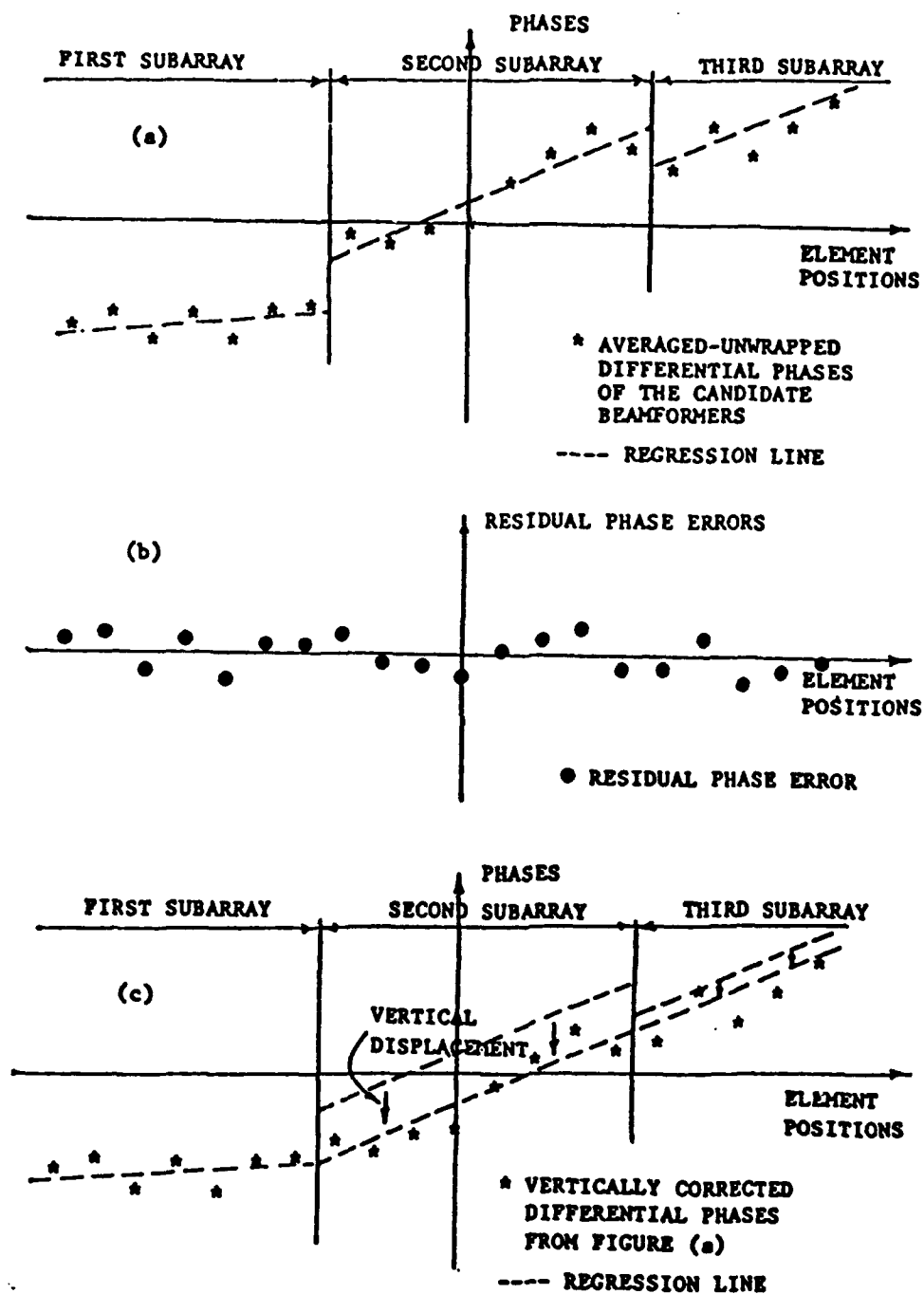


FIGURE 3.17 NONOVERLAPPING SUBARRAY PROCESSING.

- (a) REGRESSION LINE IN EACH SUBARRAY.
- (b) RESIDUAL PHASE ERRORS AFTER REMOVING THE REGRESSION LINE FROM THE DIFFERENTIAL PHASES.
- (c) VERTICALLY CORRECTED DIFFERENTIAL PHASES FROM (a). (FROM [24] AND APPENDIX.)

Figure 3.18 illustrates another subarray procedure for estimating the correction phases. The arrays are overlapped in this case. Exactly as described before, regression lines are fit to the subarray μ_n data (a). Each overlap region now has two regression lines. Each pair is averaged to form a new regression line in its limited interval. The result is a discontinuous piecewise linear fit to the data, which are then adjusted exactly as described before to obtain a continuous piecewise linear fit (b). The phase-corrected data are the μ_n^* and the modified MSA weight vector is given by (3.49).

3.9 SUBARRAY EXPERIMENTS

Figure 3.19 shows four 1-D images of a corner reflector for which beamforming was accomplished with a relatively unsatisfactory scatterer, identified in the figure as the echo from bin 61. The target area was a residential street in Phoenixville, Pennsylvania. The amplitude variance from that range bin was 0.21. Figure 3.19a shows the DSA performance. The maximum amplitude reached is 53.26 units and the peak sidelobe is -6.9 dB. The image extends over nearly 30 mrad at the -25 dB level and does not look as expected from a corner reflector.

Figures 3.19b, c and d show the performances of MSA, MSA with non-overlapping subarrays and MSA with overlapping subarrays, respectively. The superiority of Figure 3.19d is evident. The peak amplitude has increased to 69.45 units, indicating an increase of 2.3 dB in main lobe gain, and the peak sidelobe has dropped to -

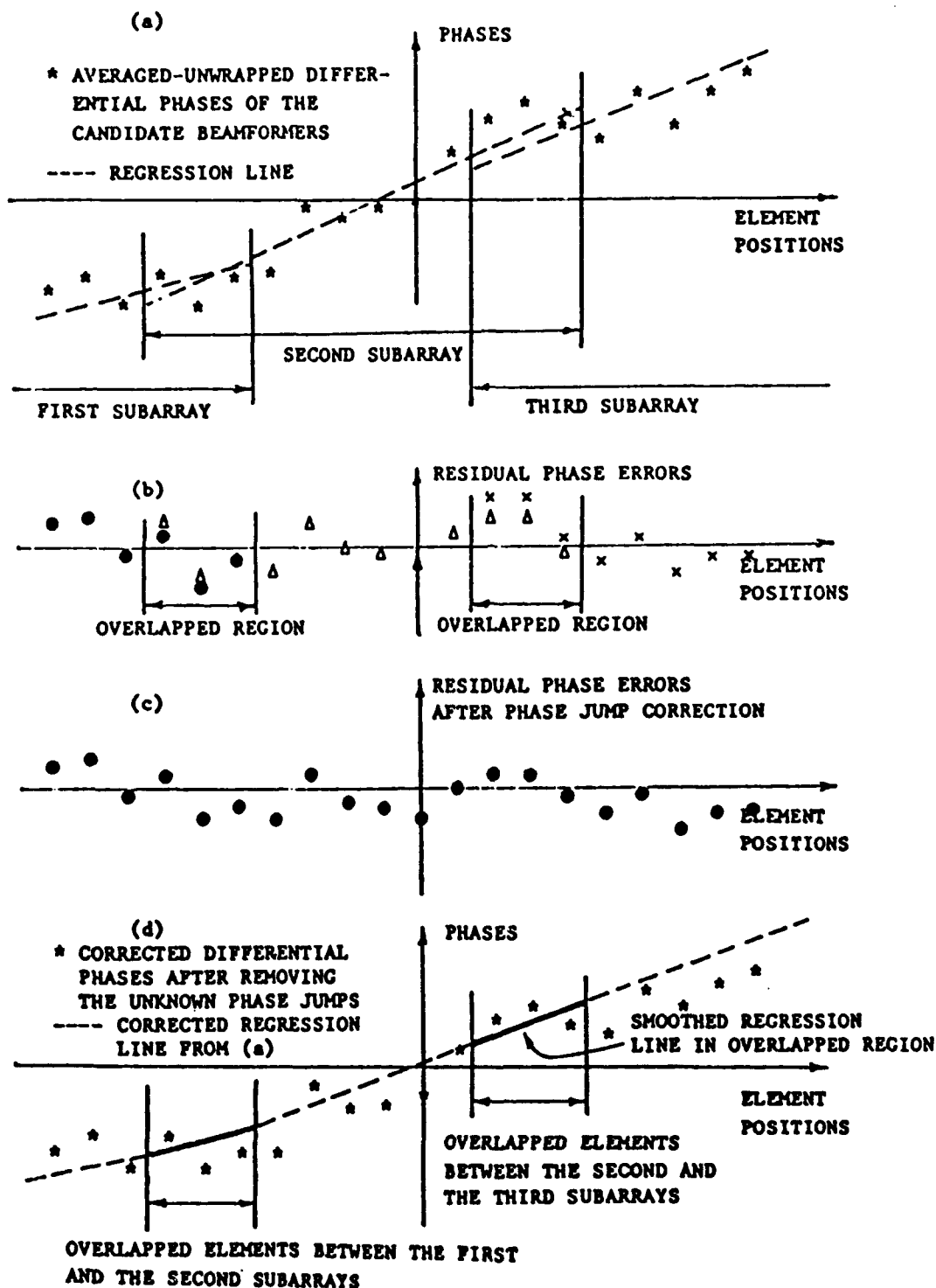


FIGURE 3.18 OVERLAPPING SUBARRAY PROCESSING.

- (a) REGRESSION LINE IN EACH SUBARRAY.
 - (b) RESIDUAL PHASE ERRORS AFTER REMOVING THE REGRESSION LINE FROM THE DIFFERENTIAL PHASES.
 - (c) CORRECTED RESIDUAL PHASE ERRORS.
 - (d) CORRECTED REGRESSION LINE AND CORRECTED PHASES.
- (FROM [24] AND APPENDIX.)

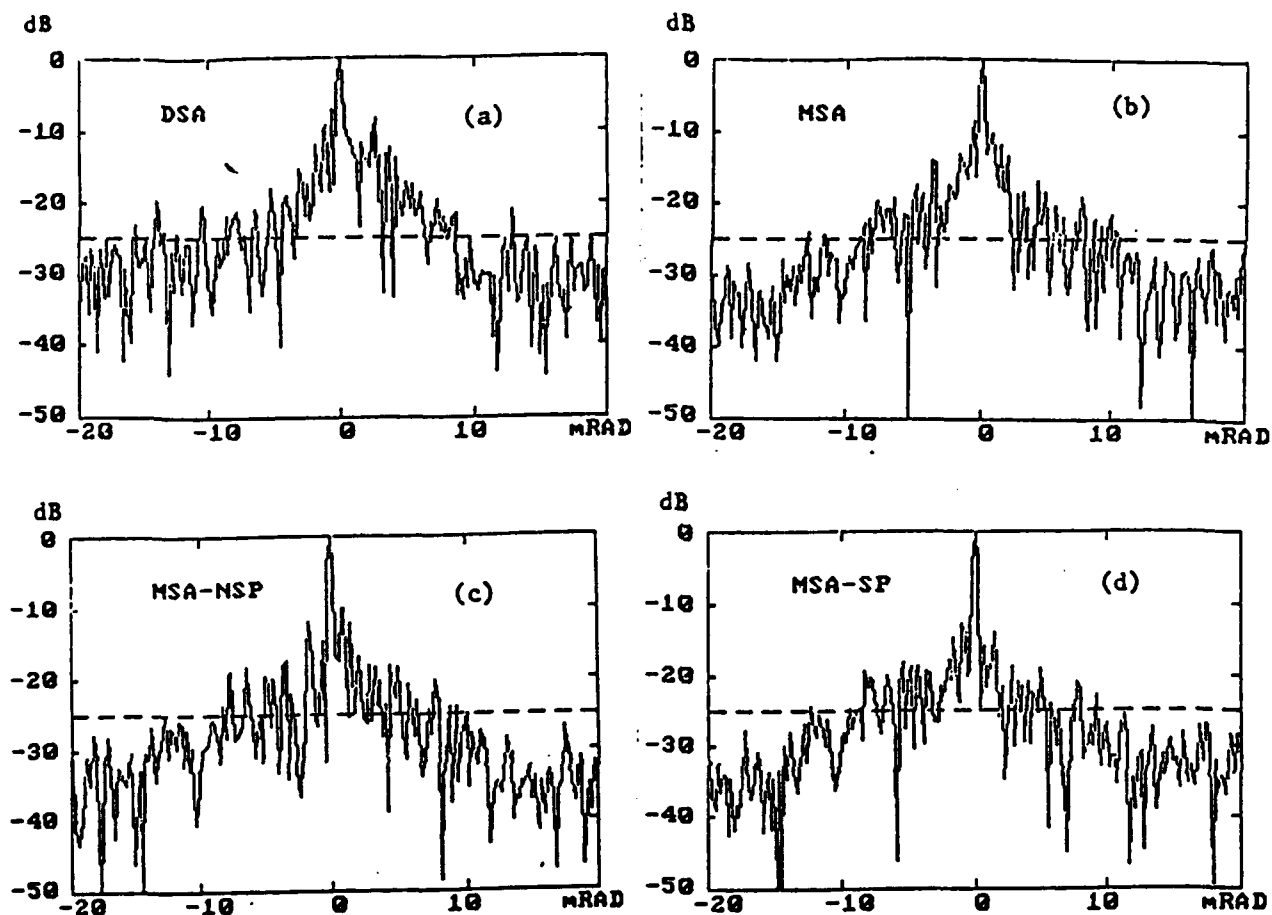


FIGURE 3.19 CROSS-RANGE IMAGES OF CORNER REFLECTOR. (FROM [24] AND APPENDIX.)

- (a) DSA WITH BIN 61
- (b) MSA WITH BINS 61, 67 AND 68
- (c) MSA WITH NONOVERLAPPING SUBARRAYS, USING BINS 61, 67, 68 AND THREE SUBARRAYS
- (d) MSA WITH OVERLAPPING SUBARRAYS, USING BINS 61, 67, 68 AND THREE SUBARRAYS

14.4 dB. The extent of the image above the -25 dB level is reduced to 17 mrad. Table 3.7 lists the results for the four cases.

		RELATIVE		EXTENT OF IMAGE
	MAX	MAIN LOBE	PSL	ABOVE -25 dB
	<u>AMP</u>	<u>GAIN (dB)</u>	<u>(dB)</u>	<u>(mrad)</u>
DSA	53.26	-2.30	-6.9	28
MSA	61.34	-1.08	-8.4	23
with nonoverlapping subarrays	66.68	-0.35	-10.0	18
with overlapping subarrays	69.43	0	-14.4	17

TABLE 3.7. COMPARISON OF DSA AND MSA, WITH AND WITHOUT SUBARRAY PROCESSING.

DATA SET 309 (HIGH STREET). TARGET IS A CORNER REFLECTOR. THE
AMPLITUDE VARIANCE OF THE BEAMFORMER IS 0.21.

Another example is shown in Figure 3.20. The 1-D images are of a target in the Limerick nuclear power plant. The target is located in bin 32. The beamformer is located in bin 26. The amplitude variance of its echoes across the array is 0.20. Table 3.8 lists the performances of the four procedures.

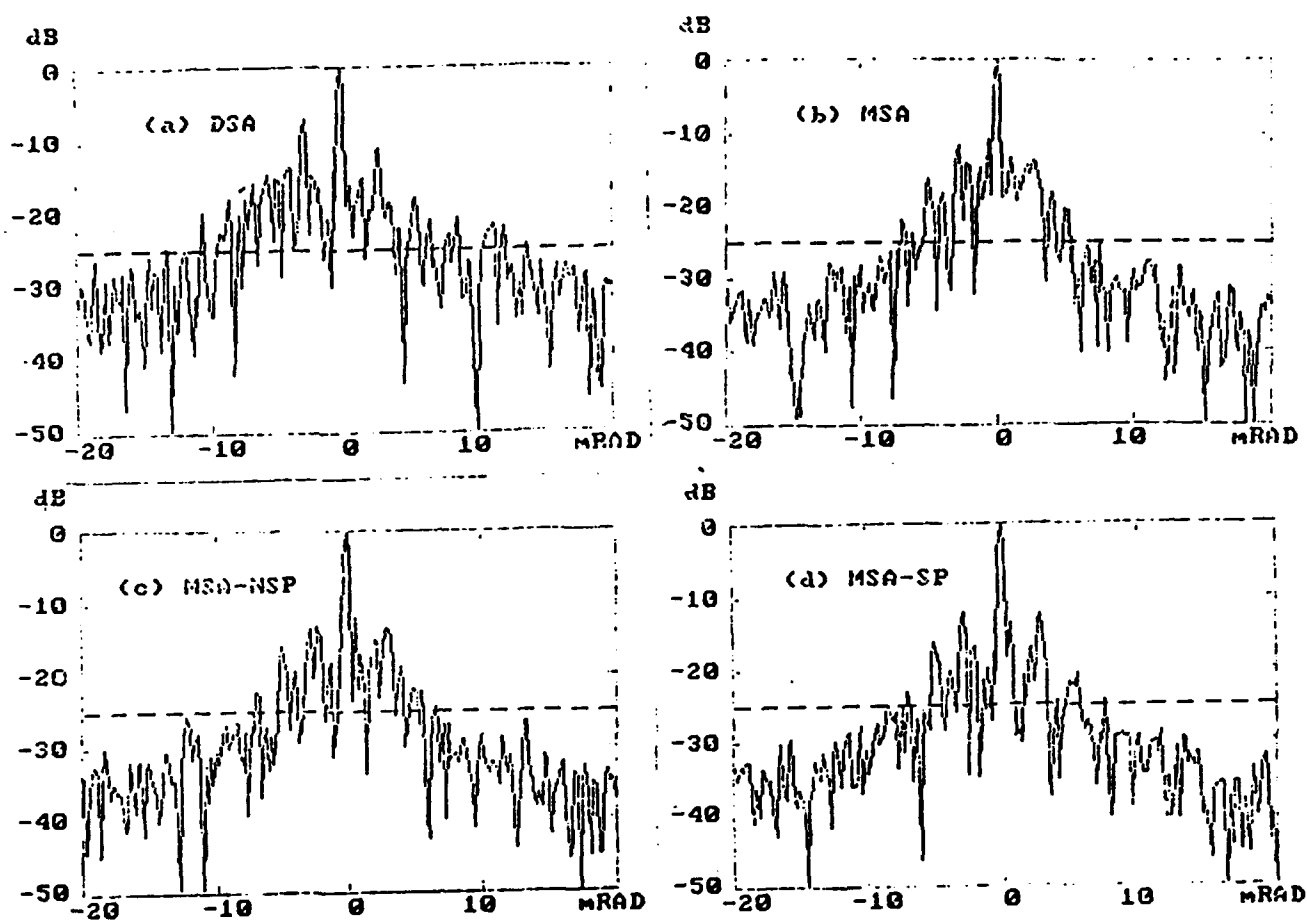


FIGURE 3.20 CROSS-RANGE IMAGES OF BIN 32 WITH LIMERICK NUCLEAR POWER PLANT (FROM [24] AND APPENDIX.)

- (a) DSA WITH BIN 26
- (b) MSA WITH BINS 17, 25 and 26
- (c) MSA WITH NONOVERLAPPING SUBARRAYS USING BINS 17, 25, 26 AND THREE SUBARRAYS
- (d) MSA WITH OVERLAPPING SUBARRAYS, USING BINS 17, 25, 26 AND THREE SUBARRAYS

		RELATIVE	EXTENT	
	MAX	MAIN LOBE	PSL	OF IMAGE
	AMP	GAIN (dB)	(dB)	ABOVE -25 dB
				(mrad)
DSA	51.08	-1.43	-6.9	24
MSA	56.89	-0.49	-10.7	13
with nonoverlapping subarrays	58.34	-0.28	-11.9	13
with overlapping subarrays	60.22	0	-12.1	13

TABLE 3.8. COMPARISON OF DSA AND MSA, WITH AND WITHOUT SUBARRAY PROCESSING.

DATA SET 301 (LIMERICK NUCLEAR POWER PLANT). THE AMPLITUDE
VARIANCE OF THE BEAMFORMER IS 0.20.

The results in these two experiments are similar. Comparing the top rows (DSA) in Tables 3.7 and 3.8 with the bottom rows (MSA with overlapping subarrays) we see an improvement in main lobe gain of about 2 dB, a reduction in sidelobe level of about 6 dB and a reduction in the angular size of the target of nearly 2:1.

3.10 OBSERVATIONS

A dominant scatterer algorithm will successfully self-calibrate a distorted phased array when a single suitable reflector (large RCS and small physical size) is embedded in clutter. The target-to-clutter ratio must be large enough to ensure that the reradiation wavefront is dominated by the prominent reflector. A test is the normalized amplitude variance of the echo across the array. A value of 0.12 or less ensures that the DSA will provide a useful image.

Under the same condition, the MSA will provide a slightly superior image but the improvement is often not sufficient to warrant the extra complexity. The strength of MSA is that it extends the useful variance range to 0.2. Subarray processing further improves its performance.

4. SPATIAL CORRELATION ALGORITHMS (SCA)

4.1 UNIT LAG ALGORITHM

Figure 3.3b showed a prominent scatterer imbedded in a cluttered range bin. The radiation field at the array was dominated by the large scatterer. As a consequence, the DSA was able to capture a relatively smooth, linear phasefront and self-calibration was successful. The situation pictured in Figure 3.3a is different. There no single scatterer is dominant. Instead, the field at the array (3.22) is the sum of randomly weighted plane waves arriving from random directions within the illuminated angular sector. Both situations are common. Corners figure prominently in manmade targets. Natural terrain such as farmland, crowns of trees and forests is less structured. Still more statistically homogeneous is sea clutter. The spatial correlation algorithm (SCA) was developed to handle these cases [17], [18]. This algorithm is also due to Attia.

Let $s(u)$ represent the complex reflectivity function of one of the range bins in Figure 3.3a. $s(u)$ can be considered a random process. For statistically homogeneous clutter, both the real and imaginary parts of $s(u)$ have pdfs that are independent of u . The source strength is the random process $s(u)$ modulated by the transmitted beam $f_T(u)$. Let $S = E\{|s(u)|^2\}$ be the mean squared value of the random process $s(u)$. The mean square scattered power as a function of u is then $S|f_T(u)|^2$.

The complex scatter strengths in the range bin shown in Figure 3.3a represent a sample function of the random process $s(u)$. It is reasonable to assume that the scattering functions $s(u)$ in many other range bins are also derived from the same random process, especially for target scenarios such as sea clutter. Consider the correlation between the data measured at two array points x_1 and x_2 , $R(x_1, x_2) = E\{e(x_1)e^*(x_2)\}$, where $e(x)$ is the data sample measured at aperture location x . The Van-Cittert Zernicke theorem states that $R(x_1, x_2)$ is spatially stationary when the underlying source distribution is incoherent, i.e., $R(x_1, x_2) = R(x_1 - x_2)$. Sea clutter echoes possess this property because the source distribution $s(u)$ is incoherent. The averaging required to estimate the correlation $R(x_1, x_2)$ can be performed over range because the source distribution $s(u)$, in different range bins, are different realizations of the same random process.

Under far-field conditions, the autocorrelation function $R(x)$ of the measured aperture data, and the mean angular power density function $I(u) = S|fT(u)|^2$, are Fourier transform pairs, as described by the Van-Cittert Zernicke theorem. The theoretical value is known because the transmitted power pattern is known. The measured correlation function will differ from the known theoretical value because of phase errors at the receiving aperture. The SCA uses the differences between the known and the measured correlation phases to estimate the unknown phase errors at the array elements.

The concept is introduced in simplified form by the following example. Assume that $|f_T(u)|$ is an even function of u , which is typical of most antenna patterns. Then $R(x)$ is real, by the property of the Fourier transform. Further, assume that far-field conditions prevail and that the receiving array is periodic.

These three assumptions, viz., an even transmitter pattern, far-field geometries and periodic receiving array are not necessary for the SCA; they are used for simplifying this discussion. The implications of the the three assumptions are discussed later.

Figure 4.1 sketches a periodic array of N elements steered to θ_0 , the angle from broadside. The phase shift ϕ_n in the n th channel is $nkdu_0$ where $k = 2\pi/\lambda$ is the wavenumber, d is the

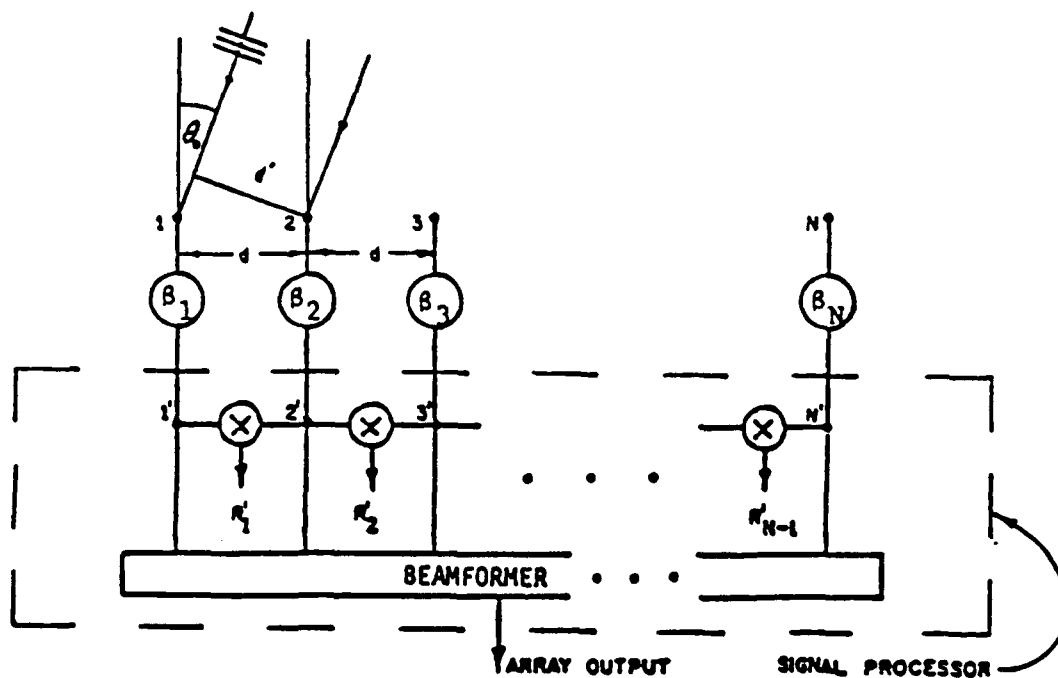


FIGURE 4.1 ARRAY MODEL AND SIGNAL PROCESSOR CONFIGURATION FOR SELF-SYNCHRONIZATION BY SPATIAL CORRELATION ALGORITHM (AFTER [17]).

element spacing, and $u_0 = \sin\theta_0$. There is a phase error β_n in the n th channel, resulting both from element position error and electrical mistuning. The left channel is considered the reference. Its phase error β is arbitrarily assigned the value of zero. In each channel but the reference channel is a phase-error correcting weight. The sum is the array output.

Information for determining the correct values of the weights is obtained from the products of signals in adjacent channels. The first product is $e_2' e_1'^*$, the second product is $e_3' e_2'^*$, and so on.

Each product is integrated or averaged over M range bins.

$$\hat{R}(2,1) = \frac{1}{M} \sum_m e_{2,m}' e_{1,m}'^* \quad (4.1)$$

is an estimate of the correlation coefficient of the radiation field between the first and second antenna elements modified by the phase-error difference $\beta_2 - \beta_1$, which, because β_1 is assigned the value of zero, equals β_2 . $\hat{R}(2,1)$ is a random variable having an expected value

$$E\{\hat{R}(2,1)\} = R(2,1) \exp(j\beta_2) \quad (4.2)$$

where $\hat{R}(2,1)$ is the error-free correlation coefficient. An estimate of the correlation coefficient $\hat{R}(2,1)$ is approximately equal to its mean, that is

$$\hat{R}(2,1) \simeq R(2,1) \exp j(\beta_2 - \beta_1) \quad (4.3a)$$

In a similar fashion

$$\hat{R}(3,2) \simeq R(3,2) \exp j(\beta_3 - \beta_2) \quad (4.3b)$$

$$\hat{R}(N,N-1) \simeq R(N,N-1) \exp j(\beta_N - \beta_{N-1}) \quad (4.3c)$$

Because of the far-field assumption, the correlation function is spatially stationary. That is, $R(i,j)$ depends only on $(x_i - x_j)$. Further, because the array is periodic

$$R(2,1) = R(3,2) = \dots = R(N,N-1) \quad (4.4)$$

Call this correlation coefficient $R(1)$. $R(n+1,n)$ is real and positive when (a) both the transmitter beam and the scatterer distribution are symmetrical about the optical axis of the transmitting antenna, and (b) the spacings between all adjacent elements are smaller than the lobe width of the correlation function. In this case, the measured arguments of the correlation coefficients provide estimates of the elemental phase errors:

$$\beta_1 = 0, \hat{\beta}_2 = \text{Phase}\{\hat{R}(2,1)\}, \hat{\beta}_3 = \hat{\beta}_2 + \text{Phase}\{\hat{R}(3,2)\}, \dots \quad (4.5a)$$

or

$$\hat{\beta}_n = \sum_{m=1}^{n-1} \text{Phase}\{\hat{R}(m+1,m)\}, \quad n > 1, \beta_1 = 0 \quad (4.5b)$$

The phase-compensation weight vector for the array is the conjugate of the phase-error vector.

4.12 UNIT LAG SCA FOR NEAR-FIELD GEOMETRY AND OFF-BROADSIDE STEERING

Three constraints were implied in the discussion above. First the transmitter pattern $f_T(u)$ was implicitly oriented broadside to the receiving array. Second, the description of the algorithm was given in far-field terms. Third, the array was assumed to be pe-

riodic. The implications of these assumptions on the ability of the SCA to calibrate the array is now discussed.

It is shown below that the near-field assumption is not necessary because the SCA automatically introduces the phase shift for focusing the array into the phase corrections $\hat{\beta}_n$.

With near-field curvature, the measured correlations, denoted $\hat{R}_1(m,n)$, can be expressed as

$$\hat{R}_1(m,n) \simeq \hat{R}(m,n) \exp[-jk(x_m^2 - x_n^2)/2r] \quad (4.6)$$

where x_m is the location of the m th element, r represents range, $\hat{R}(m,n)$ is the far-field correlation coefficient given by (4.1) and the Fresnel kernel $\exp(-jkx^2/2r)$ arises due to near-field curvature. The approximation indicates that the relationship (4.6) holds in the region of validity of the Fresnel transform.

Next, the effect of steering away from broadside is discussed. Assume that u_0 is the steering angle. The function $S|f_T(u - u_0)|^2$ is the scattered angular power density spectrum with the axis of symmetry generalized from $u = 0$ to $u = u_0$. From Fourier theory, it is easy to show that the measured phases of the correlation coefficients $\hat{R}(m,n)$ are multiplied by $\exp[jku_0(x_m - x_n)]$ to account for off-broadside steering. With near-field geometry and off-broadside steering included, the measured correlation coefficients, denoted $\hat{R}_2(m,n)$, can be expressed as

$$\hat{R}_2(m,n) \simeq \hat{R}(m,n) \exp\{jk[(x_m - x_n)u_0 - (x_m^2 - x_n^2)(1 - u_0^2)/2r]\} \quad (4.7)$$

where u_0 is the steering angle.

The spatial correlation algorithm uses the correlation phases to determine the phase errors. Spatial stationarity of the correlation function assumes that the phase of the far-field function $\hat{R}(m,n)$ equals $[\beta_m - \beta_n + \psi(x_m - x_n)]$, where $\psi(x_m - x_n)$ is the phase error of the error-free correlation coefficient. Therefore, the phase of $\hat{R}_2(m,n)$ in (4.7) can be expressed as

$$\begin{aligned} \text{Phase}\{\hat{R}_2(m,n)\} &= \{\beta_m + k[x_m u_0 - x_m^2(1-u_0^2/2r)]\} \\ &\quad - \{\beta_n + k[x_n u_0 - x_n^2(1-u_0^2/2r)]\} \\ &\quad + \psi(x_m - x_n) + \delta(m,n) \end{aligned} \quad (4.8)$$

The first (second) term on the right is the sum of the phase error at the m th (n th) element and the phase shift necessary to steer the m th (n th) element toward direction u_0 and range r . The third term is the phase of the error-free correlation coefficient $\hat{R}(m,n)$ and depends only on $(x_m - x_n)$. The fourth term $\delta(m,n)$ represents noise.

The unit lag SCA uses the phases of the $(N-1)$ correlation coefficients $\hat{R}_2(m,n)$ to determine the phase errors β_2, \dots, β_N relative to β_1 . Using (4.5b) and (4.8), the unit lag SCA phase error estimates can be expressed as

$$\begin{aligned} \hat{\beta}_n &= \sum_{m=1}^{n-1} \text{Phase}\{\hat{R}_2(m+1,m)\}, \quad n > 1 \\ &= \{\beta_n + k[x_n u_0 - x_n^2(1-u_0^2/2r)]\} + \sum_{m=1}^{n-1} \psi(x_{m+1} - x_m) \end{aligned}$$

$$+ \sum_{m=1}^{n-1} \delta(m+1, m) \quad (4.9)$$

The first term on the right is the sum of the phase error at the n th element and the phase shift necessary to steer the n th element toward direction u_0 and range r . The third term represents noise. The second term is the sum of the phases of the error-free correlation coefficient $\hat{R}(m+1, m)$, $1 \leq m \leq n-1$. The phase error estimates $\hat{\beta}_n$ become meaningless if this term varies randomly as a function of n .

There are two conditions under which the latter term does not affect the performance of the SCA:

(1) The array may be either periodic or aperiodic and the error-free correlation phases $\psi(m+1, m) = 0$ for all m , i.e., the error-free unit lag correlation coefficients $R(m+1, m)$ are real and positive.

(2) The array is periodic.

$R(m+1, m)$ will be real when the product of the transmitted beam pattern and the scatterer distribution is symmetrical about the optical axis. Further, $R(m+1, m)$ will be positive when all the spacings between adjacent elements $|x_{m-1} - x_m|$ are smaller than the null to null width of the correlation function $R(x)$. The width of the main lobe of $R(x)$ approximately equals the length of the transmitting antenna L_t . Thus the error-free correlation phases $\psi(m+1, m) = 0$ when (a) the product of the transmitting beam pattern and the scatterer distribution is symmetrical about the

optical axis and (b) $|x_{m-1} - x_m| \leq L_t$, all m . Under these conditions, the phase corrections can be rewritten as

$$\hat{\beta}_n = \{\beta_n + k[x_n u_0 - x_n^2(1-u_0^2/2r)]\} + \sum_{m=1}^{n-1} \delta_{(m+1,m)}, \quad n > 1 \quad (4.10)$$

Note that the phase correction $\hat{\beta}_n$ is the sum of the phase error β_n , the phase required to steer the n th element to direction u_0 and range r , and noise.

No assumption about array periodicity were made while deriving (4.10). Thus the unit lag SCA is capable of calibrating either periodic or aperiodic arrays when (a) the product of the transmitter beam pattern and the angular power density spectrum of the scatterer distribution is even with respect to the optical axis and (b) $|x_{m-1} - x_m|$ is smaller than half the null to null width of $R(x)$.

4.1.3 UNIT LAG SCA FOR COMPLEX CORRELATION FUNCTIONS

When the correlation function is not real and its phase varies rapidly in a nonlinear fashion with interelement spacing, there is no hope of using the correlation measurements to phase an aperiodic array. This can be seen by observing that the second term in (4.9), $\sum_{m=1}^{n-1} \psi(x_{m+1} - x_m)$, will vary randomly with n . Hence different random numbers become added to each of the phase corrections β_n , thereby rendering them useless for phase correcting the array.

However, a periodic array can be calibrated even under these circumstances. For a periodic array, the second term in (4.9),

$\sum_{m=1}^{n-1} \psi(x_{m+1} - x_m) = (n-1)\psi(d)$, where d is the interelement spacing and $\psi(d)$ is the phase of the correlation function $R(x)$ for $x = d$. Given this condition, the phase corrections in (4.9) can be expressed as

$$\begin{aligned} \hat{\beta}_n = & \{ \beta_n + k[x_n u_0 - x_n^2(1-u_0^2/2r)] \} + (n-1)\psi(d) \\ & + \sum_{m=1}^{n-1} \delta(m+1, m), \quad n > 1 \end{aligned} \quad (4.11)$$

In addition to the phase errors, the steering phase and noise, the phase correction contains a linear phase term $(n-1)\psi(d)$. This linear phase term has the effect of pointing the array away from u_0 . The beam pointing error Δu can be calculated by equating the linear phase variation $(n-1)\psi(d)$ to $k(n-1)d\Delta u$, giving the beam pointing error $\Delta u = \psi(d)/kd$.

Thus periodic arrays can be phase cohered by the unit lag SCA even when the phase of $R(x)$ varies rapidly, in a nonlinear fashion, with interelement spacing. Such a phase variation does cause a beampointing error. Beampointing errors are acceptable in applications such as imaging because the pointing error leads only to an image shift and not to a degradation in image quality. It is valuable also to note that when the phase of $R(x)$ can be approximated as a linear function having slope α for small lags, an aperiodic array can also be cohered; the beampointing error in this case is α/k .

9.1.4 EFFECT OF NOISE ON THE SCA

Eqs.(4.10) and (4.11) indicate that the phase corrections steer the array toward u_0 (or $u_0 + \Delta u$) and r , in addition to estimating the phase errors. From (4.9), the noise term in the phase correction for the n th element, denoted $\delta\phi_n$, can be expressed as

$$\delta\phi_n = \sum_{m=1}^{n-1} \delta(m+1,m), \quad n>1 \quad (4.12)$$

Clearly, the number of noise terms increases linearly with element number n . Thus one would expect the variance of the residual errors in the phase corrections to increase linearly with element number. This result was obtained in [17].

The increase in the residual phase error variance with element number results in a *decreasing* relative improvement in algorithm performance as the array grows in size. The gain of an array is expected to increase directly with the number of elements N . The rate of increase with the SCA is smaller, however. Because the phase error variance grows linearly with element number, the average phase error variance across the array grows with the number of elements. As a consequence, the loss in main lobe gain due to the residual phase error also grows with N . The formula for the normalized main beam expected gain of a *periodic* array cohered by the SCA is given approximately in [17] as

$$E\left[\frac{G}{G_0}\right] = \frac{1}{N} + \frac{2}{N^2} \frac{r^{1/2}[(N-1) - Nr + r^N]}{(1-r)^2} \quad (4.13)$$

where $r = \exp(-\sigma_\delta^2)$ and σ_δ^2 is the variance of the noise terms

$\delta(m+1,m)$ in (4.8).

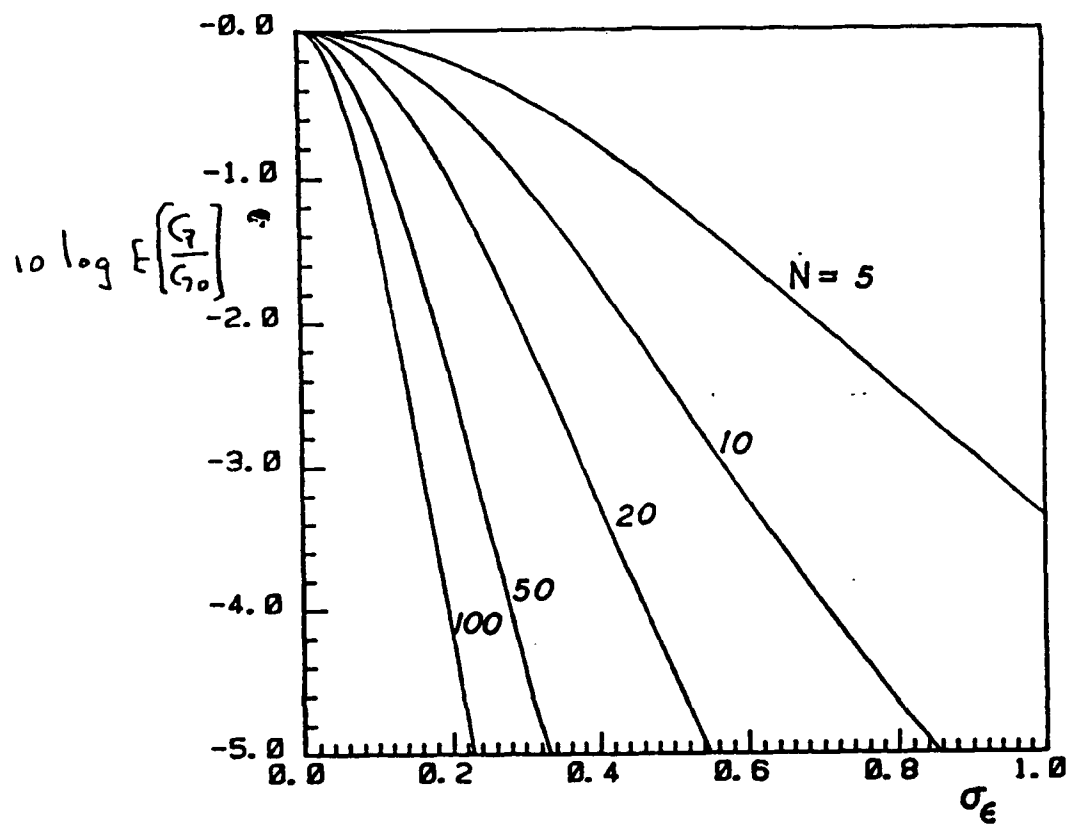


FIGURE 4.2 NORMALIZED MAIN-BEAM GAIN (dB) VERSUS σ_ϵ (rad)
FOR THE SPATIAL CORRELATION ALGORITHM (FROM [17]).

4.2 UNIT LAG SCA EXPERIMENTS

4.2.1 COMPUTER SIMULATIONS

In [17], a CLUTTER patch was simulated on the computer at X-band ($\lambda = 3$ cm) by uniformly distributing a large number of scatterers (1000) within its boundary ($\Delta R = 15$ m, $\Delta \theta = 0.06$ rad). The phase of each scatterer was taken as an independent random variable uniformly distributed over the interval $[-\pi, \pi]$, while its amplitude was taken to be proportional to both the transmitter radiation pattern and a uniformly distributed random quantity. The SCA was tested through the simulation of periodic and random arrays. Random unknown phase errors uniformly distributed over the interval $[-\pi, \pi]$ were inserted in each receiving channel. Also, an independent additive narrowband Gaussian noise component was injected into each channel on reception. It is reported in [17] that the algorithm was highly successful, always enabling the recovery of the error-free radiation pattern almost completely. Figure 4.3 shows the results of one such simulation experiment. It corresponds to an $N = 20$ element random array with a nominal length $L = 100\lambda$. The clutter-to-noise ratio (CNR) is 20 dB and the sample size $M = 100$. The solid line plots the error-free radiation pattern while the dotted line represents the distorted pattern (due to the phase errors). The dashed line plots the pattern recovered by applying the SCA. The agreement is excellent.

4.2.2 A SEA CLUTTER EXPERIMENT

In the Naval Research Laboratory experiment referenced earlier in Section 3.5 the radar data-taking equipment was also flown over the North Atlantic Ocean. Eight channels of sea clutter

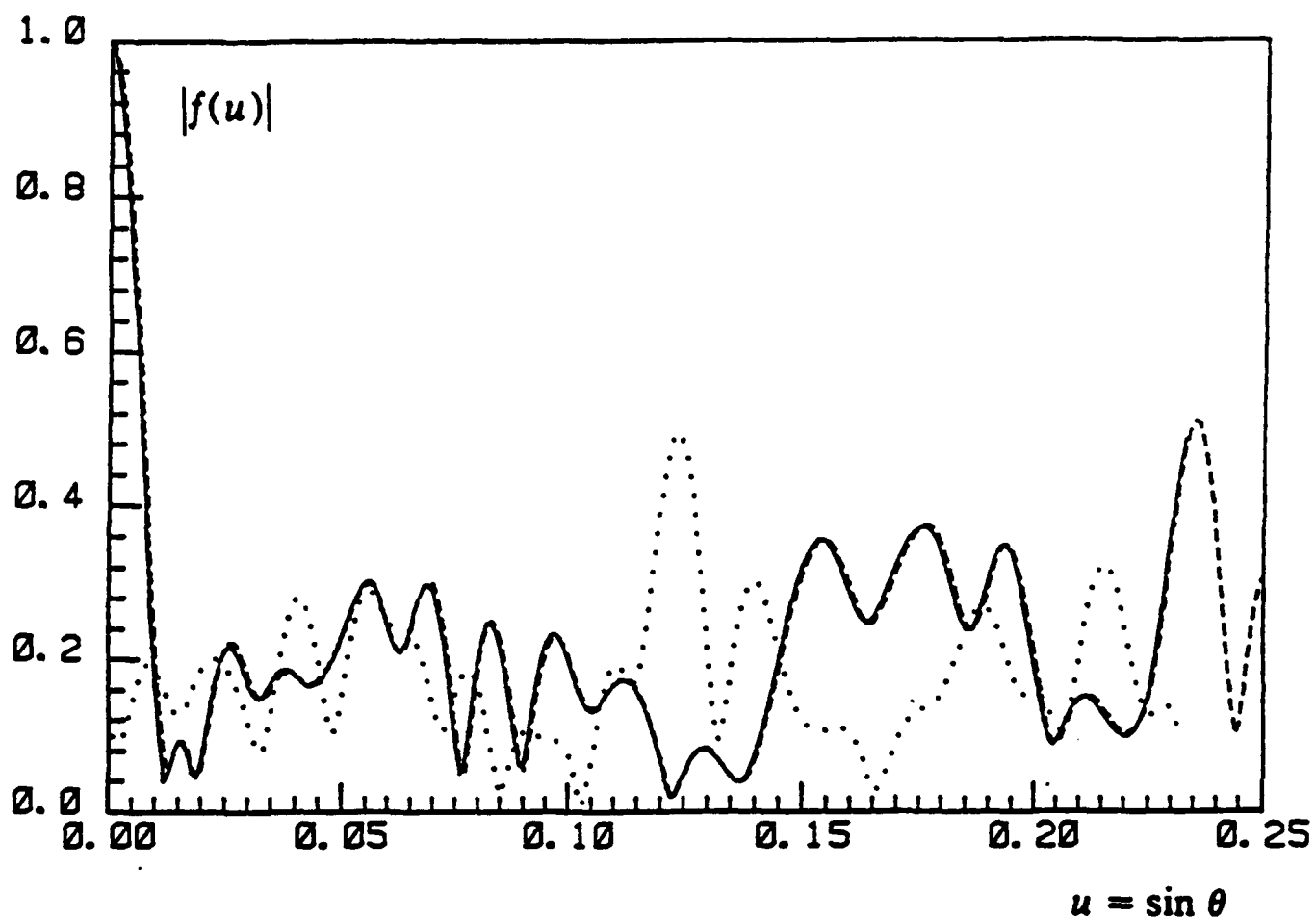


FIGURE 4.3 COMPUTER SIMULATION EXPERIMENT OF THE UNIT-LAG SPATIAL CORRELATION ALGORITHM. (—) ERROR-FREE PATTERN, (...) DISTORTED DUE TO PHASE ERRORS, (- - -) RECOVERED BY THE ALGORITHM ($N=20$, $L=100\lambda$, $CNR=20$ dB), $M=100$). (FROM [21].)

echoes were recorded, one for each dipole antenna in the array, in response to each pulse transmission. The receiving antenna was a rigid, 8-element equal-gain phased receiving array operating at 850 MHz. Its radiation pattern was of the form $\sin Nx/N\sin x$ where $N = 8$ was the number of elements and x is proportional to the sine at the angle from boresite. Its peak sidelobe is approximately -12 dB. The pattern is shown as the solid curve in Figure 4.4.

To conduct the experiment, random phases representing element position errors and electrical system errors were added in each channel. The distribution of these phase errors was uniform in the interval $[-\pi, \pi]$. Phase errors destroyed the radiation pattern, as expected; it is shown as the dotted curve. Sea clutter echoes measured in each of the eight receiving channels were then phase-shifted by these random phases and applied to the SCA. 100 range bins of data were used to smooth the correlation estimates. Phase corrections were calculated from the measured correlation coefficients according to (4.7) and cascaded with the random phase errors. The radiation pattern based upon the composite weight vector is shown dashed in the figure. It is nearly indistinguishable from the original, error-free pattern down to the third sidelobe, where the difference is 1.8 dB at the level of -16 dB. There would be no way to distinguish these patterns in a realistic operating system. This experiment demonstrates the ability of the SCA to phase-compensate on sea clutter; it is typical of many similar tests.

Two-dimensional SCA experiments on ground clutter and on complicated echoes from an airplane also were performed. These

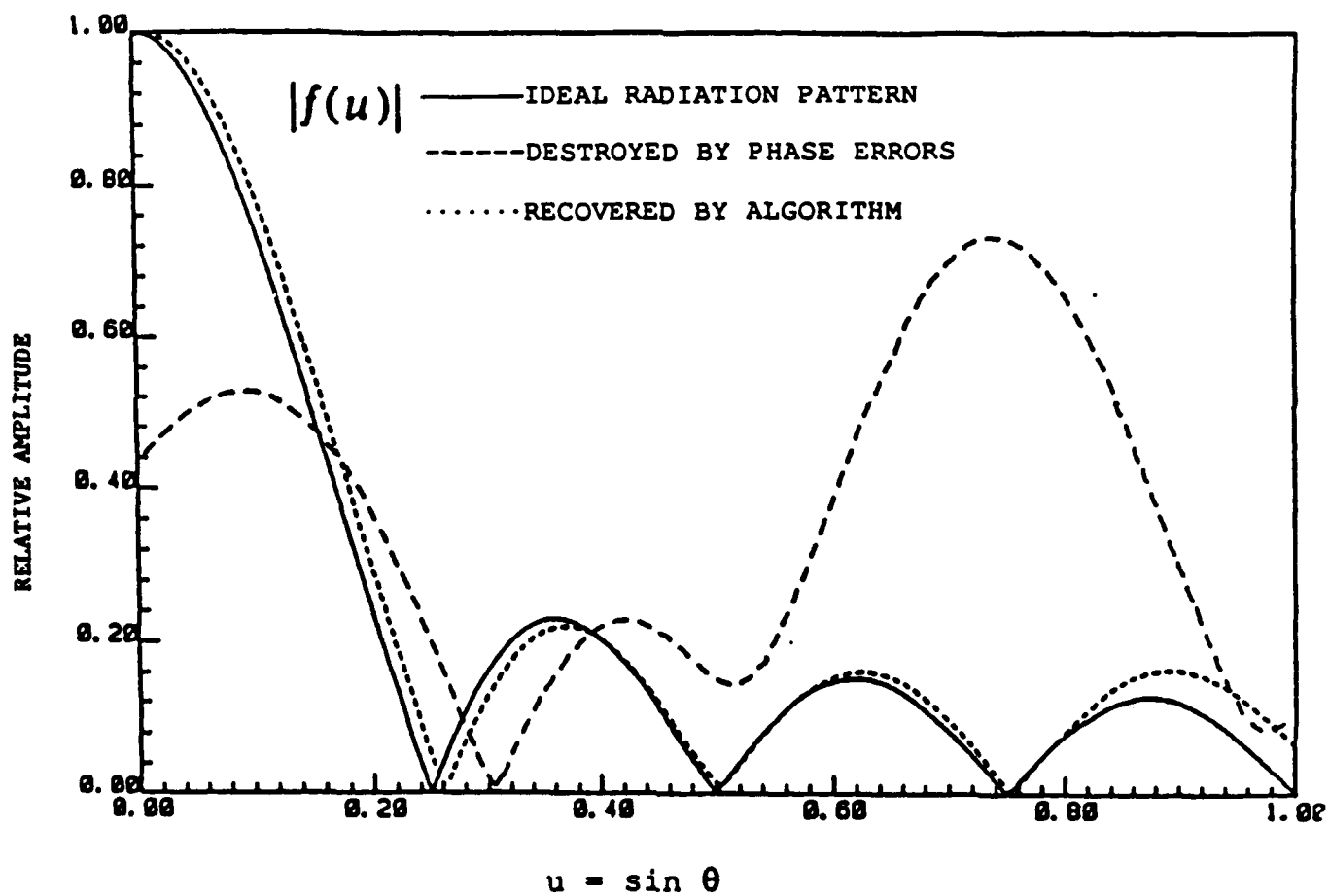


FIGURE 4.4 SEA CLUTTER EXPERIMENT WITH UNIT-LAG SPATIAL CORRELATION ALGORITHM.

results are shown in Section 4.4 where the performances of several algorithms are compared.

4.3 MULTIPLE LAG SCA

4.3.1 MULLER'S THEOREM

The SCA described in Section 4.1 employed only the unit lag correlation coefficient of the correlation function. The phase errors were derived directly from the arguments of the measured values of $R(1)$ at each point in the array. By the same procedure that led to (4.5), it is easy to see that other correlation coefficients contain phase error information as well. Consider $R(2)$, for example. It provides the phase error between two elements, spaced by twice the interelement spacing, at each point in the array at which it is measured. Similarly, $R(3)$ provides the phase error between two elements spaced by three times the interelement spacing. Thus measurement of all the available coefficients $R(1)$ through $R(N-1)$ provides phase error information as directly as $R(1)$ alone. The obvious question to be answered is "If $R(1)$, measured everywhere in the array, solves the phase-error compensation problem, why utilize any other, more complicated correlation algorithm?"

The answer is that three factors limit the quality of the unit lag correlation measurements $\hat{R}_{n,n+1} \triangleq \hat{R}(n,n+1)$. The first is noise. The quality of the estimate is a function of the signal-to-noise ratio (SNR) of the measured samples of the electric field, e_n and e_{n+1} . Second, the quality is not only impaired when the SNR is low. It is also impaired when the e-field is low at some point or points in the array. This condition easily occurs when the source function $\rho(u)$ contains a small number of strong reflectors.

Third, the number of range bins used for smoothing the correlation coefficients may be insufficient to produce suitably accurate estimates of the phase errors.

When any or all of these conditions prevail, the estimated phase errors, deduced from the arguments of $\hat{R}(n, n+1)$, can be in error. The solution is to measure the same phase errors through other correlation coefficients. In essence, an additional domain of averaging or smoothing is introduced.

Historically, the concept was first introduced by Muller as an important theorem in optical telescropy [20]. The problem of poor seeing conditions has plagued astronomers since the invention of the telescope. The problem is due to the nonhomogeneity of the refractive index of the atmosphere. Muller discovered that it is possible to fully phase-compensate a multiple mirror telescope (analogous to a phased array with very large subapertures for elements) by feedback controlling optical time delays placed in front of each optical aperture so as to maximize the integral of certain functions of the square of the image intensity in the composite image plane. Because of the Fourier relations between the e-field in the aperture and the image, and between an intensity image and the autocorrelation in the aperture, Muller's iterative algorithm can be replaced by a noniterative function of the autocorrelation coefficients measured in the aperture. This procedure is now described.

Of the class of solutions discovered by Muller the simplest one to describe is as follows. Let the image formed by the i th mirror be I_i . Let all the images be brought together onto a common

focal plane and registered. Form an objective function J , called the sharpness function, that is the integral of the square of the intensity distribution in the image plane. Let the time delays referred to above be represented more generally by a set of weights w_i . The optimization or search procedure adjusts the w_i until

$$\frac{\partial J}{\partial w_i} = 0, \text{ all } i \quad (4.14)$$

The theorem demonstrates that when this condition is achieved the wavefront distortion has been fully compensated and that the image is without error, except for an arbitrary and unknown displacement of the optical axis.

In mathematical terms, let $s = s(u)$ be the source distribution, $f_0 = f_0(u)$ the design radiation pattern and $f = f(u) = f_0 + \delta f$ the actual pattern. The optimum complex image is

$$\hat{s}_0 = s * f_0 \quad (4.15)$$

while the actual distorted image is

$$\begin{aligned} \hat{s} &= s * f = s * (f_0 + \delta f) \\ &= \hat{s}_0 + \delta s \end{aligned} \quad (4.16)$$

The display $I = I(u)$ is either the magnitude or the square magnitude of (4.16) and I_0 is displayed when the radiation pattern is error free. The statement of the theorem is that

$$I(u) = I_0(u + \delta u) \quad (4.17)$$

when (4.14) is satisfied, where δu is the shift in the optical axis.

A limitation of the theorem is the requirement that the radiation field upon which it operates be derived from an incoherent distribution of sources. Stars, being independent energy generators, satisfy this requirement. The phase relations between the radiations from each source within the passbands of the receivers are continuously changing. The result is a radiation field at the receiving antenna which is continuously changing but whose statistics are invariant with time.

4.3.2 THE MICROWAVE CASE

Not so in microwave radar, however. There the phase relations between the echoes from targets are dictated by the geometry of the locations of the transmitter, the targets, and the receiver. Each transmitted pulse results in the same set of echoes and hence the same radiation field at the receiving array.

Figure 4.5 schematically portrays a surface J as a function of two weights, indicated by the phase shifts ϕ_1 and ϕ_2 when the radiation field is not incoherent. The surface shown has multiple maxima and the search procedure can mistakenly settle for a non-global peak. The optimum weights are the coordinates of the maximum modal point of the surface.

The primary potential benefit of the procedure, in microwave radar, is less its ability to compensate for medium turbulence than for distortion in the aperture. Large antenna systems will be

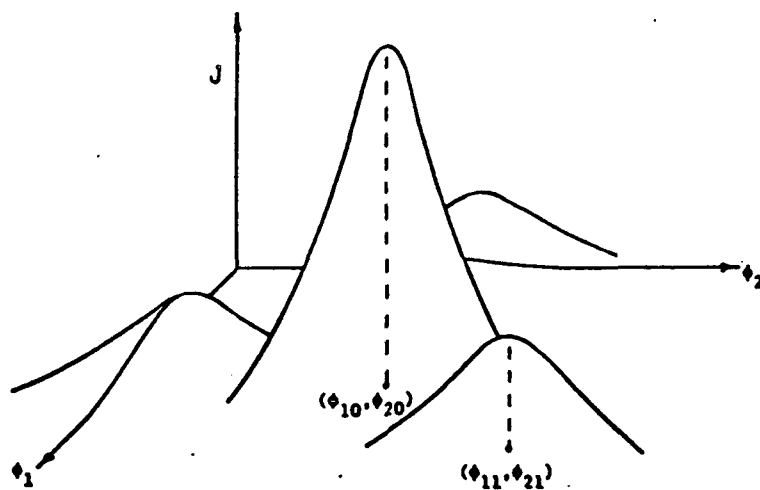


FIGURE 4.5 SHARPNESS FUNCTION IS GLOBALLY MAXIMIZED BY CORRECT PHASE COMPENSATORS ϕ_{10} and ϕ_{20} .

intrinsically distorted due to nonrigidity of their structures, differences in gravitational forces across the antennas, differential windloading, differential weather, etc. To achieve the benefits of self-calibration based upon Muller's theorem, a means must be developed for altering the phase relations of the electric fields reflected from the targets so as to emulate an incoherent distribution of radio sources.

Two methods for doing so have been developed. Each method builds up a diversity image suitable for initiation of the search for the weight vector. The first procedure uses transmitter location diversity as its tool [19]. The second procedure uses range bin diversity (Section 4.1). Transmitter diversity solves the problem completely. Its limitation is its practicality, however, for it is not a solution applicable to all system designs. The diversity image I_D is the weighted sum of images $I_m, m=1,2,\dots,M$, obtained from a set of M snapshots of the radiation field. These images are called trial images or constituent images. The trial images differ either because the diversity procedure alters the radiation pattern between images or because the procedure alters the phase relations among scatterers in the source function, or both. Thus the diversity image to which the search procedure (3.57) is applied can be written

$$I_D = \sum_{m=1}^M a_m I_m \quad (4.18)$$

9.3.3 RELATIONSHIP BETWEEN MULLER'S OBJECTIVE FUNCTION AND APERTURE CORRELATION FUNCTIONS

Assuming that the characteristics of the diversity image (4.18) are consistent with an incoherent distribution of sources, its inverse Fourier transform is the autocorrelation function $R = R(x)$ in the aperture, i.e.,

$$R = F^{-1}I \quad (4.19)$$

and the inverse Fourier transform of I^2 is

$$F^{-1}I^2 = F^{-1}I * F^{-1}I = R * R \quad (4.20)$$

Muller's objective function

$$J = \int I^2(u) du = R(x) * R(x) |_{x=0} = \int R^2(x) dx \quad (4.21)$$

or in discrete terms

$$J = |R(0)|^2 + 2 \sum_{l=1}^{N-1} |R(l)|^2 \quad (4.22a)$$

where

$$R(l) = A_l \exp(j\psi_l) = \sum_{n=1}^{N-1} R(n+l, n), \quad l \geq 0 \quad (4.22b)$$

$$R(-l) = R^*(l) \quad (4.22)$$

Thus Muller's objective function can be calculated from correlation coefficients measured in the aperture. An iterative procedure developed by Subbaram is now described. This algorithm uses the complete correlation function rather than its phase alone. The advantage of using the complete correlation coefficient lies in the accuracy of the phase measurement. When the modulus is large the phase is easy to measure, in which case both

procedures are equally effective. When the modulus is small, however, the phase measurement is subject to considerable error due to noise and the algorithm suffers. By using the entire complex coefficient the amplitude of \hat{R} acts as a weight upon the measured phase. In this way noise-induced phase measurement errors are suppressed.

The measured values of $R(n+1, n)$ will be in error because of aperture and/or medium distortion. The correlation coefficient for lag 1, after introducing the phase corrections $\hat{\beta}_n$, may be written

$$\hat{R}_1 = \sum_{n=1}^{N-1} \hat{R}(n+1, n) \exp[j(\hat{\beta}_n - \hat{\beta}_{n+1})] \quad (4.23)$$

Referring to (4.22), observe that $R(0)$ is independent of both the phase errors and phase corrections. Thus it can be dropped from the objective function. Further, the correlation coefficients for large lags have a tendency to be noisy; therefore it is better to use only a limited number of correlation lags in the objective function. Modifying J in (4.22a) by using only lags one through L results in

$$\begin{aligned} F &= \sum_{l=1}^L \left| \sum_{n=1}^{N-1} \hat{R}(n+1, n) \exp[-j(\hat{\beta}_{n+1} - \hat{\beta}_n)] \right|^2 \\ &= F_1 + F_2 + \dots + F_L \end{aligned} \quad (4.24)$$

The first term is

$$F_1 = \left| \sum_{n=1}^{N-1} \hat{R}(n+1, n) \exp[-j(\hat{\beta}_{n+1} - \hat{\beta}_n)] \right|^2 \quad (4.25)$$

An algorithm that maximizes F_1 with respect to the phase corrections $\hat{\beta}_n$ may be called a unit lag spatial correlation algorithm. Maximizing the additional terms in F generalizes the spatial correlation algorithm up to the L th lag by attempting to cophase the measured correlation data from lags 1 through L . When the correlation data are distorted only by phase errors, i.e.,

$$\hat{R}(n+l, n) = A_l \exp[j(\psi_l + \beta_{n+l} - \beta_n)], \quad (4.26)$$

the phase corrections $\hat{\beta}_n$ will cophase all the $\hat{R}(n+l, n)$ for lags one through L . In other words, the phase correction $\hat{\beta}_n$ will make F equal to its global maximum when the measured correlation data $\hat{R}(n+l, n)$ are error-free except for a phase shift of $\beta_{n+l} - \beta_n$. In realistic situations, the amplitudes of the correlation data having the same lag l will not be constant because of noise and an insufficient number of range bins available for smoothing the correlation data. Further, the phases of the measured correlation data will not be equal to $\psi_l + \beta_{n+l} - \beta_n$ due to the same reason. Hence F cannot reach its global maximum when the measured correlation data are contaminated by noise. The set of phase corrections obtained by maximizing F will attempt to cophase the correlation data giving the largest weight to the lags that have the largest amplitude, and small weights to lags that have small amplitudes. Thus maximizing F in order to obtain the phase corrections overcomes the three deficiencies of the spatial correlation algorithm mentioned at the beginning of this section.

9.3.4 MULLER'S THEOREM IN THE APERTURE DOMAIN

The following proposition derives an expression for the phase corrections $\hat{\beta}_n$ that are obtained by maximizing F . A computationally efficient algorithm for maximizing F is then presented.

PROPOSITION

Maximizing the objective function F with respect to the phase corrections $\hat{\beta}_n$ yields the following set of phase corrections:

$$\hat{\beta}_n = \beta_n + c_0 + (n-1)c_1, \quad 1 \leq n \leq N \quad (4.27)$$

In other words, the phase corrections $\hat{\beta}_n$ obtained by maximizing F are equal to the sum of the phase errors β_n , an arbitrary constant c_0 , and an arbitrary phase tilt having a slope c_1 . The constant c_0 is of no importance because it merely adds a phase c_0 to each image pixel. The constant c_1 shifts the image by an amount $\Delta u = -c_1/kd$ for an array with interelement spacing d . Thus the phase-corrected image $\hat{s}(u)$ is a version of the error-free image $s_0(u)$ multiplied by a constant e^{jc_0} .

PROOF OF PROPOSITION

The phase corrections obtained by maximizing F are shown to have the form given by (4.27). Any set of N quantities a_0, \dots, a_{N-1} can be written in terms of a polynomial of order $N-1$, i.e., $a_n = \sum_{k=0}^{N-1} c_k (n-1)^k$, where the c_k are the coefficients of the polynomial.

Expanding the $\hat{\beta}_n - \beta_n$ in this fashion leads to

$$\hat{\beta}_n = \beta_n + \sum_{k=0}^{N-1} c_k (n-1)^k \quad (4.28)$$

Further, assume that the only distortion in the measured correlation data is due to the phase errors β_n , as in (4.26). Clearly, F , defined in (4.24), reaches its maximum when all components in the summation over n are cophased. Consider a single component F_1 of F . From (4.24)

$$F_1 = \left| \sum_{n=1}^{N-1} \hat{R}(n+1, n) \exp[-j(\hat{\beta}_{n+1} - \hat{\beta}_n)] \right|^2 \quad (4.29)$$

Substituting (4.28) and (4.26) into (4.29) yields

$$\begin{aligned} F_1 &= A_1^2 \left| \sum_{n=1}^{N-1} \exp[-j(\hat{\beta}_{n+1} - \beta_{n+1} - \hat{\beta}_n + \beta_n)] \right|^2 \\ &= A_1^2 \left| \sum_{n=1}^{N-1} \exp \left\{ j \sum_{k=0}^{N-1} c_k [(n-1)^k - (n+1-1)^k] \right\} \right|^2 \quad (4.30) \end{aligned}$$

F_1 reaches its maximum when each term in the outer summation over n has the same phase. This occurs when the exponential terms in the summation are independent of n . Consider a single exponential term inside the summation. Its exponent is the sum of N terms $c_k[(n-1)^k - (n+1-1)^k]$, $0 \leq k \leq N-1$. For $k = 0$, this quantity is $c_0(1-1) = 0$, which is independent of n . The second or $k = 1$ term is $c_1(n-1-n-1-1) = c_1 l$, which is a function of l but not of n . The third term is $c_2(2l - 2nl - l^2)$. This term is a function of n . Therefore the phase of each term in the summation over n will be

Therefore the phase of each term in the summation over n will be different if $c_2 \neq 0$. The requirement that each term in the summation be cophased at the maximum of F_1 therefore demands that $c_2 = 0$. In a similar fashion, it is easy to show that all the c_k , $k \geq 2$, are zero at the maximum F_1 . The same conclusion holds for all components of F , i.e., for all F_l , $1 \leq l \leq L$. Using $c_k = 0$, $k \geq 2$, in (4.28) yields

$$\hat{\beta}_n = \beta_n + c_0 + (n-1)c_1 \quad (4.31)$$

as claimed in (4.27).

The following discussion shows that the linear phase error $(n-1)c_1$ shifts the image from the origin by an amount $\Delta u = -c_1/kd$, where d is the interelement spacing. This can be seen by examining the phase-corrected image $\hat{s}(u)$ given by

$$\hat{s}(u) = \sum_{n=1}^N \hat{e}_n e^{-jkdu(n-1)} e^{-j\hat{\beta}_n} \quad (4.32)$$

The \hat{e}_n are equal to the error-free data samples e_n shifted in phase by the phase error β_n . Using $\hat{e}_n = e_n \exp(j\beta_n)$ in (4.32) leads to

$$\hat{s}(u) = \sum_{n=1}^N e_n e^{-j(\hat{\beta}_n - \beta_n)} e^{-jkdu(n-1)} \quad (4.33)$$

Substitution of (4.31) into (4.33) yields

$$\hat{s}(u) = e^{-jc_0} \sum_{n=1}^N e_n e^{-jkd(n-1)(u+c_1/kd)}$$

$$= e^{-jc_0} s_0(u+c_1/kd) \quad (4.34)$$

Thus the phase-corrected image $\hat{s}(u)$ is a shifted version of the error-free image $s_0(u)$ multiplied by a constant $\exp(jc_0)$.

9.3.5 A COMPUTATIONALLY EFFICIENT ALGORITHM FOR MAXIMIZING THE OBJECTIVE FUNCTION F

The objective function F has to be maximized with respect to $(N-1)$ parameters $\hat{\beta}_2, \hat{\beta}_3, \dots, \hat{\beta}_N$ (remember that $\hat{\beta}_1 = 0$). Setting the derivatives of F with respect to the $\{\hat{\beta}_n\}$ to zero yields a set of $(N-1)$ transcendental equations for the $(N-1)$ unknowns. No closed form solution for this set of equations has been found; hence F has to be maximized iteratively.

There are four major steps in the following iterative algorithm:

1. Choose $\hat{\beta}_1 = 0$ and $\hat{\beta}_n, n > 1$, using the spatial correlation algorithm (Section 4.1).
2. Maximize F sequentially with respect to the $\hat{\beta}_k, 2 \leq k \leq N$, while keeping the rest of the $\hat{\beta}_n, n \neq k$, constant. Calculate the global maximum F_{\max} from the data.
3. Check if F is close to F_{\max} . If not, repeat step 2. Otherwise, go to step 4.
4. Modify the set of phase corrections to minimize the displacement of the optical axis.

Step 1 is described in Section 4.1. The remaining steps are now described.

Step 2. Because F has several local maxima, conjugate gradient algorithms cannot be used to accomplish this task. An algorithm that maximizes F efficiently is now developed. This algorithm exploits the fact that F is almost a sinusoidal function of a single $\hat{\beta}_k$ when the other $\hat{\beta}_n$, $n \neq k$, are held constant, that is

$$F(\hat{\beta}_k) \simeq A_k \sin(\hat{\beta}_k + \phi_k) + B_k \quad (4.35)$$

where A_k , ϕ_k and B_k are unknown constants. To prove (4.35), consider a single component of $F(\hat{\beta}_k)$ (say $F_1(\hat{\beta}_k)$) in terms of $\hat{\beta}_k$ holding the $\hat{\beta}_n$, $n \neq k$, constant.

In (4.29) the terms that contain $\hat{\beta}_k$ are

$$\begin{aligned} a_1 &= \hat{R}(k, k+1) \exp(-j\hat{\beta}_{k+1}) \text{ if } k+1 \leq N \\ &= 0 \text{ otherwise} \end{aligned}$$

and

$$\begin{aligned} a_2 &= \hat{R}(k, k+1) \exp(j\hat{\beta}_{k-1}) \text{ if } k-1 \geq 1 \\ &= 0 \text{ otherwise} \end{aligned}$$

The remainder

$$\begin{aligned} a_3 &= \sum_{n=1}^{N-1} \hat{R}(n, n+1) \exp[-j(\hat{\beta}_{n+1} - \hat{\beta}_n)] \\ &\quad n \neq k \text{ or } n \neq k-1 \end{aligned}$$

is independent of $\hat{\beta}_k$. Thus

$$F_1(\hat{\beta}_k) = a_1 e^{j\hat{\beta}_k} + a_2 e^{-j\hat{\beta}_k} + a_3 \quad (4.36)$$

Because the algorithm begins with the unit lag spatial correlation method (step (1)) which provides high quality initial estimates of

the β_n , all components of the sum a_3 are nearly cophased and, because a_3 is the sum of $N-1-2$ terms each of the type a_1 or a_2 , $|a_3| \gg |a_1|$ and $|a_2|$. Using this fact in (4.36) yields an expression for $F_1(\hat{\beta}_k)$ of the form

$$F_1(\hat{\beta}_k) \simeq A \sin(\hat{\beta}_k + \phi) + B, \quad 1 \leq l \leq L$$

where terms containing $\exp(\pm j2\hat{\beta}_k)$ have been ignored because their magnitude $|a_1 a_2|$ is much smaller than the magnitude of the terms containing $\exp(\pm j\hat{\beta}_k)$. The sum of L sinusoids of the form shown above is also a sinusoid; hence $F(\hat{\beta}_k)$ is of the form shown in (4.35).

The iterative algorithm first maximizes F with respect to $\hat{\beta}_2$, then does the same for $\hat{\beta}_3$, etc. After going through a cycle of maximizing F with respect to the $\hat{\beta}_n$, $2 \leq n \leq N$, the value of F is compared to F_{\max} . The iterations are stopped when F is close to F_{\max} . Equation (4.35) is used in order to maximize F with respect to a single $\hat{\beta}_k$ while holding the remaining $\hat{\beta}_n$, $n \neq k$, constant. Note that $F(\hat{\beta}_k)$ reaches its maximum value ($= A_k + B_k$) when $\hat{\beta}_k = (\pi/2) - \phi_k$. The value of ϕ_k can be computed by evaluating $F(\hat{\beta}_k)$ at three points. For example,

$$S_1 \stackrel{\Delta}{=} F(0) = A_k \sin \phi_k + B_k$$

$$S_2 \stackrel{\Delta}{=} F\left(\frac{\pi}{2}\right) = A_k \cos \phi_k + B_k$$

and

$$S_3 \stackrel{\Delta}{=} F(\pi) = -A_k \sin \phi_k + B_k$$

Then $\tan \phi_k = (S_1 - S_3) / (2S_2 - S_1 - S_3)$, and hence the optimal value of $\hat{\beta}_k$ is

$$\hat{\beta}_k \Big|_{\text{opt}} = \frac{\pi}{2} - \tan^{-1} \left(\frac{S_1 - S_3}{2S_2 - S_1 - S_3} \right) \quad (4.37)$$

Thus maximizing F with respect to a single $\hat{\beta}_k$ involves computing F for only three values of $\hat{\beta}_k$.

Step 3. Any iterative algorithm needs a stopping criterion. Fortunately, the value of the global maximum of F can be computed from the data because each term in the summation over n in (4.24) will have the same phase when F reaches its maximum. Thus, the maximum value of F , denoted F_{max} , i.e.,

$$F_{\text{max}} = \sum_{l=1}^L \left| \left(\sum_{n=1}^{N-1} \hat{R}_{n+1,n} \right) \right|^2 \quad (4.38)$$

Step 4. It is useful to minimize the shift of the phase-corrected image ($= -c_1/Rd$ from (4.34)). Clearly, the magnitude of the phase-corrected image will be identical to the magnitude of the error-free image if $c_1 = 0$. The shift of the phase-corrected image will be minimized if c_1 can be estimated.

Consider the phase-corrected unit lag phase; that is, consider

$$\text{Phase} \left\{ \hat{R}_{(n+1,n)} e^{-j(\hat{\beta}_{n+1} - \hat{\beta}_n)} \right\} = \psi_1 - c_1 \quad (4.39)$$

The identity in (4.39) results when (4.26) and (4.31) are used for $\hat{R}(n, n+1)$ and $\hat{\beta}_n$, respectively. Note that $c_1 = 0$ if the phase of the corrected correlation data for unit lag are set to ψ_1 . Hence c_1 can be set to zero if the unit lag correlation phase is known. For most target scenarios, the unit lag autocorrelation phase is approximately equal to $-kdu_0$, where d is the interelement spacing and u_0 is the center of the field of view (the direction towards which the transmitter is pointed). Therefore, an estimate of ψ_1 , denoted $\hat{\psi}_1$, is $-kdu_0$. Thus c_1 can be estimated by comparing the phase of the unit lag phase-corrected correlation values to $\hat{\psi}_1$, i.e.,

$$\hat{c}_1 = \hat{\psi}_1 - \text{Phase} \left\{ \hat{R}(n+1, n) e^{-j(\hat{\beta}_{n+1} - \hat{\beta}_n)} \right\} \quad (4.40)$$

Thus the shift in the image plane can be minimized after maximizing F by subtracting out $(n-1)\hat{c}_1$ from the $\hat{\beta}_n$. The final set of phase corrections, denoted $\hat{\beta}'_n$, are

$$\hat{\beta}'_n = \hat{\beta}_n - (n-1)\hat{c}_1 \quad (4.41)$$

where the $\hat{\beta}_n$ are obtained by maximizing F and \hat{c}_1 is defined by (4.40).

4.4 MULTIPLE LAG SIMULATION EXPERIMENTS

Figure 4.6 is a computer simulation experiment in which transmitter diversity performed the decohering function. Two equal strength point targets are located at $u = -0.3$ and 0.5 . The solid curve shows the one-dimensional image of the two targets obtained using an 11-element periodic receiving array. The dotted curve

shows the useless image that resulted when random phase errors were added at each receiver. The error distribution was uniform over the interval $\pm\pi$.

Images were then computed for five different locations of the transmitter. The transmitter locations were confined to the extent of the receive array. Cross products obtained from the five sets of receiver measurements were averaged to provide the estimates of the correlation coefficients, which were then applied to the algorithm. The result is shown in the dashed curve which is a nearly

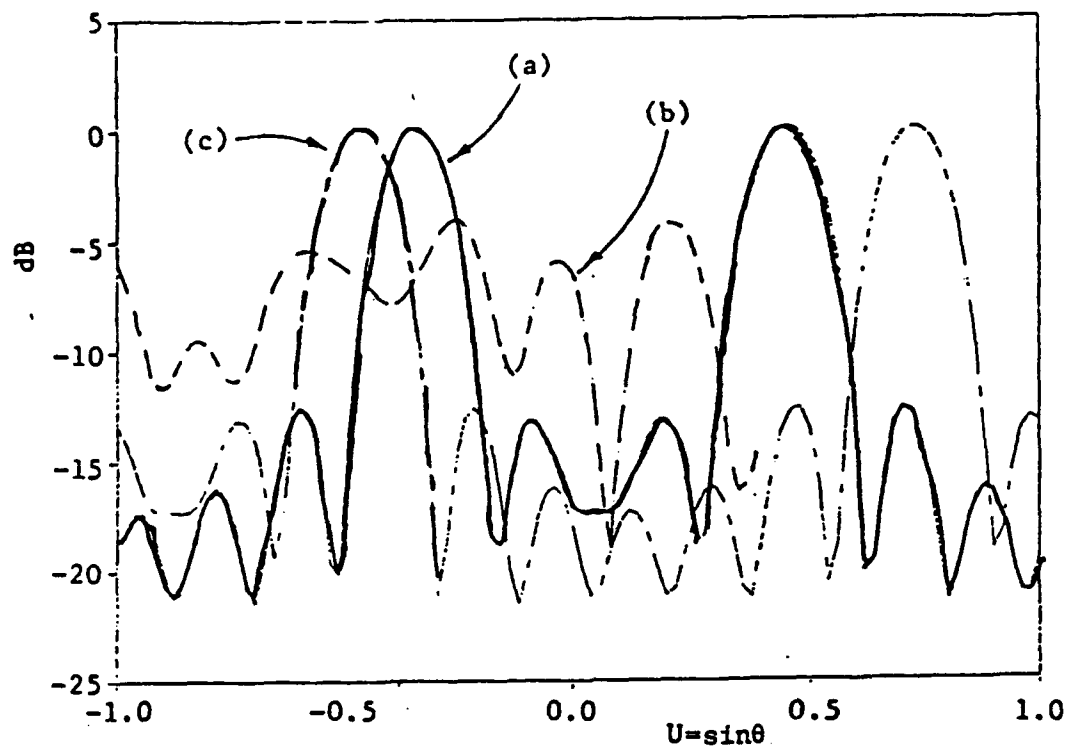


FIGURE 4.6 COMPUTER SIMULATION EXPERIMENT TO TEST MULTIPLE-LAG CORRELATION ALGORITHM.
 (a) IMAGE WITH NO PHASE ERRORS: (b) IMAGE WITH PHASE ERRORS: (c) IMAGE WITH PHASE ERRORS CORRECTED BY THE MULTIPLE-LAG CORRELATION ALGORITHM. (FROM [23].)

identical copy of the original solid curve displaced 0.68 units of u to the right.

Figure 4.7 shows another experiment. In this experiment a continuous target from $u_1 = -0.55$ to $u_2 = -0.15$ having a random rough surface was simulated by one-hundred unit amplitude and random phase scatterers randomly distributed from u_1 to u_2 . A combination of range bin diversity and transmitter diversity was employed. Two range bins were located 1300λ and 1340λ from the receiving array. The scatterer distributions in the two range bins were independent of each other. The receiving array consisted of 24 elements spaced one half wavelength apart. The FOV was illuminated from three locations, the transmitters being placed at the center and the two ends of the array. Zero mean Gaussian noise having a variance of 0.01 was introduced at each receiver. The combination of three transmitters and two range bins provided six-fold diversity for decorrelating the target scenario.

Curve (a) in Figure 4.7 is the error-free image of the first range bin. Independent phase errors, uniformly distributed between $-\pi$ and π , were then introduced at each receiver. Curve (b) is the image of the first range bin without correcting for the phase errors. This image does not resemble the target scenario whatsoever. Curve (c) is the image of the first range bin after correcting for the phase errors. This image is almost identical to the error-free image except for a shift $\Delta u = 1/3$ in the image plane.

4.5 COMPARISONS WITH OTHER ALGORITHMS

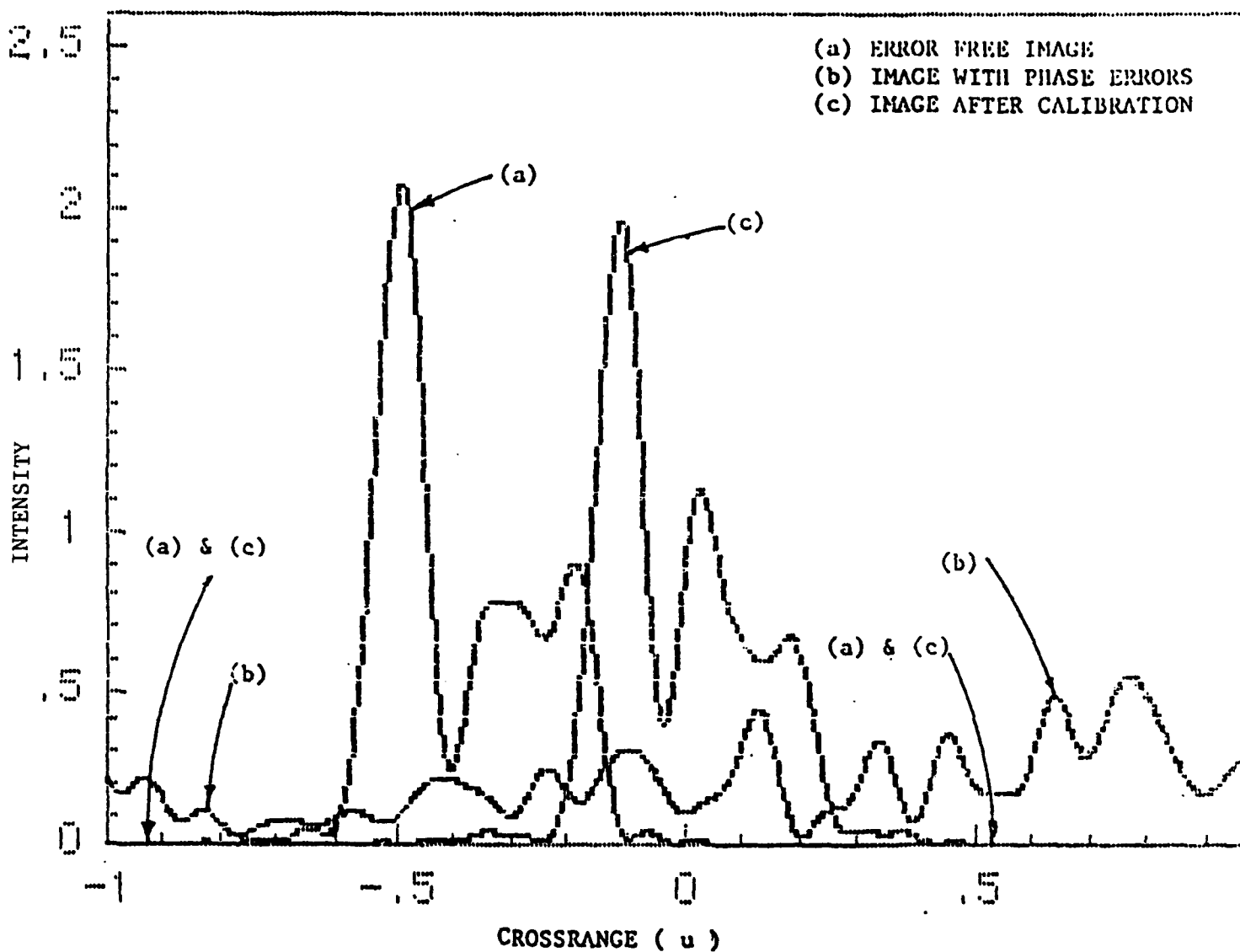


FIGURE 4.7 DEMONSTRATION OF THE MULTIPLE LAG CALIBRATOR FOR FAR-FIELD TARGETS. 100 COHERENT TARGETS, LOCATED IN THE FAR FIELD OF THE ARRAY BETWEEN $u = -0.55$ and $u = -0.15$, ARE IMAGED USING A 24-ELEMENT FILLED PERIODIC ARRAY. CURVE (a) IS THE ERROR-FREE IMAGE OF THE TARGET SCENARIO. CURVE (b) IS THE IMAGE OBTAINED AFTER ADDING RANDOM PHASE ERRORS AT EACH RECEIVER. CURVE (c) IS THE IMAGE OBTAINED AFTER CORRECTING FOR THESE PHASE ERRORS USING THE FIRST FIVE LAGS. SIXTH ORDER TRANSMITTER LOCATION DIVERSITY WAS USED FOR DECORRELATING THE COHERENT TARGETS. OBSERVE THAT THE IMAGES (a) AND (c) ARE ALMOST IDENTICAL EXCEPT FOR A SHIFT $\Delta u = 1/3$ 'u' UNITS IN THE IMAGE PLANE.

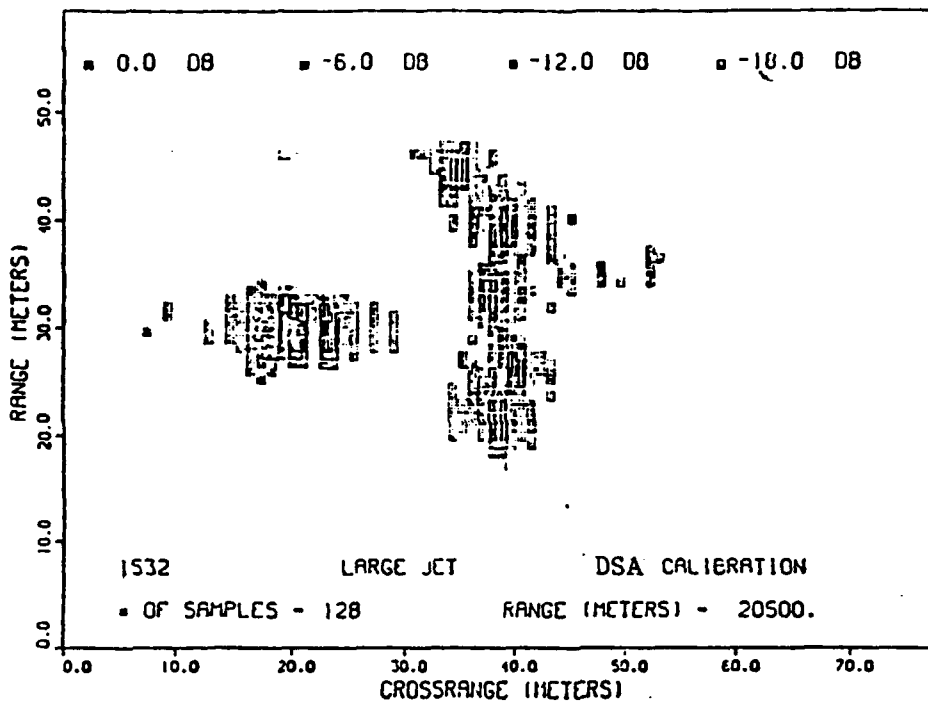
The experiments reported in this section fall into two groups. In the first three tests (Figures 4.8-4.10) the targets satisfied the dominant scatter condition; in the remainder the low variance beamformer condition was not met. The upper image of Figure 4.8 was processed using the dominant scatterer algorithm; the lower with the modified Muller-Buffington procedure. The aircraft was a large jet at a distance of about 20 km from the Valley Forge laboratory. Because the dominant scatterer condition was satisfied a satisfactory adaptively beamformed image was obtained. The bottom figure shows the image obtained using the same data set when the MMB algorithm was applied. It is evident that the two procedures were equivalent.

Figure 4.9 compares images of a Boeing 727 formed by four algorithms, the DSA, MSA, SCA and MMB. A reference scatterer with very low normalized amplitude variance ($\sigma^2 = 0.05$) was on the target. All methods work well. The main lobe gains of the adaptively formed arrays differ by no more than 0.5 dB.

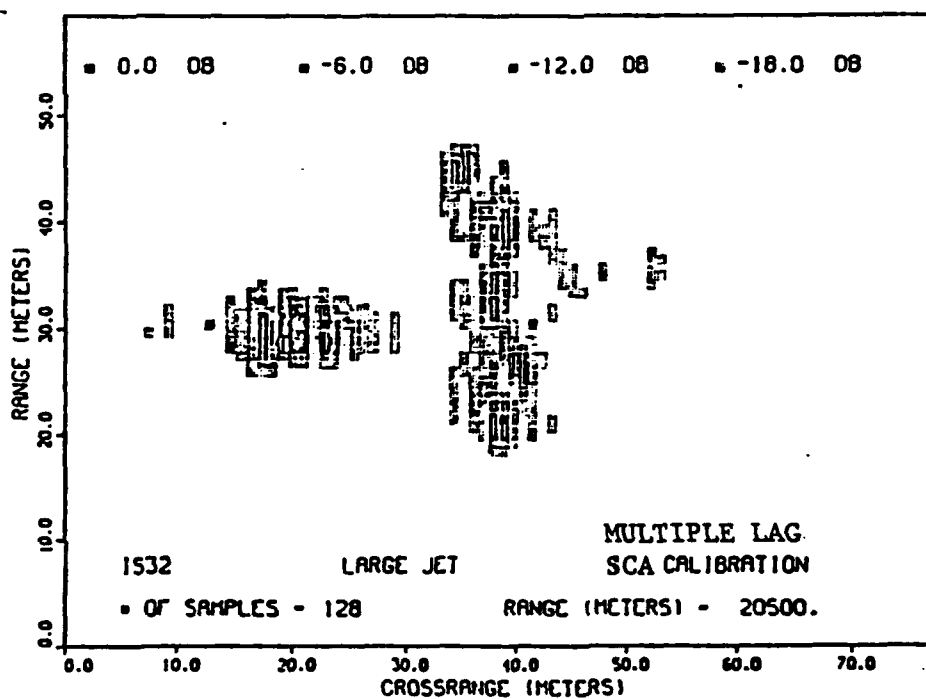
Figure 4.10 compares images of the Limerick nuclear power plant obtained from the same four algorithms. Again the results are nearly alike. The array gains differ by less than 0.5 dB.

The situation changes when no low variance range bin can be found. Figure 4.11 shows the use of bin 47 for which $\sigma^2 = 0.17$ is the reference bin. This high variance bin resulted in failure by both DSA and MSA; the former is shown in plate a. SCA and MMB were both able to form images recognizable as airplanes.

Four images from another data set obtained from the same airplane are shown in Figure 4.12. Again the SCA and MMB images are



(a)



(b)

FIGURE 4.8 RADAR CAMERA ISAR IMAGES OF A LARGE JET AIRCRAFT AT A DISTANCE OF 20 km FROM VALLEY FORGE RESEARCH CENTER. THE RANGE CELL IS 3 METERS. (a) DSA: (b) MULTIPLE LAG SCA. BOTH PROCEDURES WORKED WELL AND YIELDED COMPARABLE IMAGES. (FROM [25].)

RANGE(METERS)
2687

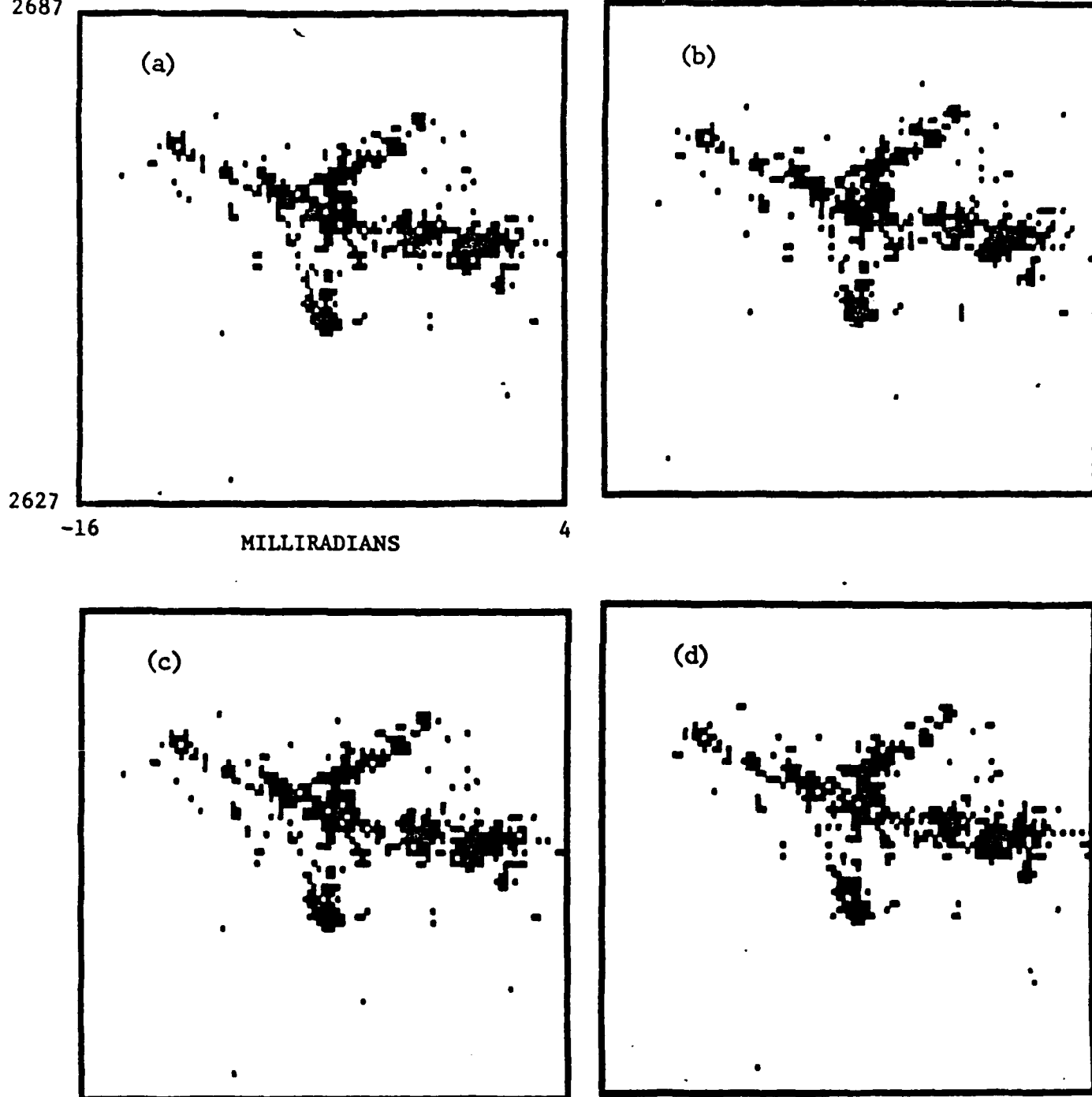


FIGURE 4.9 : RANGE-AZIMUTH IMAGE OF BOEING 727 AIRCRAFT OBTAINED USING THE FOURTH QUADRANT (ELEMENTS FROM 385 THROUGH 512). (FROM [26].)

- (a) DSA WITH BIN 40 HAVING AMPLITUDE VARIANCE 0.05 AS THE REFERENCE RANGE BIN
- (b) MSA WITH BINS 29, 40 AND 42
- (c) SCA WITH LAG ONE AND BINS 37 THROUGH 40
- (d) MMB WITH LAG (1,6,28) AND BINS 37 THROUGH 40

RANGE (METERS)

17650

17500

-10

MILLIRADIANS

30

(a) DSA WITH BIN 67

(b) MSA WITH BINS
29, 32 AND 67

(c) SCA WITH BINS
31 THROUGH 34

(d) MMB WITH BINS
31 THROUGH 34
LAG (1,8,92)

FIGURE 4.10 RANGE-AZIMUTH IMAGES OF LIMERICK NUCLEAR POWER PLANT
(FROM [26].)

RANGE (METERS)

2687

(a)

(b)

MSA NOT APPLICABLE WHEN
WHEN USING RANGE BINS 44-47.

2627

-16

MILLIRADIANS

4

(c)

(d)

FIGURE 4.11 RANGE-AZIMUTH IMAGE OF BOEING 727 AIRCRAFT. (FROM [26].)

- (a) DSA WITH BIN 47 HAVING AMPLITUDE VARIANCE 0.17
AS THE REFERENCE RANGE BIN
- (b) MSA IS NOT AVAILABLE WITH BINS 44 THROUGH 47
- (c) SCA WITH LAG ONE AND BINS 44 THROUGH 47
- (d) MMB WITH LAG (1,6,28) AND BINS 44 THROUGH 47

RANGE (METERS)

2687

(a)

(b)

2627

-16

MILLIRADIANS

4

(c)

(d)

FIGURE 4.12: RANGE-AZIMUTH IMAGE OF BOEING 727 AIRCRAFT OBTAINED USING THE SECOND QUADRANT (ELEMENTS FROM 129 THROUGH 256). (FROM [26].)

(a) DSA WITH BIN 40 HAVING AMPLITUDE VARIANCE 0.15 AS THE REFERENCE RANGE BIN

(b) MSA WITH BINS 38, 39 AND 40

(c) SCA WITH LAG ONE AND BINS 39 THROUGH 42

(d) MMB WITH LAG (1,6,28) AND BINS 39 THROUGH 42

superior. Main lobe gain is 3.3 dB greater than DSA and 3.9 dB greater than MSA.

Figure 4.13 shows DSA and SCA 1-D images of a corner reflector in which echoes from farmland were used for self-calibration. DSA fails completely; the DSA image bears no relation to that of a corner reflector while the SCA image shows a prominent target. MMB performance is comparable to SCA. Both exhibit 4.5 dB greater main lobe gain.

The observations from this and the preceding chapter lead to the following conclusions:

- If at least one range bin has a low variance beamformer ($\sigma^2 \leq 0.12$), any algorithm is satisfactory. In general the DSA is the simplest to implement.
- If no low variance bin can be found but one or more bins exhibit single targets with lower ratios of target to clutter strengths, then
 - DSA will fail.
 - MSA will often succeed, particularly with the use of overlapping subarrays.
 - SCA and MMB will always succeed.
- If no bins exhibit single targets in clutter
 - DSA and MSA will fail.
 - SCA and MMB will often succeed.

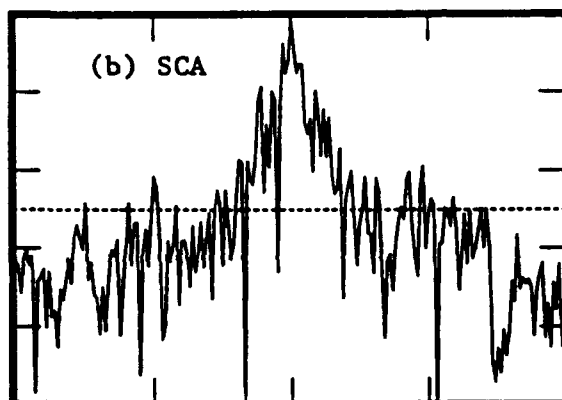
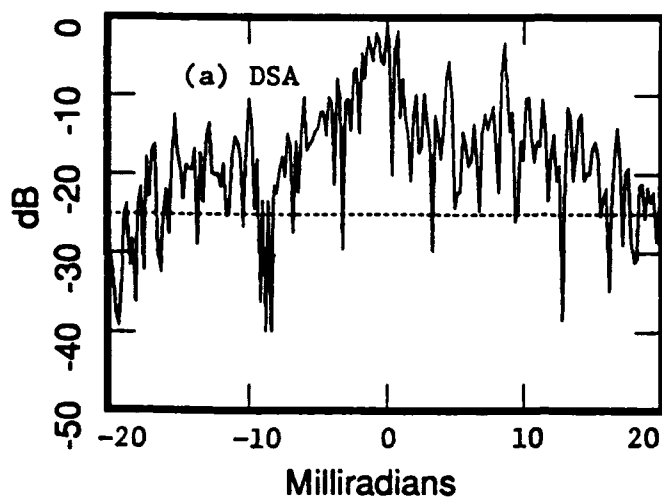


FIGURE 4.13 CROSS-RANGE IMAGES OF CORNER REFLECTOR WHEN ARRAY IS CALIBRATED ON ECHOES FROM FARMLAND. (a) DSA. (b) SCA. (FROM [24].)

5. RELATIVE COMPUTATION TIMES

Comparisons of CPU times were made for the several algorithms for two target scenes, the Limerick Nuclear Power Plant and a Boeing 727 ISAR image. The main distinction between them is that the former scene is echo-filled in range and azimuth whereas the latter target is in the clear and the scene is devoid of clutter. Taking the CPU time required for DSA to produce a 1-D image as unity, a summary of the relative times is given in Table 5.1. The reader is referred to Section 5.2 of the Appendix for further details.

	<u>1-D</u>			<u>2-D</u>		
	a	b	c	a	b	c
DSA	1	1		28	10	2.8
MSA	1.4	1.2	1.2	28	10	2.8
ITERATIVE SCA						
WITHOUT SUBARRAYS	2.9	1.5	1.9	30	11	2.7
WITH SUBARRAYS	2.8-3.2	1.5-2.2	1.7-1.4	30	11	2.7
NONITERATIVE SCA						
WITHOUT SUBARRAYS	52-250	6-23	9-11	79-277	15-32	7-9
WITH SUBARRAYS	11-43	1.9-2.5	6-17	38-70	11-12	3.5-6

TABLE 5.1 RELATIVE CPU TIME. DSA IS FASTEST FOR BOTH 1- AND 2-D IMAGES. NON-ITERATIVE SCA IS SLOWEST. ITERATIVE SCA WITH OR WITHOUT SUBARRAYS IS HIGHLY EFFICIENT.

- a. Limerick Nuclear Power Plant, 83-m array.
- b. Boeing 727, ISAR Image. Target is in the clear.
- c. Ratio of a to b.

6. SUMMARY

It is shown theoretically and experimentally corroborated that highly distorted phased arrays can be self-calibrated under a very wide range of conditions. The dominant scatterer algorithm (DSA), which is the basic procedure in the first class, can be made to self-calibrate almost always on man-made structures. A modification, the multiple scatterer algorithm (MSA), extends its usefulness under conditions of poor target to clutter ratio. The scene-free ABF algorithms are superior when the source distribution is statistically homogeneous, e.g., sea clutter. Although the scene-free techniques were designed primarily for statistically homogeneous backscattering, the experimental evidence indicates that they perform exceedingly well under those conditions in which the dominant scatterer class of algorithms work. Thus the scene-free algorithms have been found to be more generally applicable than the dominant scatterer algorithms. They do, however, require greater computational strength. However, because of the continuing improvement over the years in speed, capacity and cost of realtime signal processing devices, it is concluded that the design of future radar systems requiring very large antennas should be based upon the scene-free algorithms.

The reader is referred to pages 103, 158, 182 and 183 of the Appendix for more detailed summary observations.

References

- [1] B. D. Steinberg, "Design Approach for a High Resolution Microwave Imaging Radio Camera," Journal of the Franklin Institute, Dec. 1973.
- [2] E. N. Powers, "Adaptive Arrays for Microwave Imaging," Ph.D. Dissertation, University of Pennsylvania, 1975.
- [3] B. D. Steinberg, "Radar Imaging from a Distorted Array: The Radio Camera Algorithm and Experiment," IEEE Trans. on Antennas and Propagation, AP-29(5), 740-748, Sept. 1981.
- [4] B. D. Steinberg, Microwave Imaging with Large Antenna Arrays: Radio Camera Principles and Techniques, John Wiley and Sons, Inc., New York, 1983.
- [5] T. J. Cornwell, Lecturer on Self-Calibration, National Radio Astronomy Observation, Socorro, New Mexico.
- [6] T. J. Cornwell, "The Application of Closure Phase to Astronomical Imaging," Science, Vol. 245, No. 4915, 263-269, 21 July 1989.
- [7] J. Tsao, "Radar Imaging with Partially Coherent Array," 1988 IEEE Antennas and Propagation Society International Symposium, Vol. II, pp. 794-797.
- [8] B. D. Steinberg, "Properties of Phase Synchronizing Sources for a Radio Camera," IEEE Trans. on Antennas and Propagation, AP-30(6), 1086-1092, Nov. 1982.
- [9] B. D. Steinberg, Principles of Aperture and Array System Design, John Wiley and Sons, Inc., New York, 1976.
- [10] E. Jadlovker-Yadin, "Airborne Radars with Distributed Antenna Array," Ph.D. Dissertation, University of Pennsylvania, 1981.
- [11] J. Halat, "A Survey of Image-Embedded Passive Beamforming Sources for a Radio Camera," M.S. Thesis, University of Pennsylvania, 1986.
- [12] B. D. Steinberg, "A Theory of the Effect of Hard Limiting and Other Distortions Upon the Quality of Microwave Images," IEEE Trans. Acoust., Speech and Signal Processing, Vol. ASSP-35, No. 10, 1462-1472, Oct. 1987.
- [13] E. H. Attia, "Self-Cohering Airborne Distributed Arrays Using the Robust Minimum Variance Algorithm," AP-S International Symposium, May 1986.
- [14] E. H. Attia, "Self-Cohering Airborne Distributed Arrays," Interspec Final Report on Contract No. F19628-84-C-0080 for Rome Air Development Center (Hanscom), MA, Dec. 1985.
- [16] B. Kang, "Self-Calibration Technique of the Phased Arrays Using the Multiple Dominant Scattering Algorithm," M.S. Thesis, Moore School of Electrical Engineering, University of Pennsylvania, May 1987.
- [17] E. H. Attia and B. D. Steinberg, "Self-Cohering Large Antenna Arrays Using the Spatial Correlation Properties of Radar Clutter," IEEE Trans. on Antennas and Propagation, 30-38, Jan. 1989.

- [18] E. H. Attia, "Phase Synchronizing Large Antenna Arrays Using the Spatial Correlation Properties of Radar Clutter," Ph.D. Dissertation, Dec. 1984.
- [19] H. M. Subbaram and B. D. Steinberg, "Decorrelation of Coherent Targets Using Transmitter Location Diversity," Feb. 1987. Accepted by IEEE Trans. on Antennas and Propagation, subject to revision.
- [20] H. M. Subbaram and B. D. Steinberg, "Scene Independent Self-Calibration of Phased Array Antennas," submitted to IEEE Trans. on Antennas and Propagation.
- [21] G. T. Herman, Image Reconstruction from Projections: The Fundamentals of Computerized Tomography, Academic Press, New York, 1980.
- [22] B. D. Steinberg, "Microwave Imaging of Aircraft," Proceedings of the IEEE, Vol. 76, No. 12, 1578-1592, Dec. 1988
- [23] B. D. Steinberg, "Distortion Correction by Image Feedback Control," Valley Forge Research Center Quarterly Progress Report No. 49, March 1986, pp. 54-58.
- [24] B. Kang, "Research on Self-Calibrating Algorithms for Microwave Imaging Systems," UP-VFRC-2-89, Jan. 1989.
- [25] Valley Forge Research Center Quarterly Progress Report No. 52. Jan.-June 1987.
- [26] Valley Forge Research Center Quarterly Progress Report No. 55, Apr.-June 1988.
- *[27] B. Kang, "Research on Self-Calibrating Algorithms for High-Resolution Microwave Imaging Systems", RL-TR-91-57, Vol II (of two), Apr 91.

Although this report references * limited document above, no limited information has been extracted. The report is limited to USGO agencies and their contractors; software documentation; Apr 91. Other requests RL (EEAS) Hanscom AFB MA 01731-5000.

**MISSION
OF
ROME LABORATORY**

Rome Laboratory plans and executes an interdisciplinary program in research, development, test, and technology transition in support of Air Force Command, Control, Communications and Intelligence (C³I) activities for all Air Force platforms. It also executes selected acquisition programs in several areas of expertise. Technical and engineering support within areas of competence is provided to ESD Program Offices (POs) and other ESD elements to perform effective acquisition of C³I systems. In addition, Rome Laboratory's technology supports other AFSC Product Divisions, the Air Force user community, and other DOD and non-DOD agencies. Rome Laboratory maintains technical competence and research programs in areas including, but not limited to, communications, command and control, battle management, intelligence information processing, computational sciences and software producibility, wide area surveillance/sensors, signal processing, solid state sciences, photonics, electromagnetic technology, superconductivity, and electronic reliability/maintainability and testability.